

**Groundwater Flow at the
Prototype Repository
- Task 8e of SKB**



Gesellschaft für Anlagen-
und Reaktorsicherheit
(GRS) gGmbH

Groundwater Flow at the Prototype Repository - Task 8e of SKB

Klaus-Peter Kröhn

November 2018

Remark:

This report has been funded by the Federal Ministry for Economic Affairs and Energy (BMWi) under the contract no 02E11213.

The work was conducted by the Gesellschaft für Anlagen- und Reaktorsicherheit (GRS) gGmbH.

The author is responsible for the content of the report.

GRS - 431
ISBN 978-3-946607-13-7

Keywords:

Crystalline Rock, Final Repository, Fracture Flow, High-level Waste, Long-term Safety, Thermo-haline Flow

Acknowledgements

This report summarises work for the BMWi between 2013 and 2016 under contract no. 02E11213 (QUADER). Funding of this work is gratefully acknowledged.

Working on Task 8 would not have been possible without numerous discussions within the Task Forces on Groundwater Flow and Solute of Transport. All questions and requests for data have been answered with a delightful professional swiftness that helped many times. Thank you to everybody in this group.

Many thanks are also due to the developers of d^{3f} at the University of Frankfurt, especially Dr. Dmitrij Logashenko and Sebastian Reiter without whose help the groundwater flow models would neither have been set up nor would have worked. Also many thanks go to Anke Schneider, Anne Gehrke, and Dr. Hong Zhao from GRS who gave a lot of practical help and advice concerning the handling of the code d^{3f}.

Thank you to you all.

Abstract

The Task Force on Groundwater Flow and Transport of Solutes (TF GWFTS) and the Task Force on Engineered Barrier Systems (TF EBS), both established by the Svensk Kärnbränslehantering AB (SKB), have defined the so-called Task 8 to investigate the hydraulic interaction of the granitic host rock at the Hard Rock Laboratory at Äspö and the bentonite clay buffer in a deep geological repository. Subtasks 8 a-d ran parallel to the related BRIE-project (Bentonite Rock Interaction Experiment) at the Äspö Hard Rock Laboratory (HRL). These subtasks lead to a variety of predictive models with respect to flow in a buffer-rock system on the comparatively small scale of the BRIE. Task 8e related to the Prototype Repository (PR) was therefore subsequently defined in order to check these concepts on a much larger scale and under the additional influence of temperature.

Task 8 encompassed obviously characterizing the groundwater flow field as well as simulating bentonite re-saturation. In the framework of Tasks 8 b-d an approach had been developed where the problem of groundwater flow in rock and buffer is solved by decoupling both aspects. Groundwater flow was simplified to a steady-state single-phase flow model including discretely described large fractures. Modelling was performed with the code d³f. This report is concerned with Task 8e addressing the aspect of groundwater flow at the PR with respect to two questions: is the conceptual approach for groundwater flow that was developed for the BRIE viable at different conditions and what is the influence of temperature on the flow field?

The procedure of the PR-experiment can roughly be divided into a pre-installation phase where only the tunnel and the boreholes existed and an operational phase after installing buffer and heaters when the heaters were switched on. During the pre-installation phase groundwater flow was isothermal without interference of the buffer and a lot of effort went into characterizing the hydrogeological conditions around the PR. This phase represents therefore the most simple and, at the same time, the best known flow conditions.

The pre-installation phase was therefore considered to be most appropriate to develop a well-founded flow model. Based on the model concept for the BRIE and beginning with the related material data, a first model was set up which was then calibrated against out-flow data for the tunnel as well as for the boreholes. It became apparent that only mod-

erate modifications were necessary to achieve a satisfactory match thereby confirming the model concept for groundwater flow at Äspö.

To answer the second question called for modelling flow during the operational phase which included the thermal effects from heating the canisters. To investigate the impact of heating a pure heat conduction model was set up for calculation with the code COMSOL. Significant heating appeared to occur only in the vicinity of the canisters, though.

Neglecting a possible influence of convective heat transport on the temperature field, the temperature evolution at each of the borehole surfaces in the model was determined as input into a thermo-hydraulic model for the operational phase. Using the option in d3f to couple heat transport with groundwater flow allowed then to have a direct comparison of the isothermal and the non-isothermal flow field.

The general patterns of the isothermal flow field remained basically preserved in the thermo-hydraulically coupled (TH-)model. The flow velocities were not increased by considerably more than a factor of 2. This factor is consistent with the temperature-induced changes of density and viscosity of the water. It has thus to be concluded that heat production from the waste canisters does not result in a noteworthy change of groundwater flow as long as there is significant outflow from the rock into the deposition boreholes. The pressure gradient from the boundary towards the geotechnical openings is simply too high to allow for density-dependent flow effects. How this would change in accordance with the expected low flow rates that are imposed by the water uptake of the bentonite buffer remains to be investigated.

Table of contents

1	Introduction	1
1.1	Background.....	1
1.2	Objectives of Task 8e.....	2
1.3	Scope of modelling.....	2
2	Modelling approach for Task 8e.....	5
2.1	Modelling objectives.....	5
2.2	Approach.....	6
2.2.1	Overall concept	6
2.2.2	Flow model.....	6
3	Data base for the flow model.....	9
3.1	Coordinates.....	9
3.2	Tunnel system.....	9
3.3	Geometry	11
3.3.1	Prototype Repository layout	11
3.3.2	Deposition boreholes	11
3.3.3	Secondary test boreholes.....	13
3.3.4	Fractures.....	14
3.4	Outflow.....	15
3.4.1	Prototype Repository tunnel	15
3.4.2	Deposition boreholes	17
3.4.3	Other drifts	23
3.5	Hydraulic properties	24
3.5.1	Matrix and background fractures.....	24
3.5.2	Fractures.....	25
3.6	Influence of salinity.....	26

4	Isothermal flow model	27
4.1	Model domain	27
4.2	Hydraulic properties	30
4.3	Boundary conditions.....	31
4.4	Calibration targets.....	35
5	Heat transport model	37
5.1	Model domain	37
5.2	Thermal properties.....	37
5.2.1	Rock.....	37
5.2.2	Other materials	39
5.3	Thermal initial and boundary conditions	40
5.4	Calibration targets.....	41
6	Thermo-hydraulic flow model	43
6.1	Model domain	43
6.2	Material properties	43
6.3	Initial and boundary conditions	43
6.3.1	Groundwater flow	43
6.3.2	Heat flow	44
6.3.3	Sets of boundary conditions	46
6.4	Calibration targets.....	47
7	Results.....	49
7.1	Pre-installation flow	49
7.1.1	Calibration.....	49
7.1.2	Outflow rates.....	51
7.1.3	Pressure	55
7.1.4	Flow	55
7.2	Heat transport	62
7.2.1	Calibration.....	62

7.2.2	Heating dynamics.....	62
7.3	Thermo-hydraulic flow	71
7.3.1	State variables	71
7.3.2	Flow field.....	71
7.3.3	Outflow.....	77
8	Discussion.....	87
9	Conclusions	91
	References	93
	Table of figures.....	97
	List of tables.....	101
	Appendix A Humidity measurements.....	103
A.1	PR-tunnel.....	103
A.2	Deposition boreholes	106
	Appendix B Deriving fracture locations from flow data and trace lines	111
B.1	Deducing positions of highly water-producing features from outflow.....	111
B.2	Fracture trace lines	113
B.3	Relation of the fracture trace lines and the outflow from the rock	114
B.4	Value of the trace lines.....	117
B.5	Conclusions on fracture orientation	118
B.6	Assumed hydraulic features for the model.....	119
B.7	Deterministic hydraulic features	121
	Appendix C Comparison of flow rates	127

1 Introduction

1.1 Background

The Swedish Svensk Kärnbränslehantering AB (SKB) has established the Task Force on Groundwater Flow and Transport of Solutes (TF GWFTS) in 1992 and the Task Force on Engineered Barrier Systems (TF EBS) in 2004. Each of these Task Forces builds a frame for an international group of participants to work on specific problems concerning flow and transport in crystalline rock and the behaviour of the bentonite buffer in a deep geological repository, respectively. In collaboration representatives of both Task Forces have come up with the definition of the so-called Task 8, a compilation of several sub-tasks – called 8a, 8b, etc. – with a view to the hydraulic interaction of the granitic host rock and the bentonite clay buffer /VID 17/. Task 8e is concerned with the full-scale Prototype Repository (PR) at the Hard Rock Laboratory (HRL) at Äspö.

Three years before Task 8e was defined the TF EBS had already taken the PR as a benchmark in the framework of THM-modelling. One strong motivation had been the fact that the outer section of the PR was about to be terminated thus offering the opportunity to make blind predictions about the outcome as well as checking the results later against post-test investigations. Prediction did not come up in time, though. One reason might be that a considerable effort was required to set up a plausible flow model before modelling the whole test. Eventually, the members of the TF EBS could nevertheless investigate the re-saturation process in detail. Since much less time was allocated for Task 8e the TF GWFTS focussed more on the flow aspect of the problem.

While the option of granite as a host rock for a nuclear waste repository did not have top priority in Germany in the past, there has nevertheless been considerable effort in the past to investigate hydraulic problems in crystalline rock. Quite recently, the development of the codes d^3f and r^3t originally designed to apply cutting edge numerical methods to modelling density-dependent groundwater flow and transport in the cap rock of salt domes was extended to incorporate fracture flow /SCH 12/.

Participation in research work that included fracture flow as well as bentonite re-saturation appeared to be a consequent step forward that would increase experience in both fields and contribute to the problem at hand. However, modelling groundwater flow had taken much more time than intended so that modelling bentonite re-saturation was seriously delayed. This report therefore concentrates on groundwater flow in the framework of Task 8e.

1.2 Objectives of Task 8e

The following text is directly cited from /VID 17/:

“One aim of Task 8 is to improve the knowledge of the bedrock-bentonite interface with regard to groundwater flow. The main objectives with this exercise are to:

- Test the gained understanding of fractured bedrock control on bentonite wetting. Primarily intended to test the approaches, conceptual models, and numeric developed within Task 8a-8d.
- Scale up to a full-scale deposition hole scale as well as the deposition tunnel scale. Primarily intended to test the approaches, conceptual models, and numeric developed within Task 8a-8d.
- Test the thermal influences created by the waste (in the Prototype Repository project mimicked by heaters).
- Test interactions between deposition holes.
- Test effects on the wetting due to backfilling.
- Test effects on the wetting due to drainage effects.
- Serve as a blind prediction of the future state of the wetting in deposition holes 1 – 4.

The work described in this report address at least partly the first three bullet points.

1.3 Scope of modelling

Work on Task 8 b-d being focused on the BRIE had shown that the coupling of groundwater flow and bentonite re-saturation appears to be weak in the framework of the approach of GRS /KRÖ 17b/. Groundwater flow and bentonite re-saturation had thus been treated separately. The first appealing aspect of Task 8e was therefore tackling a real

thermo-hydraulic problem in fractured rock to test the advanced groundwater flow code. A successful model was to confirm the code as well as to contribute to the understanding of the flow regime at the PR. The focus of the work presented here thus lay on interpretive modelling rather than on predictions.

Isothermal groundwater flow and of thermo-hydraulically coupled flow was calculated with the code d^{3f} /SCN 12/. Modelling heat flow to provide input for the boundary conditions in the thermo-hydraulic model was performed with COMSOL /COM 13/.

2 Modelling approach for Task 8e

2.1 Modelling objectives

From the objectives of Task 8e two key questions were identified:

- Is the conceptual approach for groundwater flow that was developed for the BRIE viable at other conditions?
- What is the influence of temperature on the flow field?

The first question could best be answered by modelling flow during the pre-installation phase of the Prototype Repository (PR). As long as the deposition holes had not been filled, the flow conditions were quite similar to the conditions at the BRIE, namely isothermal flow, a hydraulic gradient from deep in the rock towards tunnel and boreholes, some deterministic fractures, background fractures and outflow over tunnel and borehole walls. Differences between BRIE and PR concern the geometry of the geotechnical openings and the size of the in-situ tests thus allowing to check the approach developed for the BRIE.

For answering the second question the isothermal model was used again. The effect of the heaters was simulated by applying transient temperatures to the surface of the deposition boreholes. This procedure allowed on the one hand to leave out heater and buffer but required on the other hand a heat flow simulation to acquire the necessary temperature data. Assessment of the impact of heating was then based on the outflow rates from the rock into the deposition boreholes as calculated by the isothermal and the non-isothermal model. According to the discussion about the interplay of the water producing rock and the water uptake characteristics of a bentonite buffer in /KRÖ 17b/ this comparison can only account for very early times of the buffer-rock system. With a view to the general flow characteristics, it proved to be nevertheless illuminating to continue modelling for a significant period of time even if the model did subsequently not represent realistic conditions. Appropriate model set-ups for these cases would have been possible and related modelling desirable but could not be realised within the given time frame.

2.2 Approach

2.2.1 Overall concept

Task 8 had apparently two aspects: water flow in the host rock and water uptake of the bentonite. Both phenomena are often described on the basis of two-phase flow. This allows formally a simultaneous calculation of flow in the rock and in the bentonite with the same numerical tools which is usually based on coupled thermo-hydro-mechanically (THM) balance equations. However, the two-phase flow concept appears to be not entirely consistent with the observed phenomena in the bentonite (e. g. /KRÖ 11/). It was therefore a natural choice to use separate tools for fracture flow and for bentonite re-saturation, in this case the groundwater flow code d^{3f} /SCN 12/ and the re-saturation code VIPER¹ /KRÖ 11/.

By and large the same approach for the flow model in Task 8e was applied as in Task 8d. A groundwater flow model was set up to explain the observed outflow into tunnels and boreholes. The calculated and/or measured outflow rates were then intended to be used as input for the axisymmetric re-saturation model of a horizontal disk of buffer material in the deposition boreholes. Model concept as well as model parameters were adopted from Task 8d where appropriate. Modelling re-saturation had to be dropped, though, in favour of finding a viable representation of the groundwater water flow.

2.2.2 Flow model

All groundwater flow models used for Task 8 contain three features: matrix, large deterministic fractures or fracture/deformation zones and background fractures. A hybrid approach that allows to describe discrete fractures embedded in a continuum was chosen for this problem.

At Äspö there is in principle the so-called “**undisturbed matrix**” or “intact rock”. It is a common assumption though that fractures exist on all length-scales. In /DER 03/ for in-

¹ VIPER is an experimental code that had been developed to test the alternative conceptual model and is thus presently still restricted to one-dimensional or 2d axisymmetric models.

stance it is claimed that “The connected porosity in crystalline rock is mainly made up of micro fractures ...”. This means there are always fractures that are smaller than any reasonably sized volume thus challenging the concept of a REV.

Background fractures are defined here as fractures that are of significantly smaller scale than the model domain and are only described in terms of stochastic mathematical laws. Despite the discussion about the applicability of the REV concept the background fractures had not been explicitly considered in the flow model for Task 8d. Instead, they were allowed for as an increase of the homogeneous matrix permeability. As it turned out during calibration this increase was substantial /KRÖ 17b/.

Large deterministic hydraulic features have a size comparable to the model domain or larger. Evidence of such features as detected by /RHÉ 01/ was initially not known to the TF EBS or even later also to the TF GWFTS. Following the discussion in section 3.3.4, however, the outflow measurements in the PR-tunnel indicate at least two highly active hydraulic features towards the end of the tunnel and one in the vicinity of the outer plug. Reasoning concerning such features led to a set of assumed fractures and fracture zones as described in Appendix B.

Later, when the deterministic fractures were widely acknowledged among the participants of Task 8e, it turned out that there was a good fit between the previously assumed fractures in the GRS model and the documented features in terms of location and orientation. Only the size was different as all previously assumed fractures at the PR-site including those of other participants had been larger than the model domain – like at the BRIE-site – while the detected fractures fit clearly into any reasonably sized model domain for the PR.

The aperture of the fractures is taken to be extremely small in comparison to the model size while they are nevertheless producing large amounts of water. A discrete representation of the fractures was feasible since the flow code d^{3f} meets the challenge of reproducing high flow rates within fractures in direct vicinity of slow flow in a low conducting matrix /SCN 12/. For the lack of better knowledge the large deterministic fractures are simplified to features with constant properties within their plane.

Additionally included in the model is a so-called “skin” at the drifts and borehole walls. The expression “**skin**” denotes here a narrow zone of significantly reduced permeability. The idea of such a skin appears to be rather widely spread among the fractured rock modeling community. Two documented examples are discussed in more detail in /KRÖ 17b/.

While the physical reason for the observed considerable flow reductions has not been determined yet there are several mechanisms being possibly responsible, among them degassing of dissolved gases where the water pressure drops below the solubility limit for gas and mechanical effects from changes of the stress field in the rock. Impediment of water flow by forming of gas bubbles can take place only in rather small flow channels where a high capillary pressure prevails. This would affect the matrix with its very small pores rather than the fractures where bubbles are more likely to be flushed out right after forming. Increased stresses on the other hand should affect the transmissivity of fractures as well as the permeability of the matrix.

Note that decreasing the rock permeability in the skin for single-phase flow is equivalent to unsaturated flow or two-phase flow in a water-gas system where the relative permeability acts as a reduction factor for the intrinsic permeability.

Ideas about the extension of such a skin and the related permeability reduction were taken over from the model for Task 8d and formed a basis for the implementation of skins in the flow model for Task 8e. The model thus contains a low permeability skin around tunnels and boreholes and allows also for a reduction of permeability of fractures where the deterministic features are located within this skin.

3 Data base for the flow model

3.1 Coordinates

The coordinate system used for location data in Task 8 is the Swedish RT90 system. At Äspö this system leads to excessively large numbers. It was therefore recommended to cut off the leading 4 digits of the x- and y-coordinates.

As a consequence the geometric data showed inaccuracies on a scale of a metre. Where necessary, adjustments based on common sense were introduced.

3.2 Tunnel system

An artistic view of the tunnel system at Äspö is given in Fig. 3.1. The tunnel with the Prototype Repository (PR) experiment can be found at the right hand side.

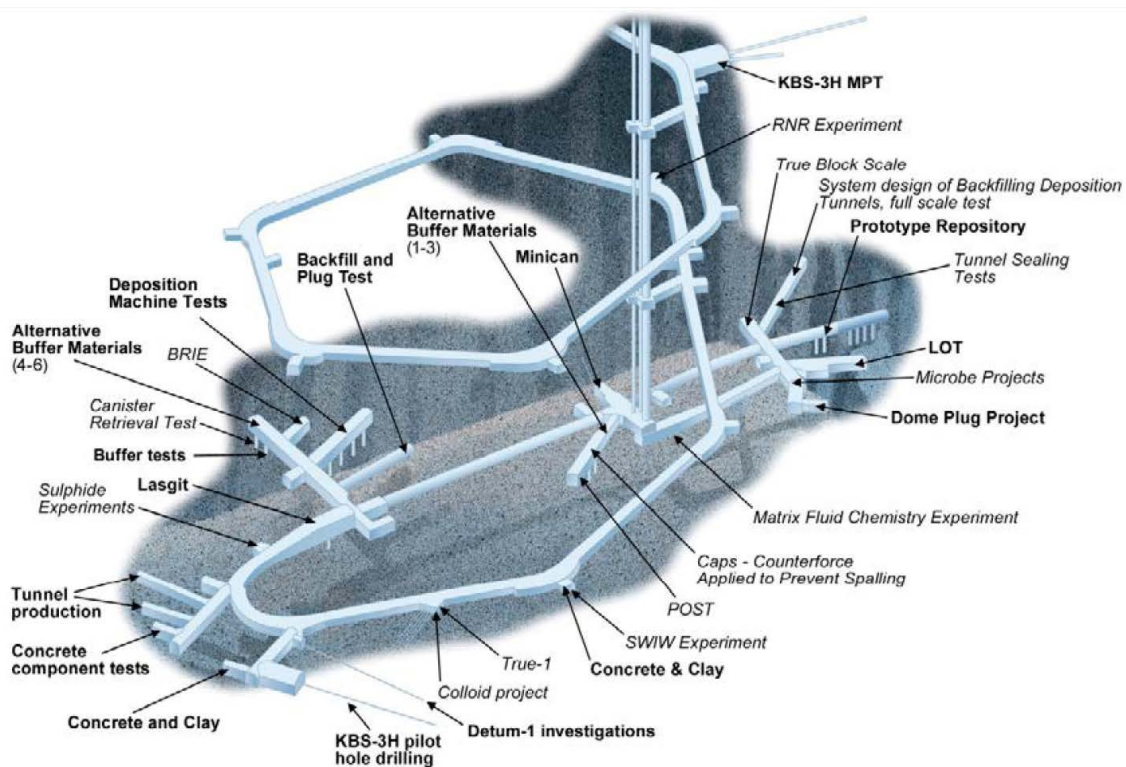


Fig. 3.1 Experiments at the Äspö URL; from /VID 17/

A more recent 3d-sketch showing a close-up is depicted in Fig. 3.2. Note that the TASS-tunnel was not excavated until 2007 and does therefore not show on older graphics.

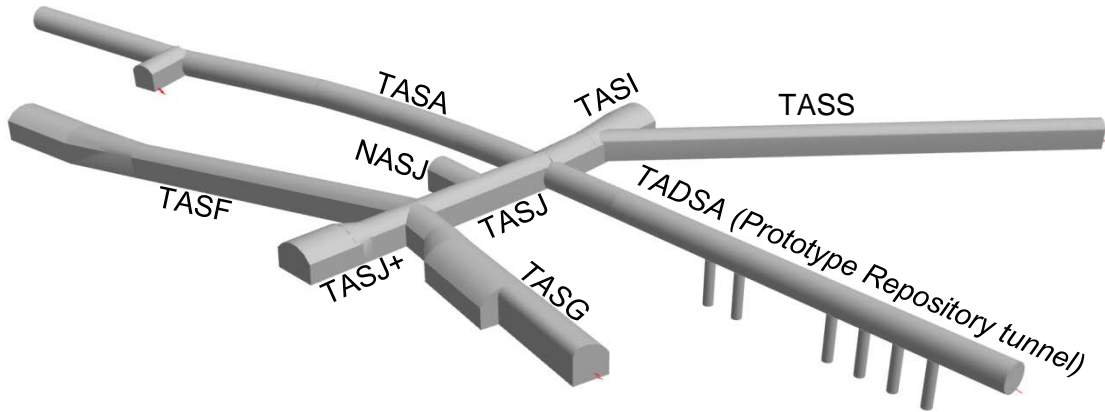


Fig. 3.2 Sketch of the tunnel system around the Prototype Repository

The detailed floor plan of the surroundings of the PR depicted in Fig. 3.3 provides the means of telling the size of the PR-tunnel².

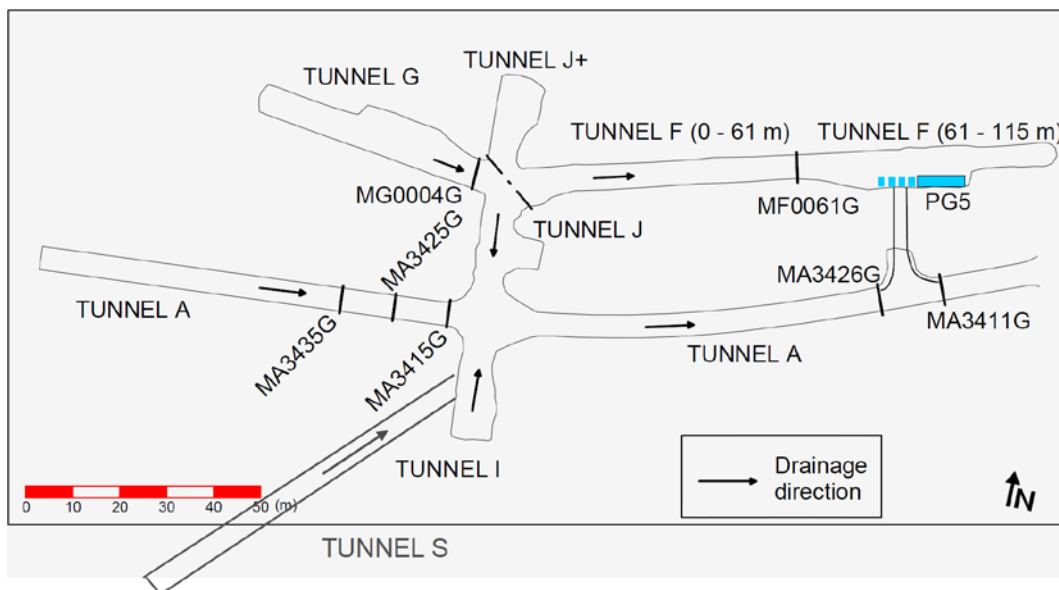


Fig. 3.3 Floor plan of the area around the Prototype Repository; modified from /ALM 05/

² While the systematic labelling of the tunnels has persisted over time, the tunnel housing the PR experiment was denoted by several names in the literature, like A-tunnel, TBM-tunnel, PR-tunnel etc.

3.3 Geometry

3.3.1 Prototype Repository layout³

The Prototype Repository drift, 65 m long and 5 m in diameter, was excavated using a Tunnel Boring Machine (TBM). Further details are compiled in Tab. 3.1. Two new tunnels were utilized for the project, TADSA (Prototype Repository Tunnel) and TASG (Data acquisition tunnel). The tunnels run sub-parallel to each other. Holes were drilled to lead cables for power and instruments between the tunnels, see Fig. 3.4.

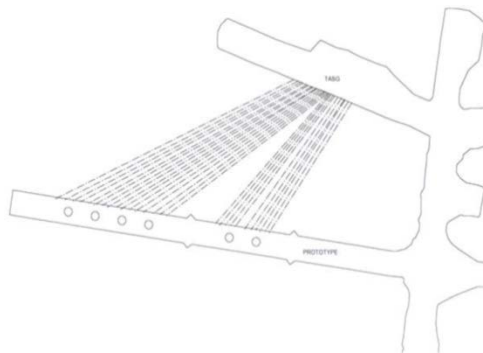


Fig. 3.4 Ground plan showing the PR-tunnel and the G-tunnel; from /VID 17/

Tab. 3.1 Approximate geometric data of the Prototype Repository

Total tunnel length	63 m
Length of section I	40 m
Length of section II	23 m
Tunnel diameter	5 m

3.3.2 Deposition boreholes⁴

Six vertical deposition holes, 8.37 m deep and 1.75 m in diameter, were drilled into the tunnel floor. The Prototype Repository consists of two sections. The installation of the first Section of Prototype Repository was made during summer and autumn 2001 and Section 2 was installed in spring and summer 2003.

³ This section is copied from /KRI 10/

⁴ This section is copied from /KRI 10/.

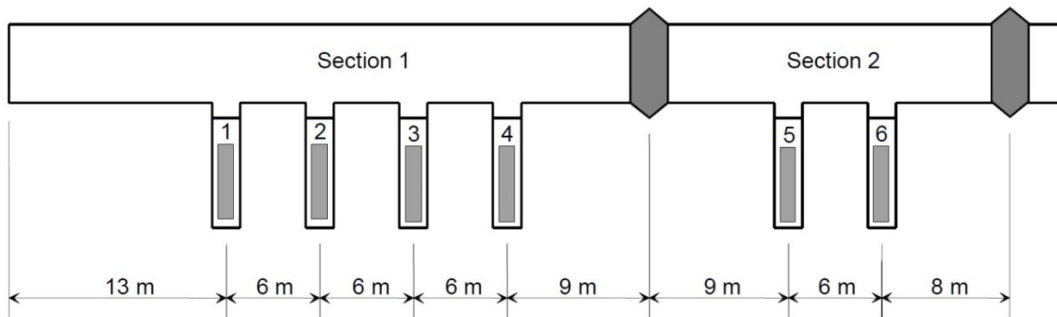


Fig. 3.5 Schematic view of the Prototype Repository; from /VID 17/

Section 1 consists of four full-scale deposition holes, copper canisters equipped with electrical heaters, bentonite blocks and a deposition tunnel backfilled with a mixture of bentonite and crushed rock and ends with a concrete plug as shown in Fig. 3.5. The inner part of Section 1 was wet, and in order to handle the water inflow a draining system (a sump inside hole 1⁵ where water was drained from) was installed. Section 2 consists of two full-scale deposition holes with a backfilled tunnel section and ends also with a concrete plug. To simulate the thermal behaviour of the nuclear waste, heaters are installed in the canisters.

The bentonite buffer in deposition holes 1, 3, 5 and 6, the backfill and the surrounding rock are instrumented with gauges for measuring temperature, water pressure, total pressure, relative humidity, resistivity and canister displacement. The instruments are connected to data collection systems by cables protected by tubes, which are led through the rock in watertight lead throughs. Instrumentation is used to monitor processes and properties in the canister, buffer material, backfill, and the near-field rock.

Tab. 3.2 Approximate geometric data of the deposition holes

Deposition hole depth	8 m
Deposition hole diameter	1,75 m
Canister height	~5 m
Canister diameter	1,05 m
Bentonite thickness below the canister	0,5 m
Bentonite thickness above the canister	1,5 m

⁵ There is an official long denomination for each borehole that includes the position of the borehole as a coordinate on the tunnel axis. For convenience each hole has also simply a number between 1 and 6. Borehole 1 is thus officially called DA3587G01 and hole 6 is DA3545G01.

3.3.3 Secondary test boreholes

Location and size of the secondary test boreholes are depicted in /ALM 05/ as well as /RHÉ 01/ (see Fig. 3.6). According to /FOR 01/ they were already sealed before drilling the deposition boreholes in order to observe changes in the pressure field. During the active time of the PR monitoring was continued /ALM 05/ so that these boreholes did not significantly interfere with the flow field at the PR⁶. They are thus not considered in the flow model.

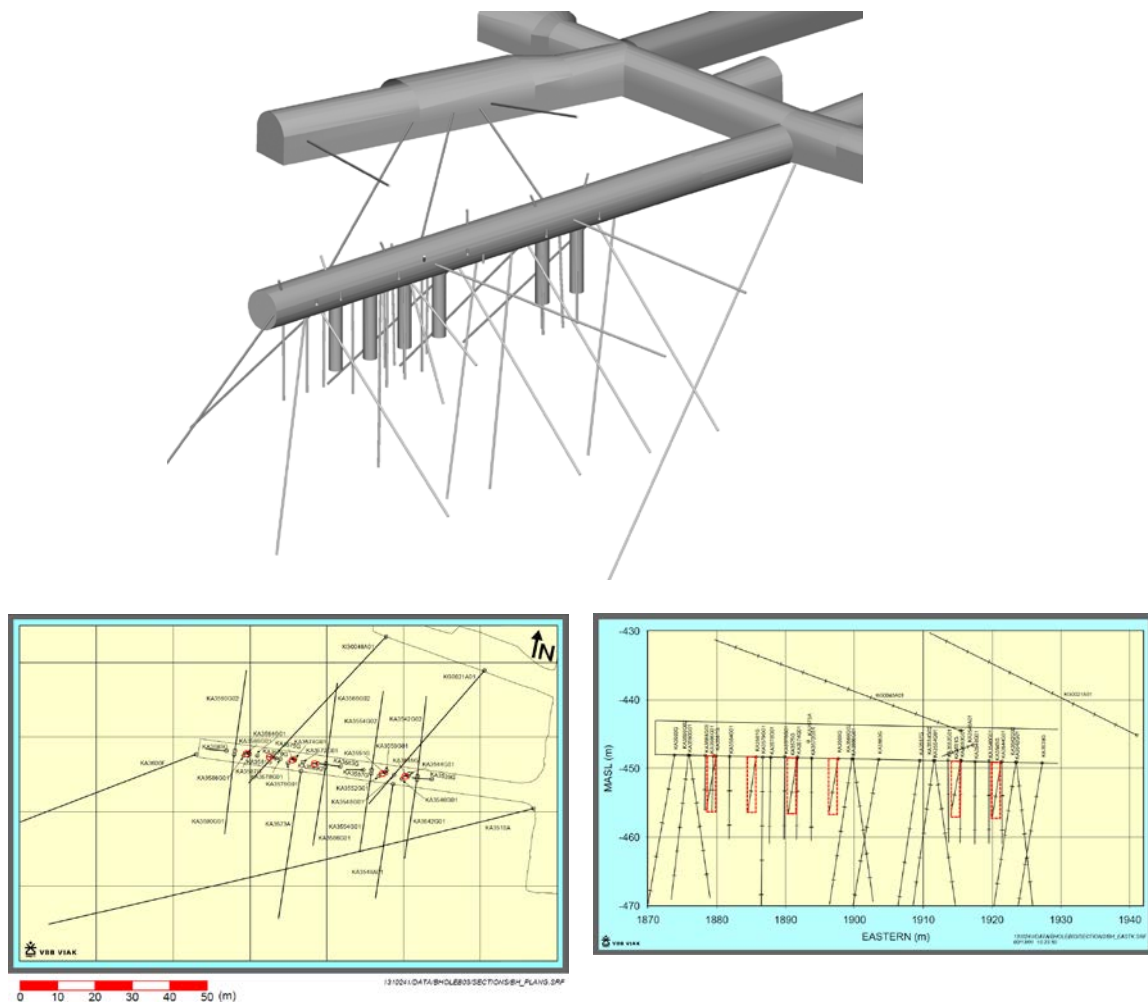


Fig. 3.6 Location and size of the secondary test boreholes; 3D-view from /ALM 05/, cross-sections from /RHÉ 01/

⁶ The only exception was when a packer failed in April 2006. On this occasion a significant increase of out-flow from the rock could be observed /KRI 10/.

3.3.4 Fractures

No direct information about hydraulic large-scale features was given in the task description /KRI 10/. It included only fracture traces in the drifts. Outflow data for tunnels and boreholes gave some additional indications. Based on these data a system of 6 fractures or fracture zones was derived. Details can be found in Appendix B.

Only then the author became aware of the extensive hydraulic test program /RHÉ 01/ that had been performed using the large array of secondary boreholes described in section 3.3.3. From this program 2 major and 6 minor deterministic fractures had already been identified as depicted in Fig. 3.7.

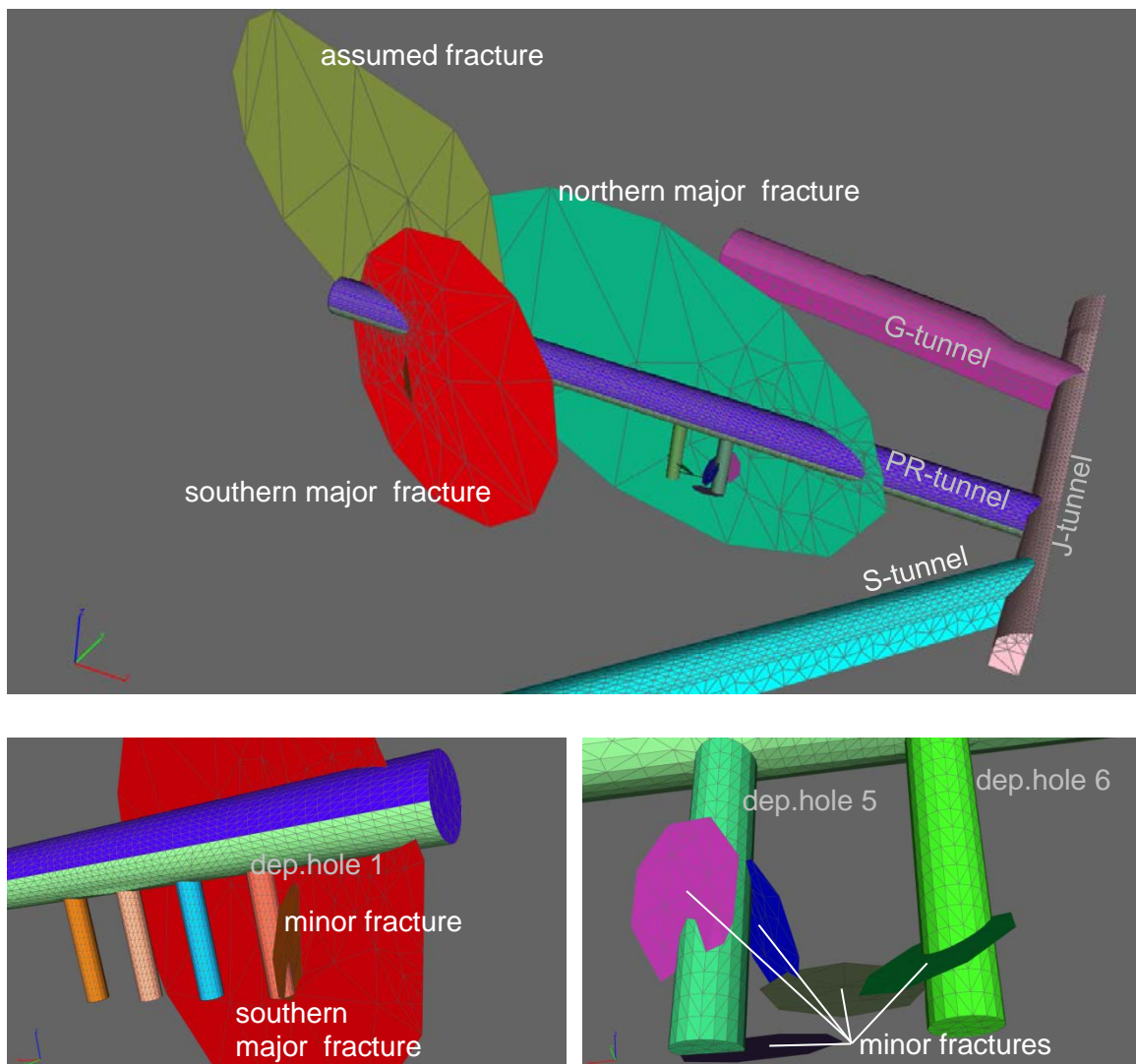


Fig. 3.7 Deterministic fractures according to /RHÉ 01/ and assumed fracture

A comparison of the theoretically postulated fractures with the fractures derived from the hydraulic testing showed that 5 of the 6 theoretical fractures could directly be replaced by the deterministic fractures. The reasoning is given in Appendix B as well.

The sixth previously postulated feature at the end of the PR-tunnel was then modified to fit in with the other two major deterministic fractures in terms of size and orientation. A possible location for this assumed fracture had now to comply with the condition that the fracture must have gone undetected by the extensive hydro-testing of the vicinity of the PR-tunnel (see Fig. 3.6). The sum of these conditions defined the fracture quite clearly.

3.4 Outflow

3.4.1 Prototype Repository tunnel

Sectionnally mean outflow rates have been measured along the PR-tunnel in three campaigns (1997, 1999 and 2000) by means of weirs /RHÉ 01/. The results are compiled in Tab. 3.3 and plotted in Fig. 3.8. Note that range and position of the weirs in the 1997 campaign was different from the other two.

Tab. 3.3 Outflow into the PR-tunnel measured by means of weirs; after /RHÉ 01/

Campaign 1997			Campaigns 1999 & 2000				Mass outflow		
Weir from [m]	sections to [m]	Q (1997) [L/min]	Weir from [m]	sections to [m]	Q (1999) [L/min]	Q (2000) [L/min]	1997	1999	2000
							[kg/s]		
3527	3533	0.20					3.33E-03		
3533	3539	1.17					1,95E-02		
3539	3545	0.12					2.00E-03		
3545	3551	0.03	3546	3552	0.001	0.006	5.00E-04	1.67E-05	1.00E-04
3551	3557	0.02	3552	3570	0.100	0.110	3.33E-04	1.67E-03	1,83E-03
3557	3562	0.05					8,33E-04		
3562	3568	0.10					1.67E-03		
3568	3575	0.05	3570	3576	0.000	0.000	8,33E-04	0.00E+00	0.00E+00
3575	3581	1.56	3576	3582	2.000	1.320	2.60E-02	3.33E-02	2.20E-02
3581	3587	1.61	3582	3588	1.490	1.820	2.68E-02	2.48E-02	3.03E-02
3587	3593	0.29	3588	3600	1.120	1.080	4,83E-03	1,87E-02	1,80E-02
3593	3600	0.93					1.55E-02		

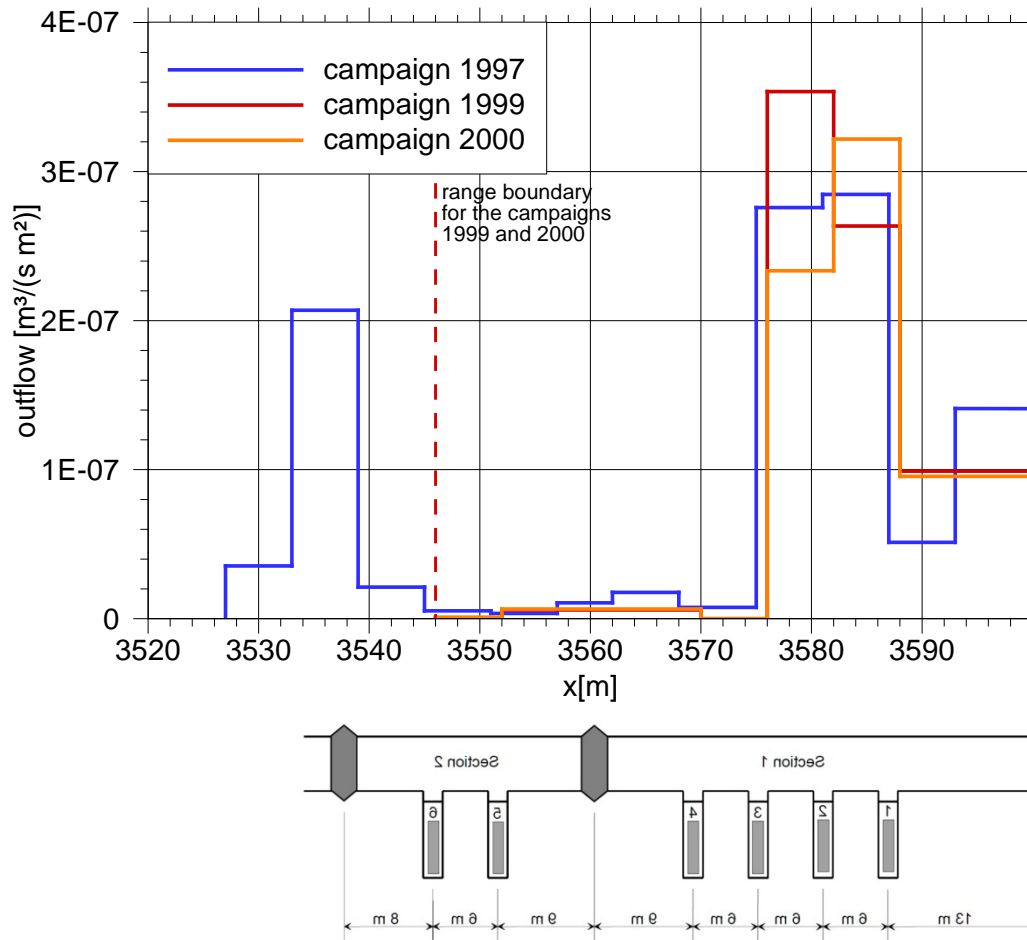


Fig. 3.8 Outflow into the PR-tunnel related to location of the deposition boreholes; sketch relating to the PR-tunnel after /VID 17/

Comparing mean outflow rates with data from the BRIE-site

The data for mass outflow from Tab. 3.3 is transformed into flux densities in Tab. 3.4. On the basis of flux densities the outflow rates into the PR-tunnel can be compared with those of the TASO-tunnel. For Task 8d an average value of $3.63 \cdot 10^{-9} \text{ m}^3/(\text{m}^2 \text{ s})$ had been estimated /KRÖ 17b/ for the tunnel surface without large fractures. Assuming the same geostatistics for the background fractures at the PR as for the BRIE-site the values marked in green compare well with a rate that is related to the absence of larger fractures. The colour coded data thus indicate a section in the PR-tunnel from 3545 m to 3575 m that is free of larger fractures.

Tab. 3.4 Outflow into the PR-tunnel in terms of flux densities; after /RHÉ 01/
marked in green are values less than 5 times the TASO reference value

Campaign 1997			Campaigns 1999 & 2000				Outflow		
Weir from [m]	sections to [m]	Q (1997) [L/min]	Weir from [m]	sections to [m]	Q (1999) [L/min]	Q (2000) [L/min]	1997	1999	2000
							[m ³ /(s m ²)]		
3527	3533	0.20					3.54E-08		
3533	3539	1.17					2.07E-07		
3539	3545	0.12					2.12E-08		
3545	3551	0.03	3546	3552	0.001	0.006	5.31E-09	1.77E-10	1.06E-09
3551	3557	0.02	3552	3570	0.100	0.110	3.54E-09	5.89E-09	6.48E-09
3557	3562	0.05					1.06E-08		
3562	3568	0.10					1.77E-08		
3568	3575	0.05	3570	3576	0.000	0.000	7.58E-09	0.00E+00	0.00E+00
3575	3581	1.56	3576	3582	2.000	1.320	2.76E-07	3.54E-07	2.33E-07
3581	3587	1.61	3582	3588	1.490	1.820	2.85E-07	2.63E-07	3.22E-07
3587	3593	0.29	3588	3600	1.120	1.080	5.13E-08	9.90E-08	9.55E-08
3593	3600	0.93					1.41E-07		

3.4.2 Deposition boreholes

There had been three different measurements in the deposition boreholes:

- total outflow into the deposition holes /RHÉ 01/ (see Tab. 3.5)
- localized outflow /RHÉ 01/ (see Tab. 3.6 and Fig. 3.9)
- diaper measurements in deposition holes 2 and 3 /RHÉ 01/ as well as 5 and 6 /FOR 05/ (see Fig. 3.10)

The results of the total outflow measurements are summarised in Tab. 3.5. Mean values are derived also where applicable. They indicate that total outflow varies by a factor of ± 2 around a value of $1.5 \cdot 10^{-04}$ l/min except in borehole 1 where total outflow exceeds this average by a factor of 53.

Local spots of comparatively high outflow into the boreholes had also been identified. The locations of these spots as well as the observed fracture trace lines are depicted in Fig. 3.9.

Tab. 3.5 Total outflow into the deposition boreholes; after /RHÉ 01/

borehole		representative total outflow rates				
		1999	2000/1	2000/2	mean	
code name	#	[l/min]				[kg/s]*
DA3587G01	1	0,0800	0,0787		0,0794	1,32E-03
DA3581G01	2	0,0016	0,0022		0,0019	3,17E-05
DA3575G01	3	0,0028	0,0031		0,0030	5,00E-05
DA3569G01	4	0,0007			0,0007	1,17E-05
DA3551G01	5		0,0016	0,0016	0,0016	2,67E-05
DA3545G01	6		0,0027		0,0027	4,50E-05

* Conversion from [l] to [kg] using a water density of 1000 kg/m³.

Relating the high outflow spots and the fracture trace lines the following observations can be made:

- The position of the four local outflow spots in **borehole 1** are neither aligned to a specific fracture trace nor do they indicate a trend that could be interpreted as a regular feature.
- In **boreholes 2 and 3** only one or no spot was found.
- In **borehole 4** three of the four spots are aligned to a subhorizontal fracture close to the tunnel floor indicating a relation to the EDZ rather than to the natural fracture system.
- Seven of nine spots in **borehole 5** indicate the position of a subvertical fracture. The remaining two spots are not apparently related to anything.
- All ten spots in **borehole 6** follow a trend that is consistent with about one half of a fracture being cut through by the borehole. Why there is not just one additional spot in the suspected other half is quite unclear.

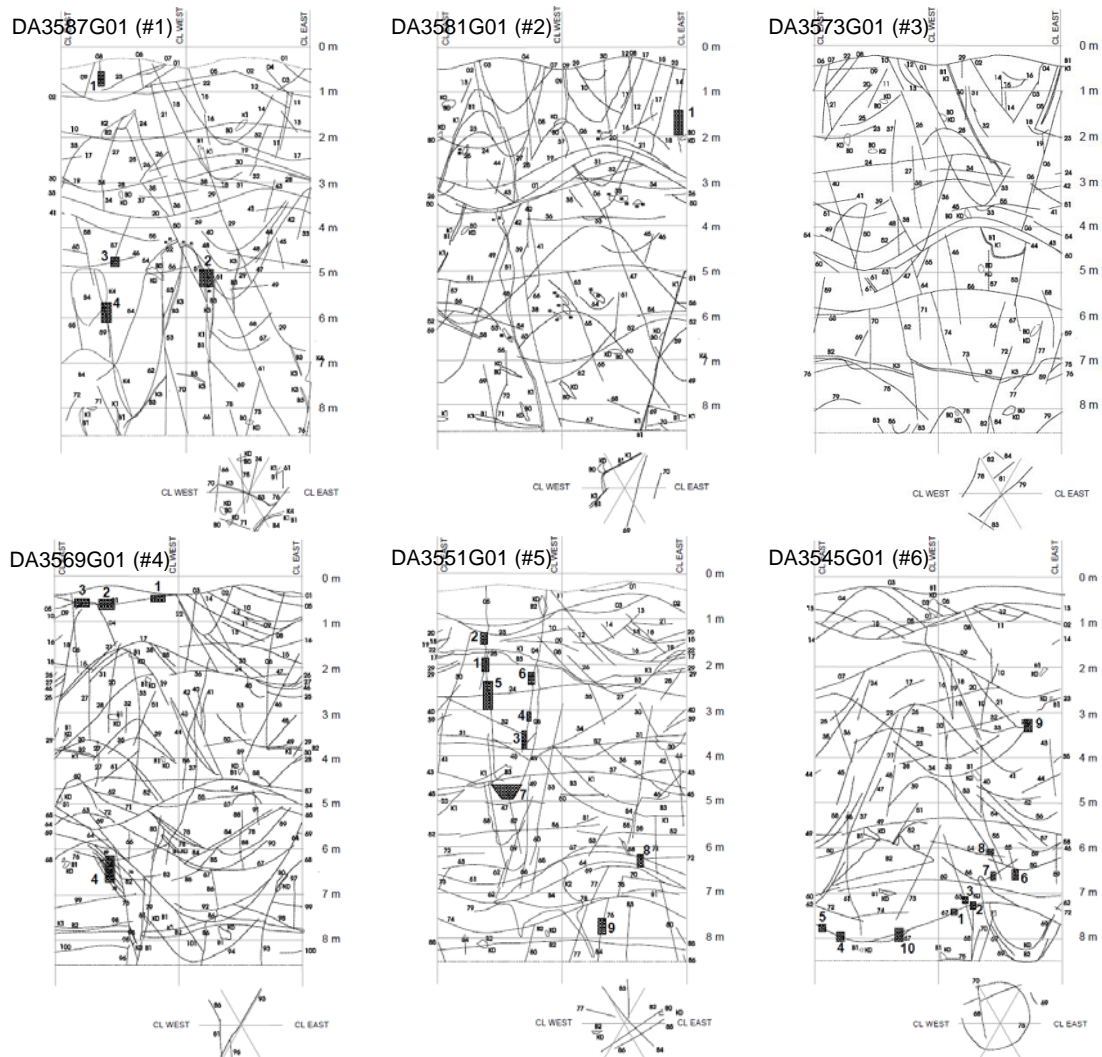


Fig. 3.9 Fracture traces and localised outflow locations in the deposition holes; localized outflow marked by pattern-filled polygons; from /RHÉ 01/

Note that the features seemingly identified in boreholes 5 and 6 bear no resemblance with the deterministic features detected by /RHÉ 01/ (see Fig. 3.9 and Fig. 3.7).

Outflow rates for the spots shown in Fig. 3.9 are compiled in Tab. 3.6 as well as the number of outflow locations and the resulting mean outflow rate per location. The local outflow rates thus seem to vary within a bandwidth of an order of magnitude, but none at all could be detected in borehole 3.

Tab. 3.6 Localised outflow into the deposition boreholes; after /RHÉ 01/

Borehole no.		localised outflow		number of local outflow locations	mean outflow rate
Code name	#	[10 ⁻⁵ l/min]	[kg/s] ⁷		[10 ⁻⁵ l/min]
DA3587G01	1	15,8	2,63E-06	4	3,95
DA3581G01	2	16,7	2,78E-06	1	16,70
DA3575G01	3	0	0	0	0
DA3569G01	4	5,24	8,73E-07	4	1,31
DA3551G01	5	35,9	5,98E-06	9	3,99
DA3545G01	6	59,5	9,92E-06	10	5,95

The difference between total and localized outflow gives an idea about the areal outflow rate which is taken here to be a mean distributed outflow that can be ascribed to the undisturbed matrix including background fractures. Total localised and distributed outflow rates are summarized in Tab. 3.7. The contribution of the localized outflow accounts for up to 23 % of the total outflow except for borehole 1 where localised outflow is negligible in comparison to the total outflow and for borehole 3 where no localised outflow had been measured.

Tab. 3.7 Total, localised and areal outflow into the deposition boreholes

Borehole no.		total outflow		localised outflow		(local outflow)/(total outflow)	areal outflow	
Code name	#	[l/min]	[kg/s]	[l/min]	[kg/s]	[%]	[l/min]	[kg/s]
DA3587G01	1	0,0794	1,32E-03	1,58E-04	2,63E-06	0,20	0,0792	1,32E-03
DA3581G01	2	0,0019	3,17E-05	1,67E-04	2,78E-06	8,79	0,0017	2,89E-05
DA3575G01	3	0,0030	5,00E-05	0	0	0,00	0,0030	4,92E-05
DA3569G01	4	0,0007	1,17E-05	5,24E-05	8,73E-07	7,28	0,0007	1,11E-05
DA3551G01	5	0,0016	2,67E-05	3,59E-04	5,98E-06	22,79	0,0012	2,03E-05
DA3545G01	6	0,0027	4,50E-05	5,95E-04	9,92E-06	21,88	0,0021	3,54E-05

Somewhat unexpected from the data discussed so far is the fact that total outflow into borehole 1 is drastically increased in comparison to the other boreholes while the localised outflow appears to be in line with the overall level of outflow of all other boreholes (except hole 3). The fracture trace map of borehole 1 does not show a cross-section with a major fracture thus rather indicating that a highly increased number of local smaller

fractures (which could be called a “deformation zone” for want of a better expression) might account for the high water outflow rate. However, there appears to be a small deterministic fractures connected to borehole 1 which in turn is connected to a large fracture as shown in Fig. 3.7. This constellation could easily explain the high outflow.

Equally remarkable is the fact that borehole 3 shows the highest total outflow rate of boreholes 2 to 6 but shows no significant local outflow spot. This might be the consequence of a certain variability in the permeability field created by background fractures whose outflow rates were below the detection limit. However, by and large it has to be concluded that the localised outflow spots appear to be a rather weak indication of relevant water bearing fractures.

In boreholes 2, 3, 5, and 6 arrays of diapers had been installed for a certain period of time⁷ to investigate the outflow distribution in the boreholes. The derived flow rates are visualized in Fig. 3.10. Total flow into borehole 3 was estimated to be approximately $3 \cdot 10^{-3}$ l/min which is consistent with the value from Tab. 3.7. In case of boreholes 5 and 6 the sum of the derived outflow rates for all diapers amounts to $1.6 \cdot 10^{-4}$ l/min and $3.1 \cdot 10^{-4}$ l/min, respectively. This is about 1/10 of the total outflow rates as given in Tab. 3.7.

A characteristic pattern can be observed in Fig. 3.10. The areas of high outflow as shown in Fig. 3.10 are generally rather elongated, more or less vertically orientated being broad at the top and narrow at the bottom. Such a pattern suggests rather flow from the top of the borehole than flow from the borehole wall especially as the majority originates in the first diaper row.

There appears to be a relation between wetting of the diapers and location 1 in deposition hole DA3581G01 as well as locations 7 and 8 in DA3551G01. But again the same top to bottom pattern seemingly originating at these locations can be observed. Otherwise, there is no significant relation between the wetted diapers and specific fractures. The results of the diaper tests provide therefore no indication of vertical fractures being opened by the deposition holes.

⁷ In case of the earlier measurements no specific period of time is given. For the deposition holes in section II the tests lasted about a week /FOR 05/.

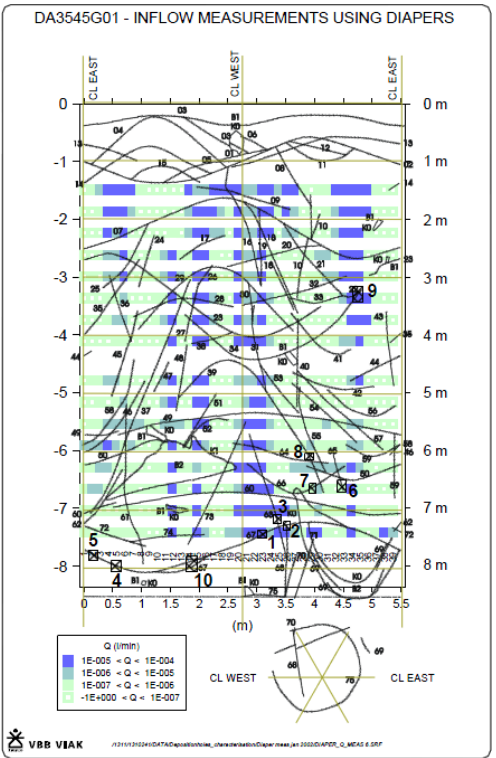
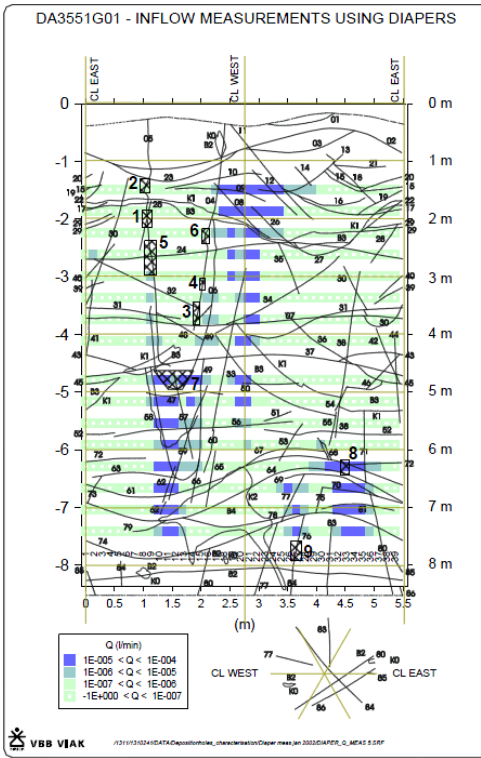
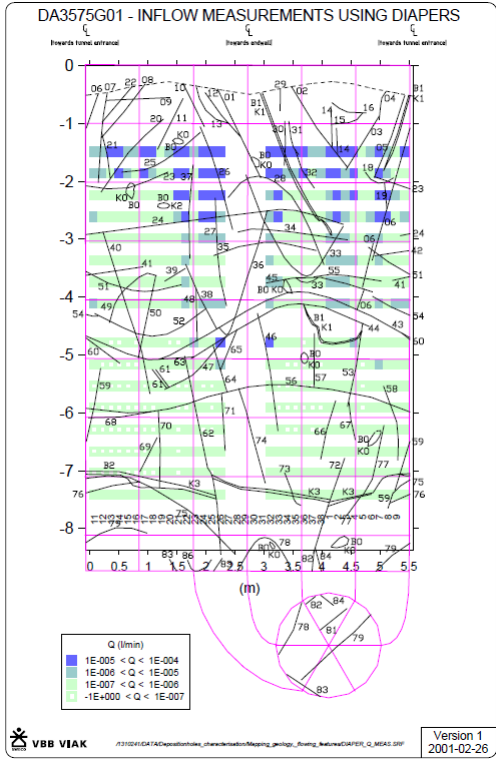
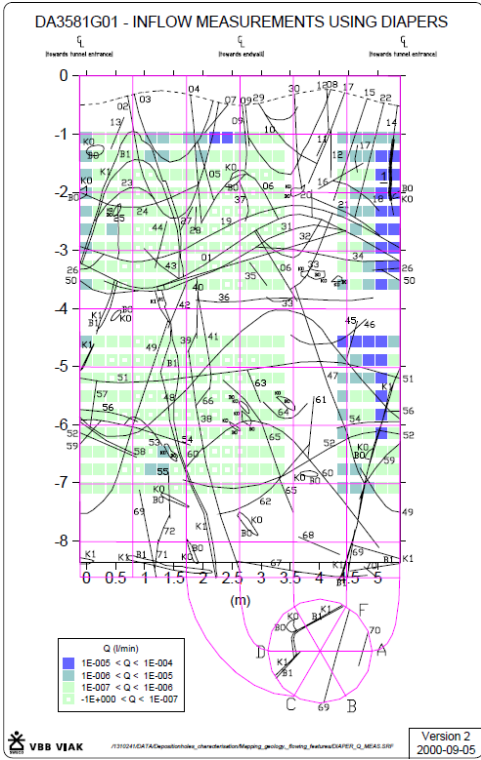


Fig. 3.10 Outflow from diaper measurements; localized outflow marked by black pattern-filled polygons; top row from /RHÉ 01/ and lower row from /FOR 05/

3.4.3 Other drifts

Additional weir tests had been performed in different tunnels and tunnel sections. Estimations about outflow into the PR as well as neighbouring drifts are shown in Fig. 3.11. The measured data as well as the resulting average flow rate per metre tunnel are compiled in Tab. 3.8.

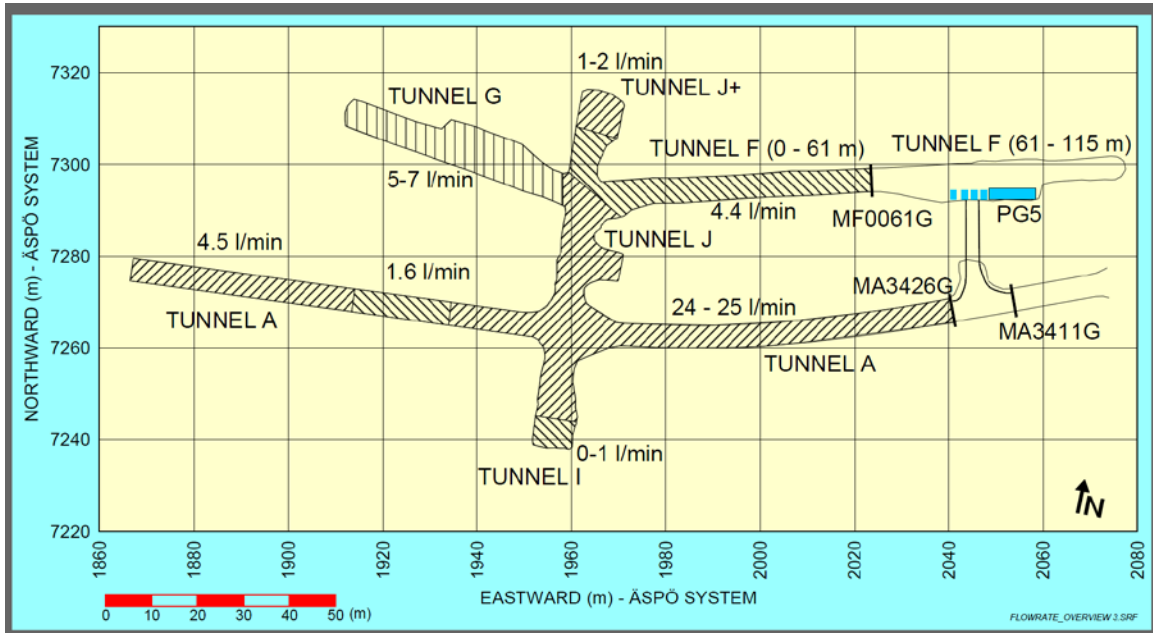


Fig. 3.11 Estimated outflow into different tunnel sections; from /RHÉ 01/

The outflow rate for the PR-tunnel thus amounts to 0.084 l/min per metre tunnel or $8.9 \cdot 10^{-8} \text{ m}^3/(\text{s m}^2)$ referring to the tunnel surface. As a rule of thumb an average value of 0.1 l/(min m) or $1.1 \cdot 10^{-7} \text{ m}^3/(\text{s m}^2)$ applies to the whole investigated tunnel system. Note that this average includes outflow from strongly water-producing local fractures. These data are therefore of very limited use for model calibration if these local features are not taken into account.

Tab. 3.8 Outflow (absolute and per metre tunnel) into the drift system; from /RHÉ 01/

Tunnel ID	Tunnel secup (m)	Tunnel seclow (m)	Meas. period	Weir	Flow rate L/min	Flow rate per m tunnel (l/(min·m))	Comments
A	3527	3600	1997	Temporary weirs	6.13	0.084	
A	3546	3600	1999-2000	Temporary weirs	4.50	0.083	
F J+	61 0	115 10.6	1995	-	6	0.11	
F J+	0 0	61 10.6	1996-07	MF0061G	4.40 (1)	0.061	Some flow from J+
F J+	0 0	61 22.6	1996-12	MF0061G	6.20 (2)	0.074	Flow from J+ prob. 1.8 L/min
J (J+)	40 (10.6)	52 (22.6)	1996-12	MF0061G	1-2 (3)	0.08 – 0.16	Estimated from measurements (2) – (1)
F J+ G	0 0 0	61 22.6 52	1999	MF0061G	7.9 (4)	-	Probably only parts of the flow from tunnel G.
A I J	3426 0 0	3600 15 26	1996-08	MA3426G	31.2 (5)	0.14	
A I J G	3426 0 0 0	3600 25 26 52	1999	MA3426G	37.6 (6)	(0.13)	Flow rate per m tunnel, not entirely correct as some water from tunnel G probably goes to MF0061G.
I	15	25	1999	MA3426G	0-1 (7)	0 – 0.1	
G	0	52	1999	MF0016G MF3426G	5-7	0.10 – 0.13	Estimated from measurements (6)-(5)-(7)+(4)-(2)-(3)

3.5 Hydraulic properties

3.5.1 Matrix and background fractures

Six core measurements presented by /VIL 07/ for the rock matrix at the Forsmark site – which is believed to be comparable to the rock at Äspö – indicated a spectrum for the matrix permeability roughly ranging from 10^{-21} m² to 10^{-19} m². A fractured network model for the undisturbed rock points in the direction of slightly less than 10^{-20} m² /SVE 12/. New laboratory tests on de-stressed matrix core samples showed a range of permeability values between $6 \cdot 10^{-21}$ m² and $9 \cdot 10^{-20}$ m² /VID 17/. Measurements at GRS on core samples from the BRIE-site resulted in a gas permeability of roundabout 3 to $6 \cdot 10^{-20}$ m².

Initially the matrix in the models for Task 8b-d had been considered to be “undisturbed” or “intact”⁸. A permeability of 10^{-20} m² had therefore been adopted. During model calibration, however, the strong influence of the background fractures had become apparent increasing the overall permeability of matrix and background fractures up to 10^{-17} m² /KRÖ 17b/. The latter thus became a starting value for the model calibration.

3.5.2 Fractures

According to the considerations in Appendix B eight detected and one assumed fracture are taken into account for the model. Location, orientation, size and permeability of the detected fractures are compiled in Tab. 3.9. The additionally assumed fracture in the model is actually a copy of the northern major fracture where strike was slightly modified. This applies also to the permeability. In contrast to the permeability of the detected fractures this parameter was open to variation in the course of calibration, though.

Tab. 3.9 Characterisation of the deterministic fractures; mainly from /RHÉ 01/

feature	centre coordinates			strike	dip	radius	transmissivity ⁹
	x	y	z				
	[m]	[m]	[m] (amsl)	[°]	[°]	[m]	[m ² /s]
Northern major fracture ¹⁰	1892	7289	-449	118	88	20	$5 - 10 \cdot 10^{-8}$
Southern major fracture	1887	7266	-449	124	89	20	$7 - 9 \cdot 10^{-8}$
minor fracture 1	1878.28	7275.03	-453.53	354	79	2	$8.1 \cdot 10^{-9}$
minor fracture 2	1915.42	7271.06	-455.24	312	40	2	$4.7 \cdot 10^{-9}$
minor fracture 3	1917.50	7269.90	-455.56	271	38	2	$3.3 \cdot 10^{-9}$
minor fracture 4	1919.55	7268.80	-456.66	278	24	2	$1.7 \cdot 10^{-9}$
minor fracture 5	1919.55	7268.80	-453.54	164	64	2	$2.8 \cdot 10^{-10}$
minor fracture 6	1921.45	7270.22	-453.14	298	64	2	$1.3 \cdot 10^{-8}$
Assumed fracture	1153.18	7775.34	-435.30	126	88	20	$5 - 10 \cdot 10^{-8}$

⁸ For a discussion of the expression “intact rock”: see section 2.2.2.

⁹ For conversion of the transmissivity T into a hydraulic conductivity K it is necessary to define a more or less arbitrary fracture aperture d. The formula reads then: $K=T/d$.

¹⁰ Note that the northern major fracture has been modified according to Appendix B to an ellipsoid which still has a vertical diameter of 40 m.

3.6 Influence of salinity

No significant salinity variation had been found at the BRIE-site that would have influenced groundwater flow /KRÖ 17b/. The same is assumed to apply to the PR-site.

4 Isothermal flow model

4.1 Model domain

The model consists basically of three 3d-components: the matrix, the skin around the geotechnical openings and the fractures. They are depicted in Fig. 4.1 and Fig. 4.2, respectively. The model comprises four tunnels called S-, PR- G- and IJ-tunnel here, and two extensions to the J-tunnel called I- and J+-tunnel. The six deposition holes drilled from the PR-tunnel are also enveloped in a skin zone like the tunnels. Additionally, there are three major and six minor deterministic fractures (the northern and the southern as well as the assumed fracture plus minor fractures M1 to M6). Only the assumed fracture cross-sections the model surface (see Fig. 4.3) and only fracture M3 does not cut through the PR-tunnel or a deposition borehole.

The 3d-elements are grouped in so-called subsets with individual names. These names are also given in Fig. 4.2 except for the six minor fractures which are too small to be differentiated at this scale. They are depicted as close-ups in Fig. 4.4 and Fig. 4.5.

Model size is approximately 150 m x 200 m x 50 m. The coordinates of the eight corner nodes are compiled in Tab. 4.1.

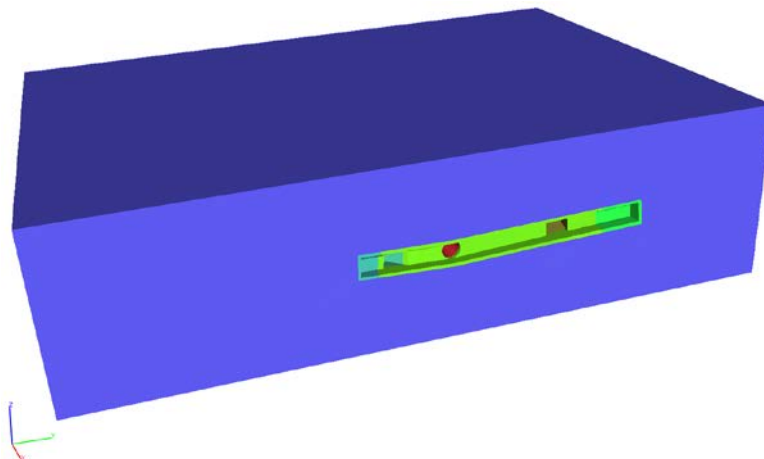


Fig. 4.1 Matrix block including cut through the IJ-tunnel

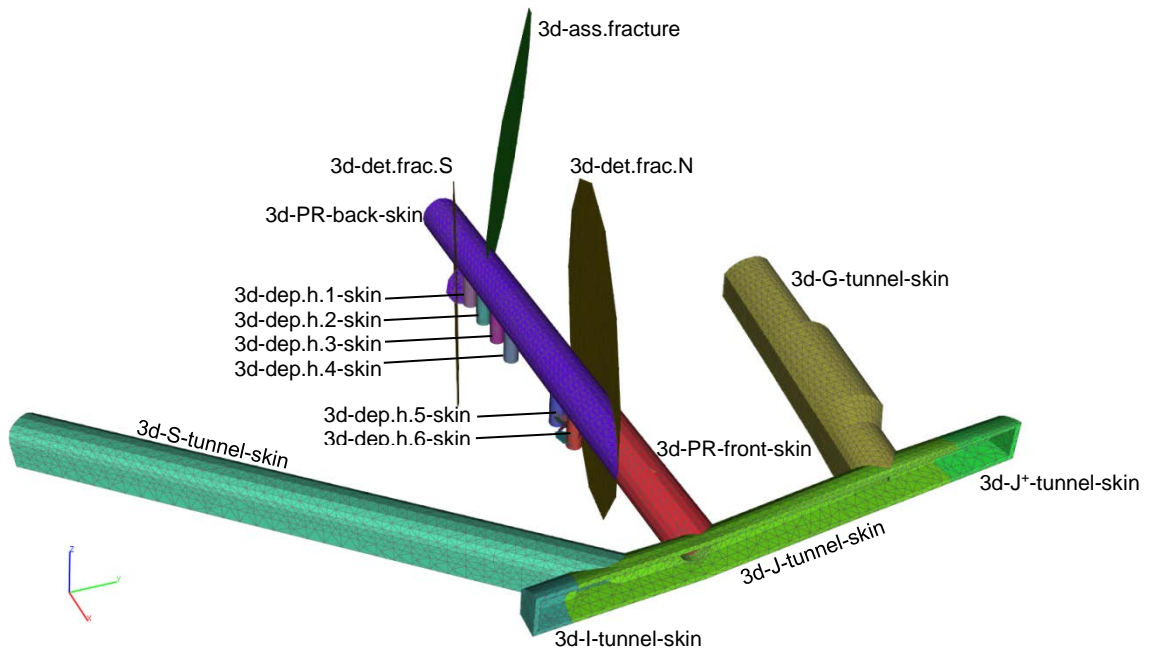


Fig. 4.2 3d-subsets of the model (except matrix) including their names

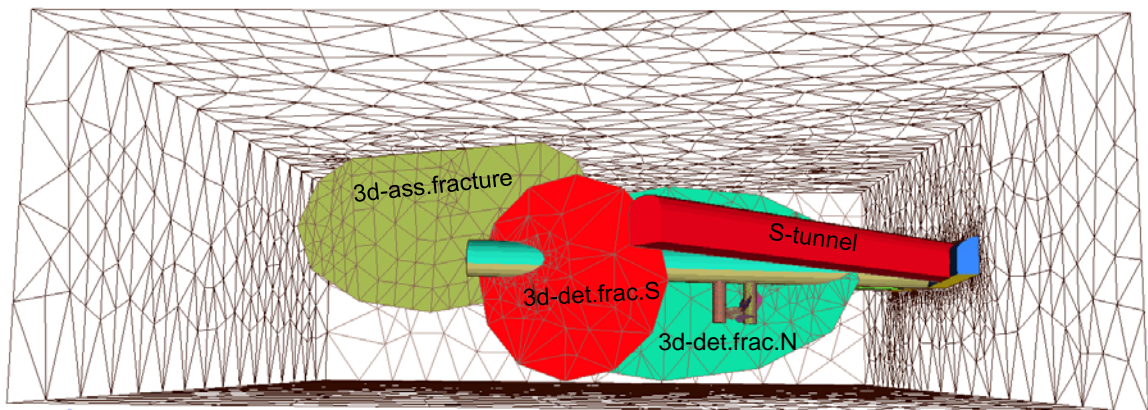


Fig. 4.3 Relation of large fractures to the outer model surface

Tab. 4.1 Coordinates of the nodes of the boundary box

x	y	z
1100	7636	-444.5
1309.5	7636	-444.5
1309.5	7836	-444.5
1100	7836	-444.5
1100	7636	-528
1309.5	7636	-528
1309.5	7836	-528
1100	7836	-528

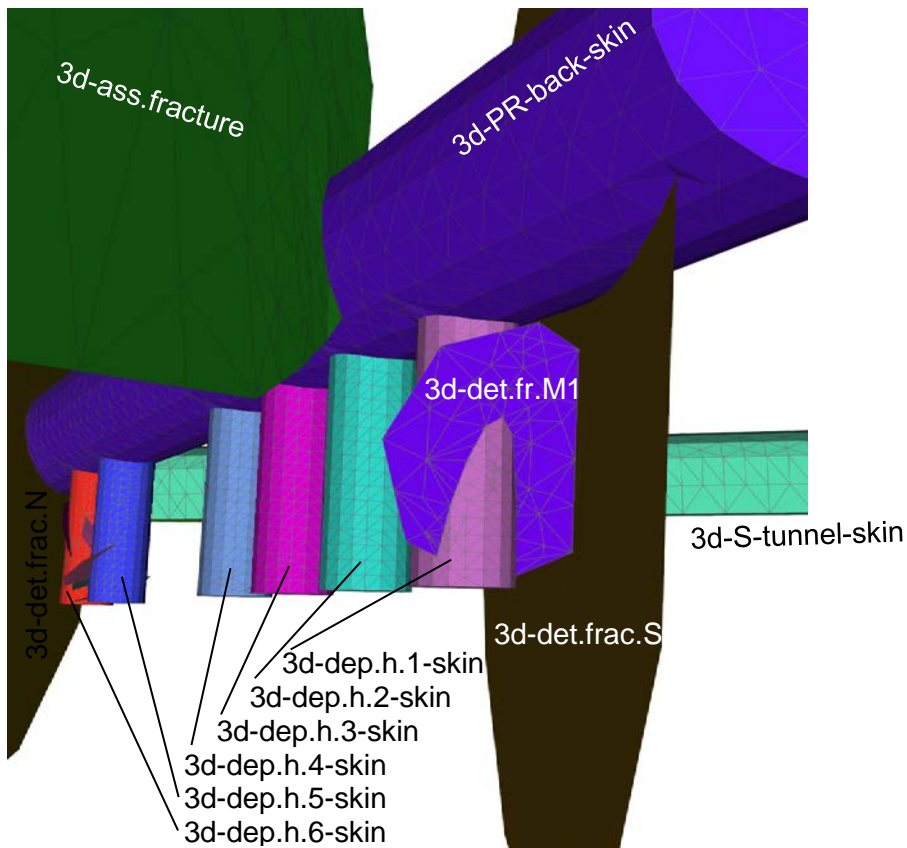


Fig. 4.4 3d-subsets of the model; close-up at the end of the PR tunnel

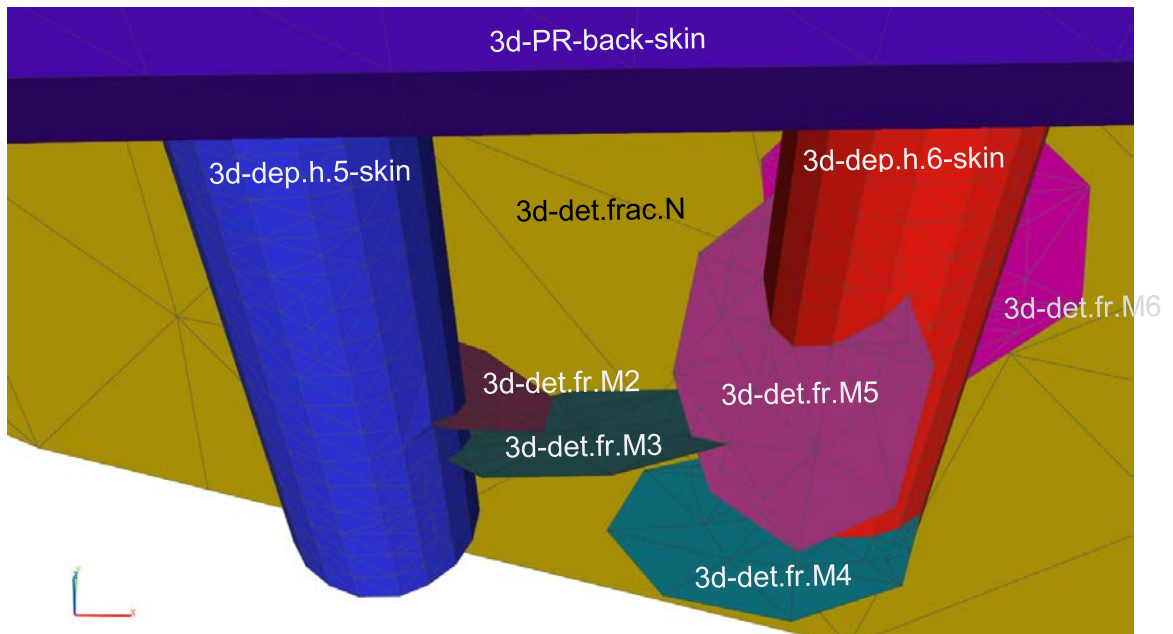


Fig. 4.5 3d-subsets of the model; close-up at deposition boreholes 5 and 6

4.2 Hydraulic properties

Permeability values for matrix and skin in the reference model were taken over from the modelling exercise for the BRIE /KRÖ 17b/. The data for the fractures were given in terms of transmissivities which had to be transformed into permeabilities for modelling purposes. These two quantities can be related with the help of an arbitrary fracture width which was chosen here to be 1 cm. Since steady-state conditions were assumed, porosity is not required. The data used for the reference model are compiled in Tab. 4.2.

Tab. 4.2 Hydraulic data

Subset name	Subset number	Permeability [m ²]	Transmissivity [m ² /s]
3d-matrix	73	10 ⁻¹⁷	not applicable
3d-PR-back-skin	74	10 ⁻¹⁸ *)	not applicable
3d-PR-front-skin	75		
3d-dep.h.1-skin	76	10 ⁻¹⁸ *)	not applicable
3d-dep.h.2-skin	77		
3d-dep.h.3-skin	78		
3d-dep.h.4-skin	79		
3d-dep.h.5-skin	80		
3d-dep.h.6-skin	81		
3d-S-skin	82	10 ⁻¹⁸ *)	not applicable
3d-G-skin	83		
3d-IJ-skin	84		
3d-l+-skin	85		
3d-J+-skin	86		
3d-det.frac.N	87	8 · 10 ⁻¹³ **)	5 – 10 · 10 ⁻⁸
3d-det.frac.S	88	8 · 10 ⁻¹³ **)	7 – 9 · 10 ⁻⁸
3d-det.fr.M1	89	8 · 10 ⁻¹⁴ **)	8.1 · 10 ⁻⁹
3d-det.fr.M2	90	5 · 10 ⁻¹⁴ **)	4.7 · 10 ⁻⁹
3d-det.fr.M3	91	3 · 10 ⁻¹⁴ **)	3.3 · 10 ⁻⁹
3d-det.fr.M4	92	2 · 10 ⁻¹⁴ **)	1.7 · 10 ⁻⁹
3d-det.fr.M5	93	3 · 10 ⁻¹⁵ **)	2.8 · 10 ⁻¹⁰
3d-det.fr.M6	94	1 · 10 ⁻¹³ **)	1.3 · 10 ⁻⁸
3d-ass.fracture	95	8 · 10 ⁻¹³ **)	5 – 10 · 10 ⁻⁸
3d-det.frac.N-skin	96	8 · 10 ⁻¹⁴ ***)	not used
3d-det.frac.S-skin	97	8 · 10 ⁻¹⁴ ***)	
3d-det.fr.M1-skin	98	8 · 10 ⁻¹⁵ ***)	
3d-det.fr.M2-skin	99	5 · 10 ⁻¹⁵ ***)	
3d-det.fr.M3-skin	100	3 · 10 ⁻¹⁵ ***)	
3d-det.fr.M4-skin	101	1 · 10 ⁻¹⁵ ***)	
3d-det.fr.M5-skin	102	3 · 10 ⁻¹⁶ ***)	
3d-det.fr.M6-skin	103	1 · 10 ⁻¹⁴ ***)	
3d-ass.frac-skin	104	8 · 10 ⁻¹⁴ ***)	

*) 1/10 of matrix value

**) estimated for a fracture width of 1 cm

***) 1/10 of fracture value

4.3 Boundary conditions

The isothermal flow model requires only pressure boundary conditions. These fall into two categories: pressure data for the matrix at the outer surface of the model and atmospheric pressure at the surface of the geotechnical openings. Fig. 4.6 shows the outer surface of the model as a wire frame representation and the geotechnical openings as solid coloured objects.

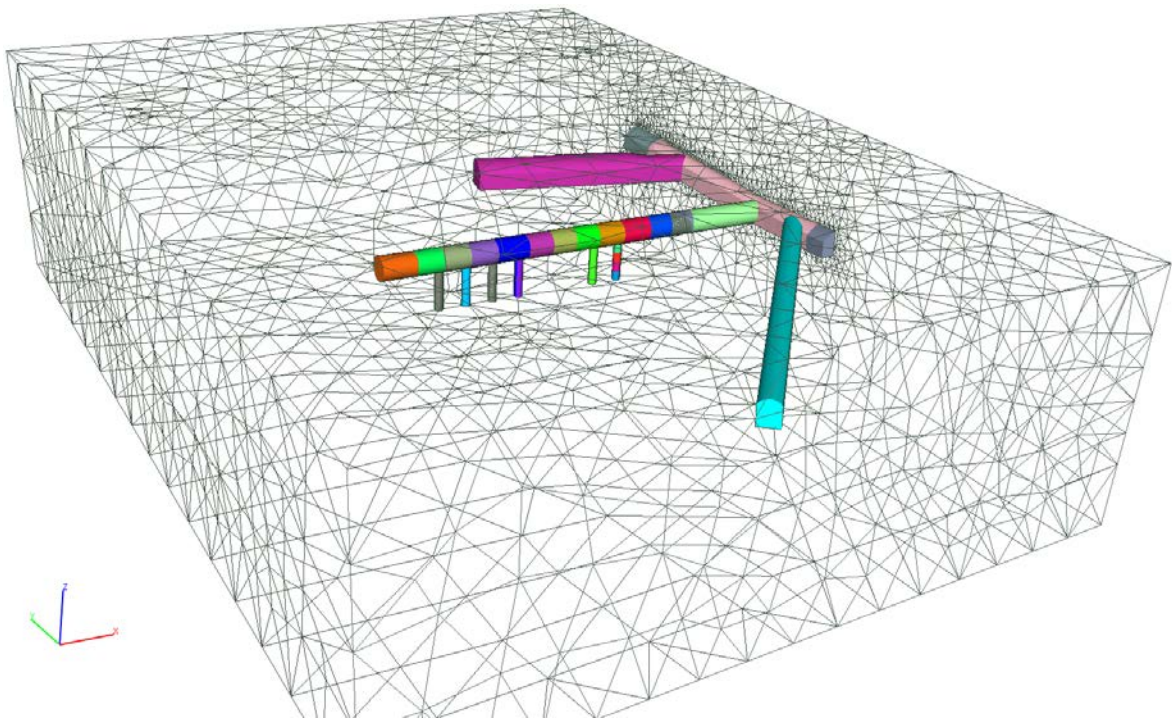


Fig. 4.6 Visualization of 2d-subsets with boundary conditions;
wire frame: outer surface of the model,
coloured solids: geotechnical openings

Pressure data for the matrix had been provided along with the task description as a 3d-cloud of data points and had to be pre-processed by means of an inverse distance weighing scheme to extract appropriate values at the outer model surface. Note that this surface includes the assumed fracture where it cuts through the top of the model (see Fig. 4.3). A list of the related subsets can be found in Tab. 4.3. The resulting pressure distribution is shown in Fig. 4.7.

Tab. 4.3 Subsets with pressure data from the rock (see Fig. 4.7)

Subset name	Subset number
box-top / 1d-ass.frac.top	0 105
box-E / box-E-skin	4 6
box-S	1
box-W	2
box-N	3
box-bottom	5

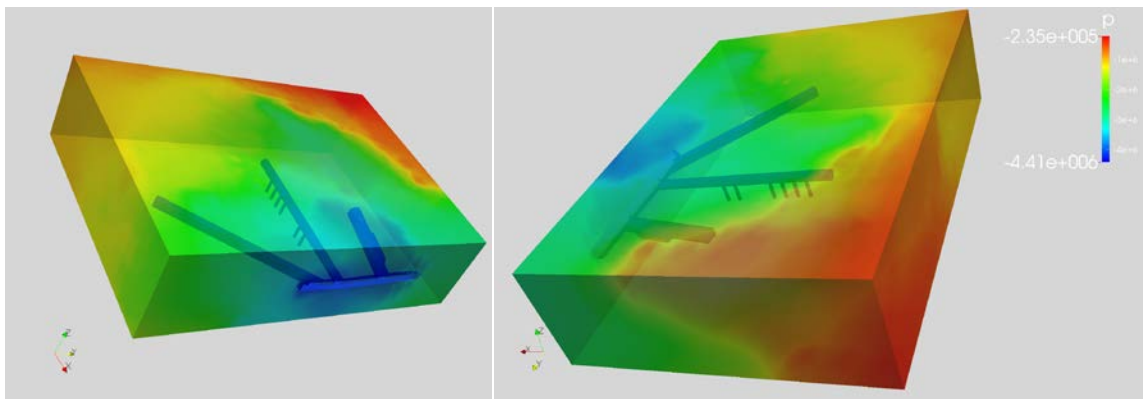


Fig. 4.7 Prescribed pressure distribution at the model boundaries

Like in the BRIE /KRÖ 17b/ the measured humidity in the PR-tunnel as well as in the deposition boreholes was very high. The referring data is discussed in Appendix A. This observation indicates a high degree of saturation close to the surface of the geotechnical openings thus supporting the notion of single-phase flow in the rock. Atmospheric pressure was therefore assigned here in the model.

Different areas of the inner surface of the PR-tunnel were allocated to different subsets in such a way that outflow from a subset relates to a corresponding outflow measurement in the field. Fig. 4.8 depicts the 2d-subsets representing areal outflow from the tunnel surface or the deposition boreholes and includes the subset names for reference.

The surface of the geotechnical openings include again the fractures that had been cut by excavation. The boundary edges of the fractures at the tunnel surface are a bit more difficult to visualize in a comprehensible way so that Fig. 4.9 shows actually four variants of the same view, with or without other subsets interfering with the view and with or with-

out the related fractures. All subsets with assigned atmospheric boundary conditions are listed in Tab. 4.4.

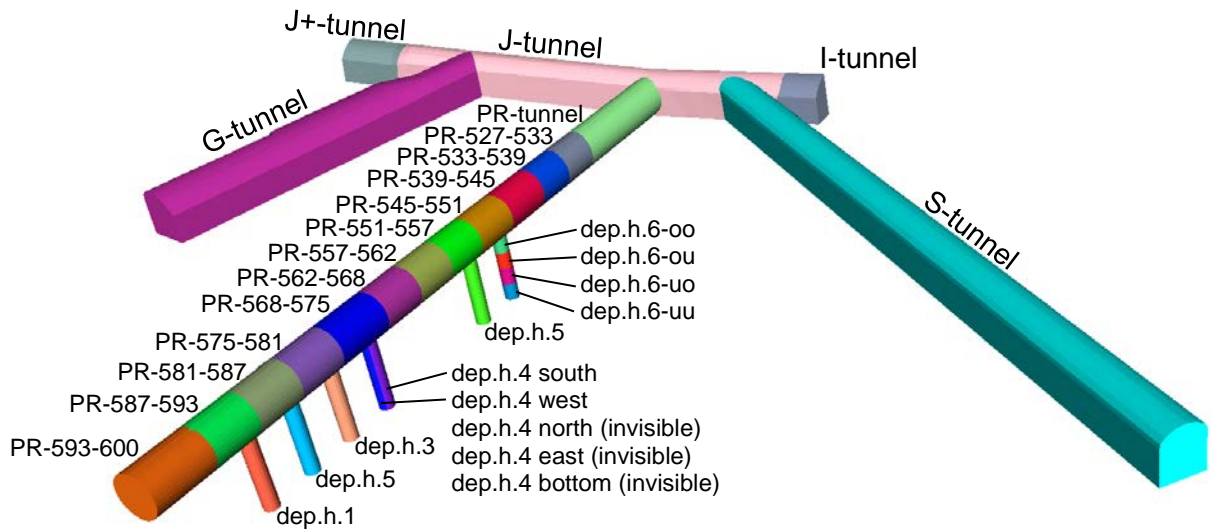


Fig. 4.8 2d-subsets of the model to which atmospheric pressure is assigned

Tab. 4.4 Subsets with atmospheric pressure

Subset name	Subset number	Subset name	Subset number
S-tunnel	7	dep.h.1	25
IJ-tunnel	8	dep.h.2	26
I+-tunnel	9	dep.h.3	27
J+-tunnel	10	dep.h.4 bottom	28
PR-tunnel	11	dep.h.4 east	29
PR-527-533	12	dep.h.4 north	30
PR-533-539	13	dep.h.4 west	31
PR-539-545	14	dep.h.4 south	32
PR-545-551	15	dep.h.5	33
PR-551-557	16	dep.h.6-oo	34
PR-557-562	17	dep.h.6-ou	35
PR-562-568	18	dep.h.6-uo	36
PR-568-575	19	dep.h.6-uu	37
PR-575-581	20	1d-det.frac.S	106
PR-581-587	21	1d-det.fr.M2	107
PR-587-593	22	1d-det.fr.M5	108
PR-593-600	23	1d-det.fr.M6	109
G-tunnel	24	1d-ass.fracture	110
		1d-det.frac.N	111
		1d-det.fr.M1	112
		1d-det.fr.M4	113

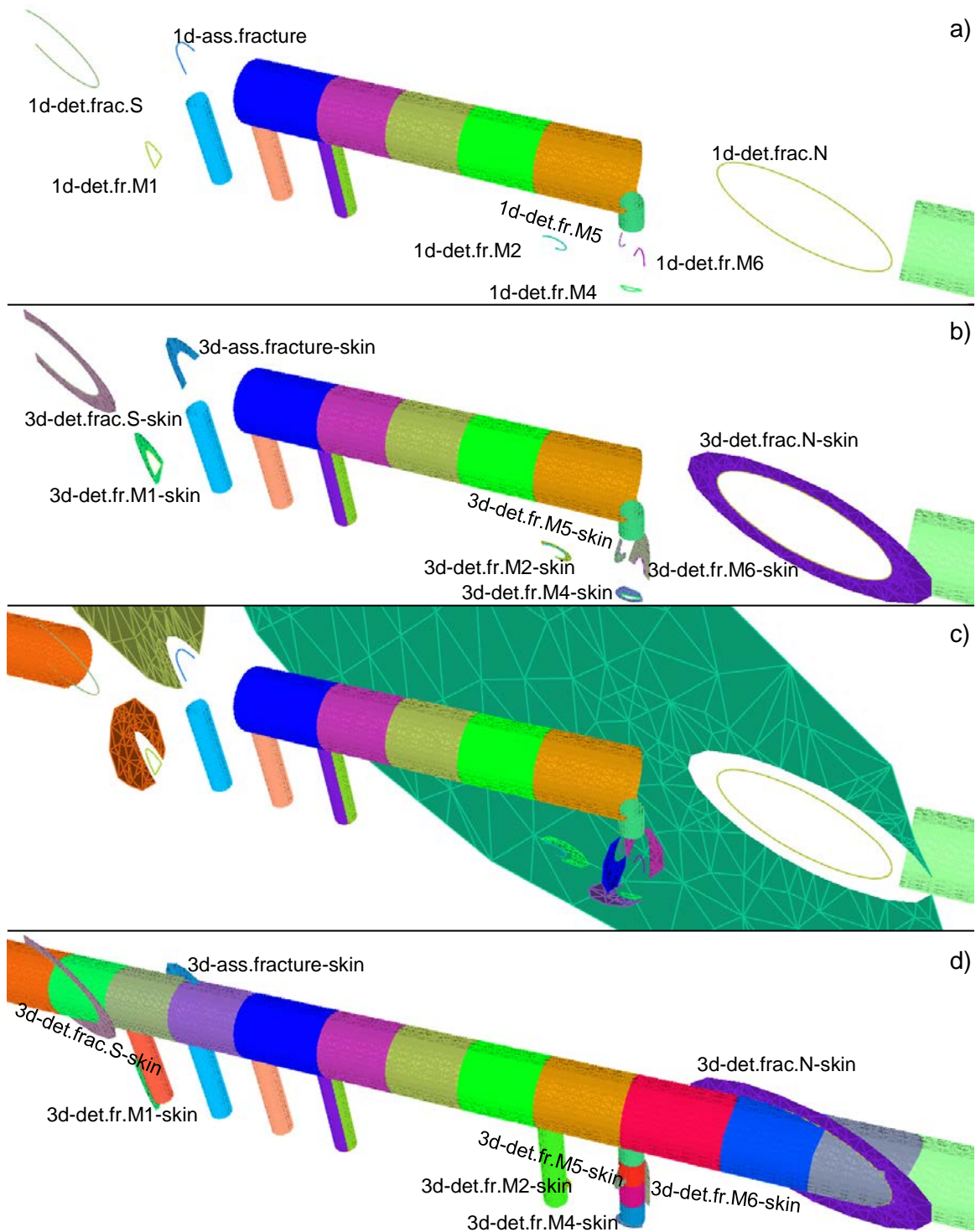


Fig. 4.9 Visualization of fracture boundary edges with boundary conditions;
a) only boundary edges and some parts of tunnel and boreholes missing
b) as a) plus parts of fractures within the skin
c) as a) plus parts of fractures outside the skin
d) as b) with all parts of tunnel and boreholes

4.4 Calibration targets

Calibration of the steady-state, single-phase, and isothermal flow model is based on the following data on outflow:

- Outflow into sections of the PR-tunnel (see section 3.4.1)
- Total outflow into deposition boreholes (see section 3.4.2)
- Outflow into G-, I-, and J+ tunnel, respectively (see section 3.4.3)

In the previous section Fig. 4.8 had shown the 2d-subsets to which atmospheric pressure had been assigned as boundary conditions. For each of these subsets outflow can be calculated. Note that Fig. 4.8 also shows that the surfaces of deposition holes 4 and 6 are subdivided to allow for a closer inspection of circumferential and vertical distribution of the outflow into these holes. The target outflow values for calibration are compiled in Tab. 4.5 to Tab. 4.7.

Tab. 4.5 Outflow into the sections of the PR-tunnel; after /RHÉ 01/

weir section			adopted outflow ranges
from	to	subset name	[kg/s]
[m]	[m]		
3527	3533	PR-527-533	$3.33 \cdot 10^{-3}$
3533	3539	PR-533-539	$1.95 \cdot 10^{-2}$
3539	3545	PR-539-545	$2.00 \cdot 10^{-3}$
3545	3551	PR-545-551	$1.67 \cdot 10^{-5} - 5.00 \cdot 10^{-4}$
3551	3557	PR-551-557	$3.33 \cdot 10^{-4} - 1.83 \cdot 10^{-3}$
3557	3562	PR-557-562	$8.33 \cdot 10^{-4} - 1.83 \cdot 10^{-3}$
3562	3568	PR-562-568	$1.67 \cdot 10^{-3} - 1.83 \cdot 10^{-3}$
3568	3575	PR-568-575	$< 8.33 \cdot 10^{-4}$
3575	3581	PR-575-581	$2,20 \cdot 10^{-2} - 3.33 \cdot 10^{-2}$
3581	3587	PR-581-587	$2.48 \cdot 10^{-2} - 3,03 \cdot 10^{-2}$
3587	3593	PR-587-593	$4,83 \cdot 10^{-3} - 1.87 \cdot 10^{-3}$
3593	3600	PR-593-600	$1.55 \cdot 10^{-2} - 1.87 \cdot 10^{-3}$

Tab. 4.6 Outflow into the deposition boreholes; after /RHÉ 01/

borehole		representative total outflow rates [kg/s]
code name	subset name	
DA3587G01	dep.h.1	$1.32 \cdot 10^{-2}$
DA3581G01	dep.h.2	$3.17 \cdot 10^{-5}$
DA3575G01	dep.h.3	$5.00 \cdot 10^{-5}$
DA3569G01	dep.h.4	$1.17 \cdot 10^{-5}$
DA3551G01	dep.h.5	$2.67 \cdot 10^{-5}$
DA3545G01	dep.h.6	$4.50 \cdot 10^{-5}$

Tab. 4.7 Outflow into other drifts; after /RHÉ 01/

tunnel		representative total outflow rates	
code name	subset name	[l/min]	[kg/s]
TASG	G-tunnel	5 - 7	$8.33 \cdot 10^{-2} - 0.117$
TASI	I-tunnel	< 1	$< 1.67 \cdot 10^{-2}$
TASJ+	J+-tunnel	1 - 2	$1.67 \cdot 10^{-2} - 3.33 \cdot 10^{-2}$

5 Heat transport model

5.1 Model domain

The heat transport model encompasses the same volume as the groundwater flow model. However, there are some differences in the model domains. As it is assumed that the structural difference between the skin zone and the matrix has no impact on heat flow, the thermal model does not differentiate between these two subdomains. In the same way also the fractures are believed to be thermally “invisible” and do therefore not appear in the model.

While the flow model represents the pre-installation phase of the Prototype Repository (PR), heat can obviously only be introduced after the installation of heaters during the operational phase of the experiment. The deposition boreholes thus contain the heaters as well as compacted bentonite filling the remaining space of the boreholes. In the PR-tunnel backfill composed of a mixture of crushed rock and bentonite and the plugs made of highly compacted bentonite were installed. Simplifying the model the plugs were treated like the backfill. The resulting model domain is depicted in Fig. 5.1. 73435 volumetric elements were used for the numerical grid.

5.2 Thermal properties

5.2.1 Rock

After an extensive effort by /SUN 05/ to characterize the rock at the PR the sensitivity analysis of the PR-site concerning temperature evolution by /KRI 07/ suggests a singular value of 2.72 W/(m K) as the relevant effective thermal conductivity for the rock.

Heat capacities for the minerals constituting the rock types encountered at Äspö have been compiled and a mean weighted by volume fractions has been calculated /PAT 97/. The results for the different rock types are compiled in Tab. 5.1. They show very little variation so that a value of 770 J/(kg K) is assumed to be representative for all rock types.

As the porosity of the rock is less than 1 % the impact of pore water on the bulk values of the thermal rock properties is considered to be negligible regardless of a possibly varying degree of saturation.

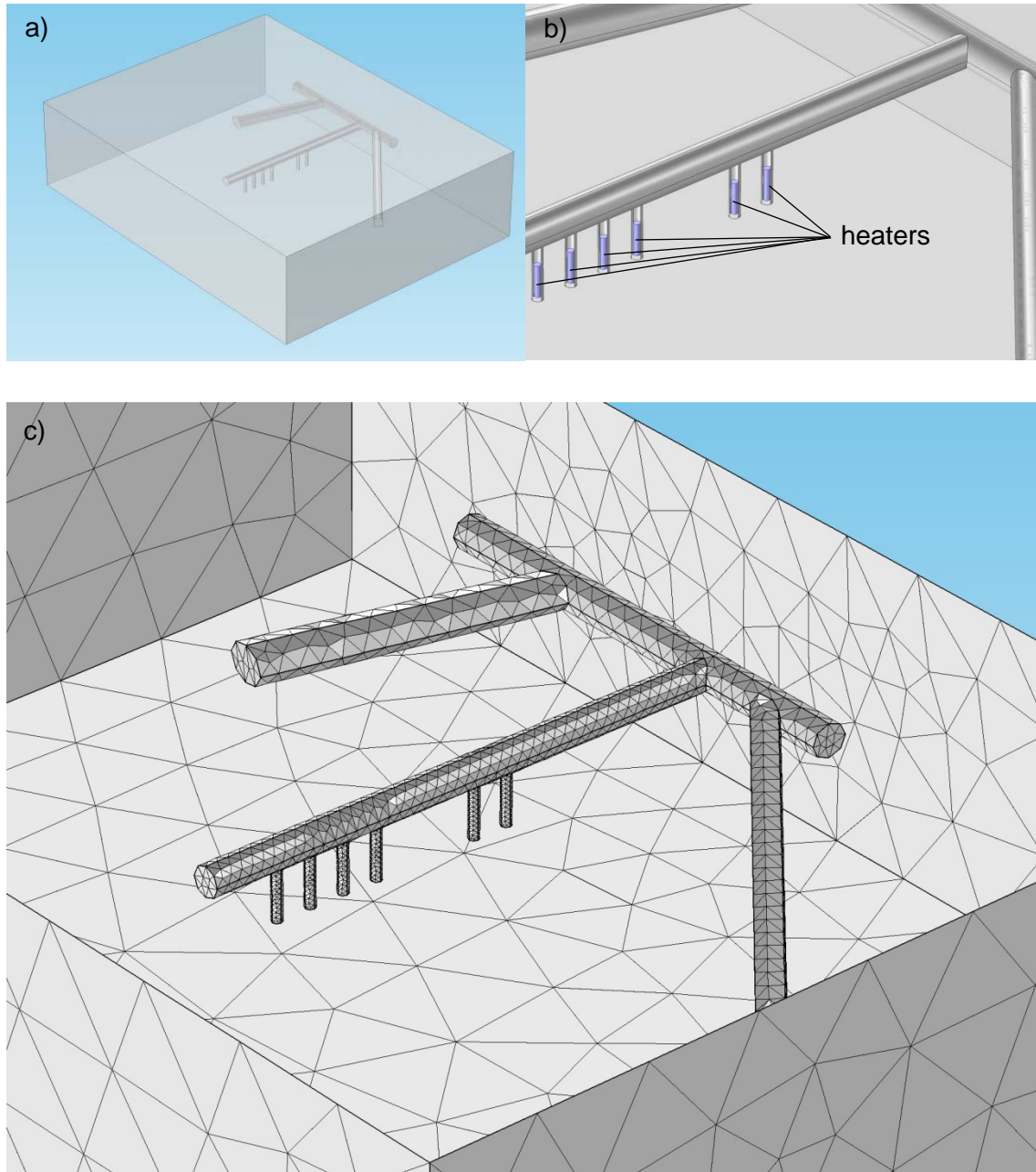


Fig. 5.1 Domain of the thermal model;
a) total view, b) close-up of the PR-tunnel, c) grid

Tab. 5.1 Heat capacities at 25 °C; after /PAT 97/

Rock type	Mean value [J/(kg °C)]
Greenstone	775
Dioritoids	770
Quartz monzodiorite-granodiorite	760
Granodiorite-granite	755
Granite	740
All samples	755

5.2.2 Other materials

Besides for the rock four other subdomains can be differentiated by their different material properties: canisters, buffer, backfill and air. They are depicted in Fig. 5.2. The related material data was taken from /KRI 07/ except for the heaters and for air, the latter of which was of no concern in /KRI 07/. The data for copper provided by the COMSOL material data base¹¹ ($\rho=8700 \text{ kg/m}^3$, $\lambda=400 \text{ W/(m K)}$ and $c=385 \text{ J/(kg K)}$) was assumed to represent the canister material as /KRI 07/ also inserted values for copper from a different source.

The IJ-, G- and S-tunnel were assumed to be air-filled using the material “air” from the COMSOL data base which introduces automatically a temperature dependency of all three quantities. As the heat from the canisters barely reaches these three tunnels the referring values can be taken to be constants, though ($\rho\sim 1.23 \text{ kg/m}^3$, $\lambda=0.024 \text{ W/(m K)}$ and $c\sim 1005 \text{ J/(kg K)}$). All thermal material data used in the heat transport model are compiled in Tab. 5.2.

Tab. 5.2 Material data for the heat transport model

Material	Thermal conductivity [W/(m K)]	Specific heat capacity [J/(kg K)]	Density [kg/m ³]
granite	2.72	770	2770
air	$\lambda(T)$; ~ 0.024	$c_p(T)$; ~ 1005	$\rho(T)$; ~ 1.23
backfill	1.5	780	2500
bentonite	1.0	800	2780
copper	400	385	8700

¹¹ integrated in the code COMSOL

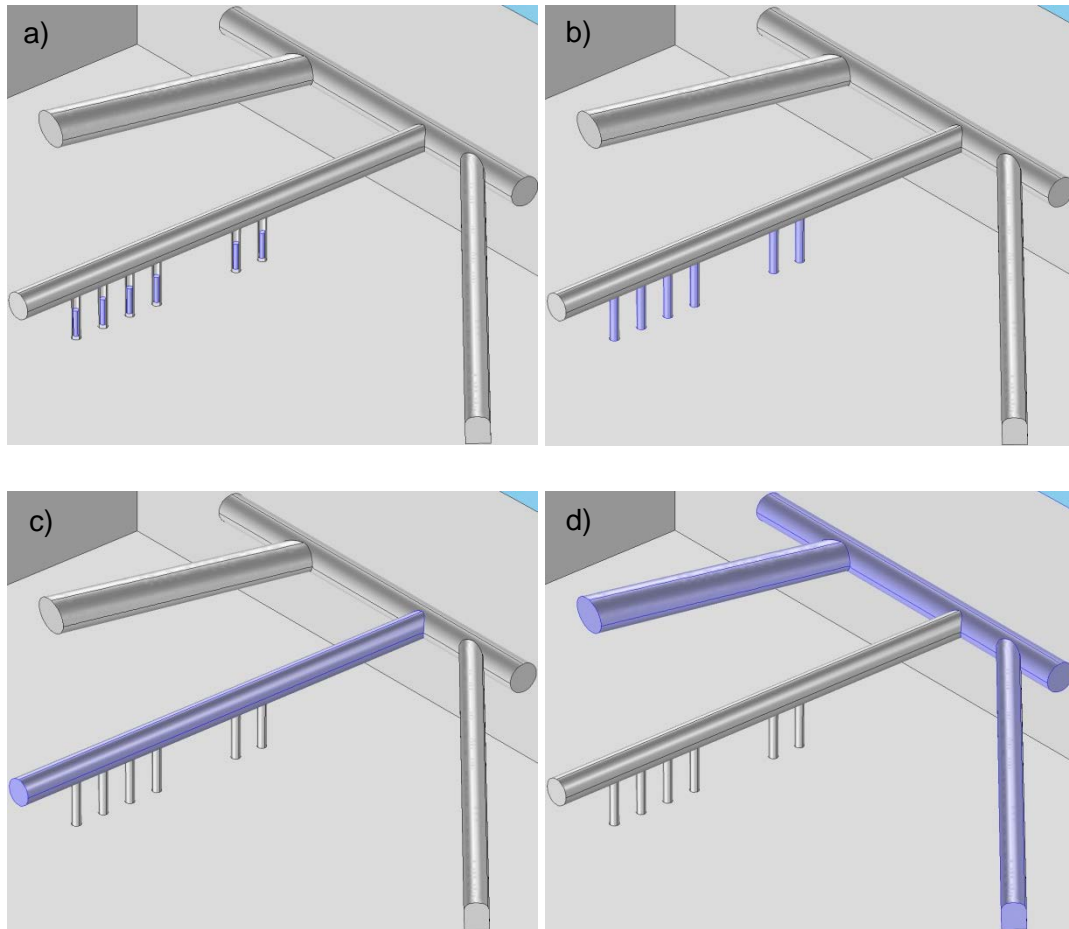


Fig. 5.2 Objects of different properties; a) canisters, b) buffer, c) backfill, d) air

5.3 Thermal initial and boundary conditions

In the thermal model the rock takes up heat from the six heaters in the deposition boreholes. Heat inflow is defined in the model by the power uptake of the respective heater where the power is equally distributed over its volume. A free outflow condition is assigned to the boundaries of the model domain.

In the following the heaters are labelled with the same number as the borehole where they have been emplaced. Each heater has its own history of power consumption as there were some failures, power reductions and also different starting times. The graphical log of power uptake is given in Fig. 5.3. Note that day 0 in the graphs of Fig. 5.3 refers to different dates. To simplify the input for the model the data were approximated by step functions. The simplified functions are depicted in Fig. 5.4 in their actual sequence.

The background temperature at the Prototype Repository amounted to 15 °C /KRI 07/.

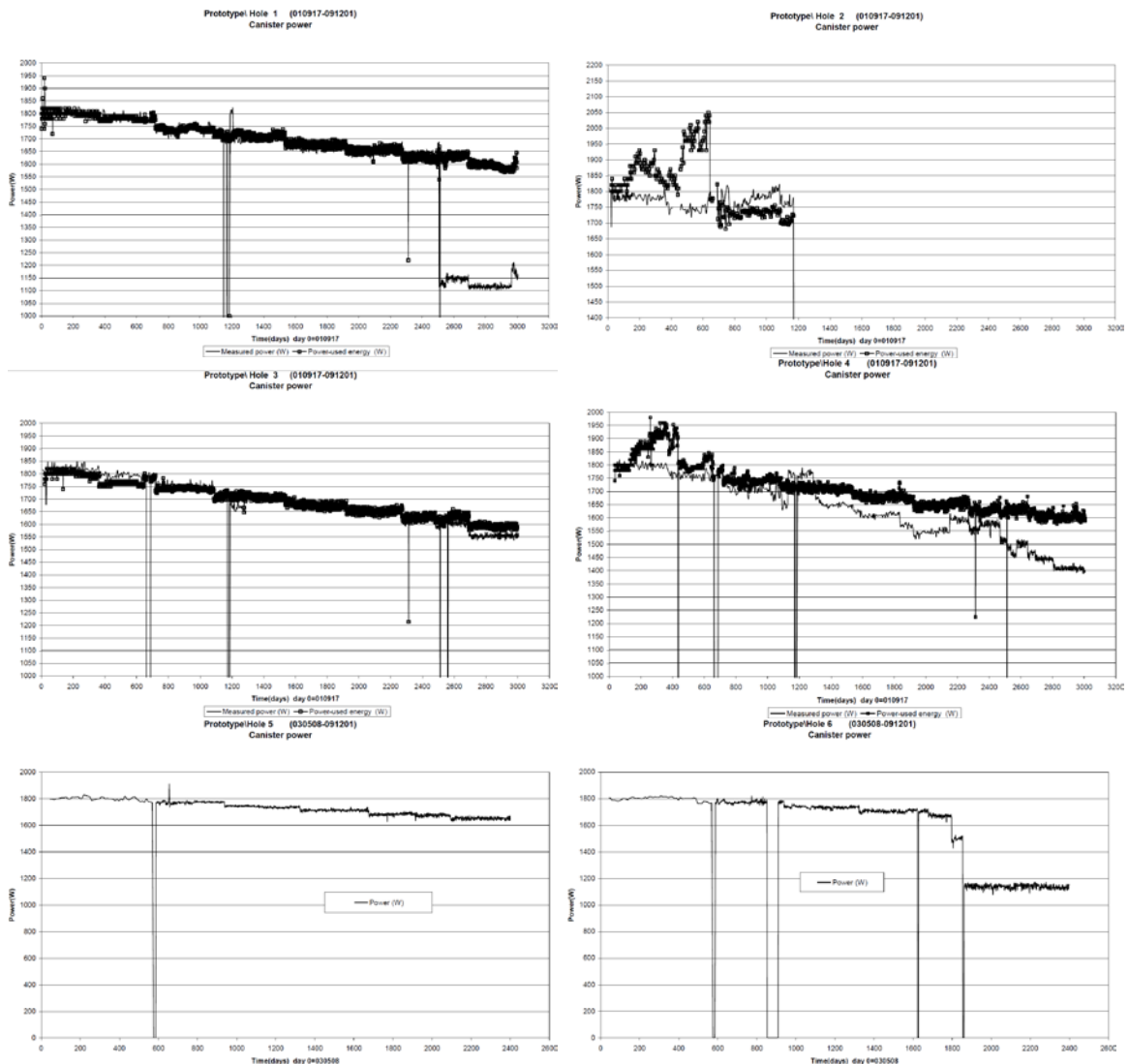


Fig. 5.3 Heater power consumption in deposition holes 1 to 6; from /KRI 10/

5.4 Calibration targets

The heat flow model was intended to be calibrated against continuous sensor data from the rock around deposition boreholes 5 and 6 as well as from the backfill in the tunnel above these boreholes. The data are depicted along with the model results in Fig. 7.12 and Fig. 7.13. As it turned out, though, the achieved fit was good enough for the purpose at hand without any calibration (see section 7.2.1).

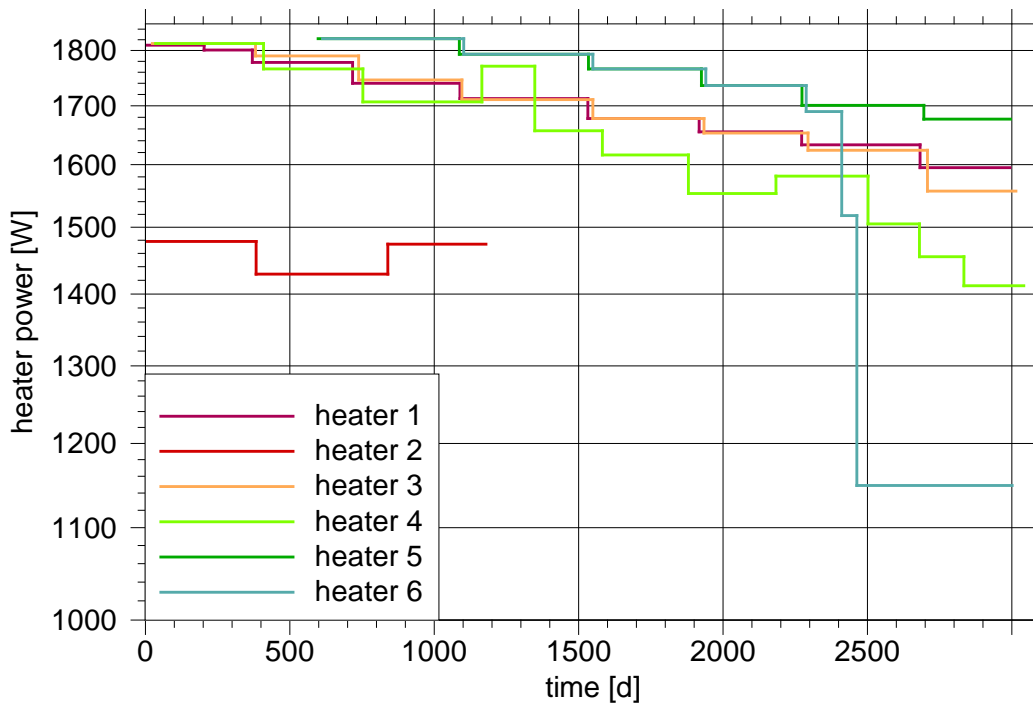


Fig. 5.4 Heater power consumption simplified for modelling

6 Thermo-hydraulic flow model

6.1 Model domain

(same as for the isothermal flow model, see section 4.1)

6.2 Material properties

Thermo-hydraulically coupled models require not only the hydraulic material properties described in section 4.2 and the thermal material properties given in section 5.2 but also temperature-dependent properties of the water, namely density and viscosity. Density was calculated after /OLD 98/ and viscosity after an ad hoc approach presented in /KRÖ 10/. A porosity of 0.005 was assumed for the matrix as well as for the fractures.

6.3 Initial and boundary conditions

6.3.1 Groundwater flow

A certain conceptual inconsistency between the fluid flow model and the heat flow model becomes apparent when it comes to the hydraulic boundary conditions. While the fluid flow model represents the pre-installation phase the heat flow model stands for the operational phase. The difference lies in the deposition boreholes which are not filled during the pre-installation phase but contain heaters and buffer during the operational phase.

The effect of the bentonite buffer on the flow field in the host rock is, that in the beginning more water is drawn by the clay than the rock can provide which is more or less equivalent with an open boundary. Later, though, the clay impedes further water outflow from the rock quite effectively which can be approximated by a no-flow boundary. The BRIE had shown that significant re-saturation via the distributed outflow from the rock can require considerably more than the testing period of 520 days /FRA 17/. For the orientating investigations intended here the boreholes are therefore assumed to be hydraulically open all the time.

6.3.2 Heat flow

The initial temperature of 15 °C was chosen to be the same as for the heat flow model. The formulation of thermal boundary conditions required the results from the heat flow model that are discussed later in section 7.2 in detail.

The same conceptual inconsistency that was found in the context of the hydraulic boundary conditions (see section 6.3.1) concerns also the selection of temperature data as boundary conditions for the thermo-hydraulic model. Deposition boreholes as well as the PR-tunnel are filled with buffer or backfill material during the operational phase while they are open during the pre-installation phase.

This problem was circumvented by prescribing the calculated transient temperature at the borehole walls in the heat flow model to the geotechnical openings in the thermo-hydraulic model. The required temperature distributions are quite complex as indicated in Fig. 6.1. However, since only an indication of the influence of temperature on the flow field was sought, the mean temperature on the borehole surface was used instead.

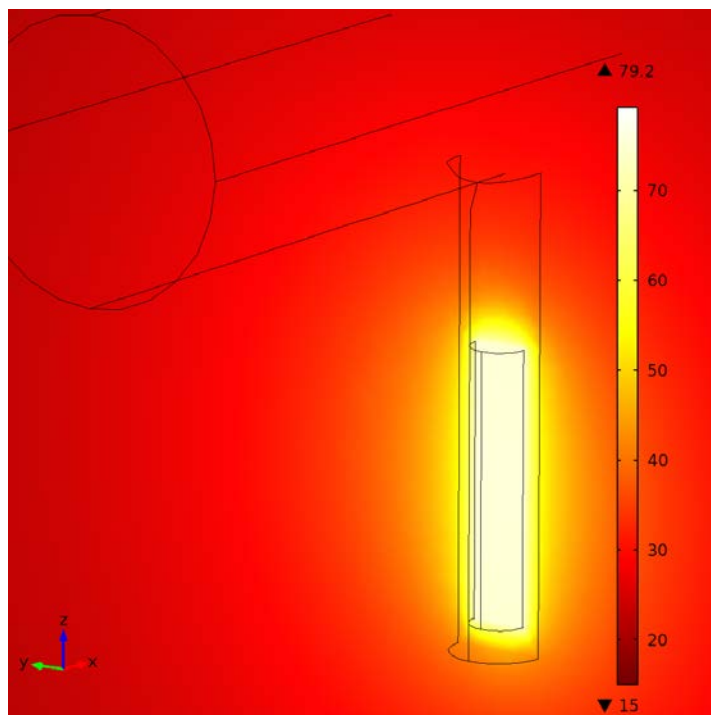


Fig. 6.1 Temperature in a vertical cross-section through heater 1 after 3000 days

While there clearly are distinct temperature differences in the vertical direction, the differences along the perimeter appear to be rather little. Fig. 6.2 shows the mean temperatures for deposition boreholes 1, 3, and 6 along four vertical line segments that lay either in the direction of the tunnel (east and west) or orthogonal to the tunnel axis (north and south). Three of these vertical lines at borehole 1 are highlighted in blue in the inlay plot in Fig. 6.2. Also plotted are the mean values for each borehole surface. The maximum temperature difference in the vertical line segments of each borehole does not exceed 3 °C and is found for the outer boreholes in the direction of the tunnel, as expected. The mean surface value includes the surface at the bottom of the borehole which is not quite as hot as the borehole walls next to the heater (see Fig. 6.1).

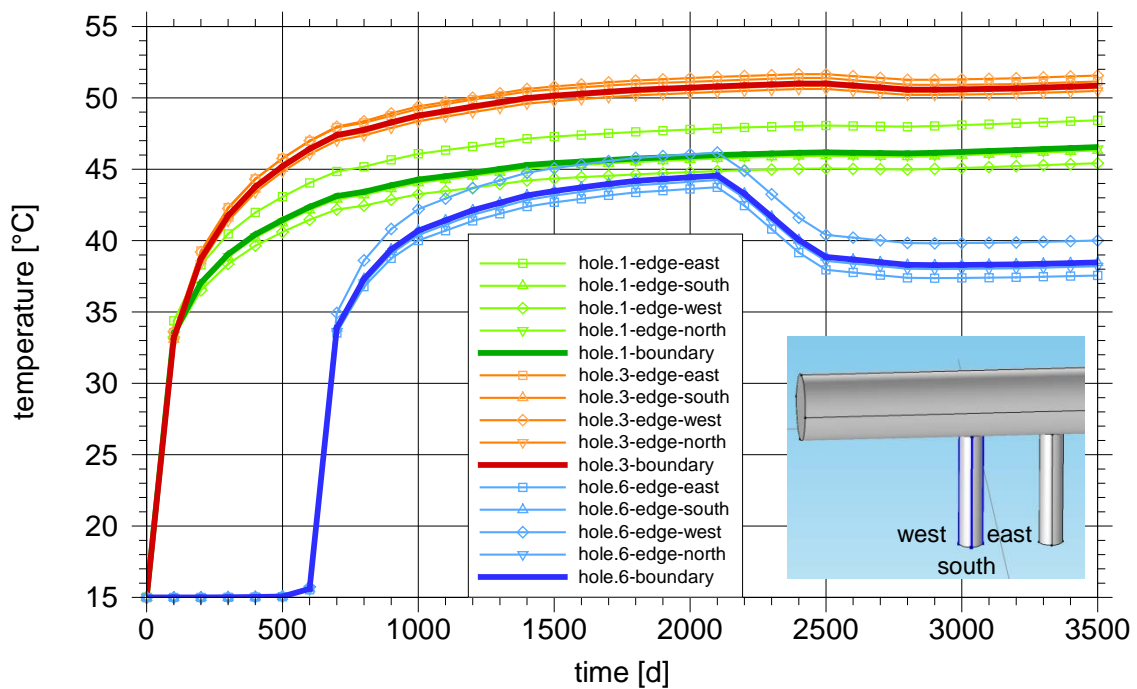


Fig. 6.2 Temperatures in boreholes 1, 3, and 6; mean values along 4 vertical line segments per borehole (thin curves) and mean value on the surface (thick curves)

6.3.3 Sets of boundary conditions

The thermo-hydraulic model was executed as a thermo-haline calculation where the salt concentration was set to zero everywhere at every time. In principle there are therefore three sets of boundary conditions as depicted in Fig. 6.3:

- outer model boundary:
 - prescribed pressure
 - rock temperature ($T = 15\text{ °C}$)
 - no salt

- tunnel surface:
 - atmospheric pressure
 - temperature outflow
 - salt outflow

- borehole surface:
 - atmospheric pressure
 - temperature evolving according to the heat flow model
 - salt outflow

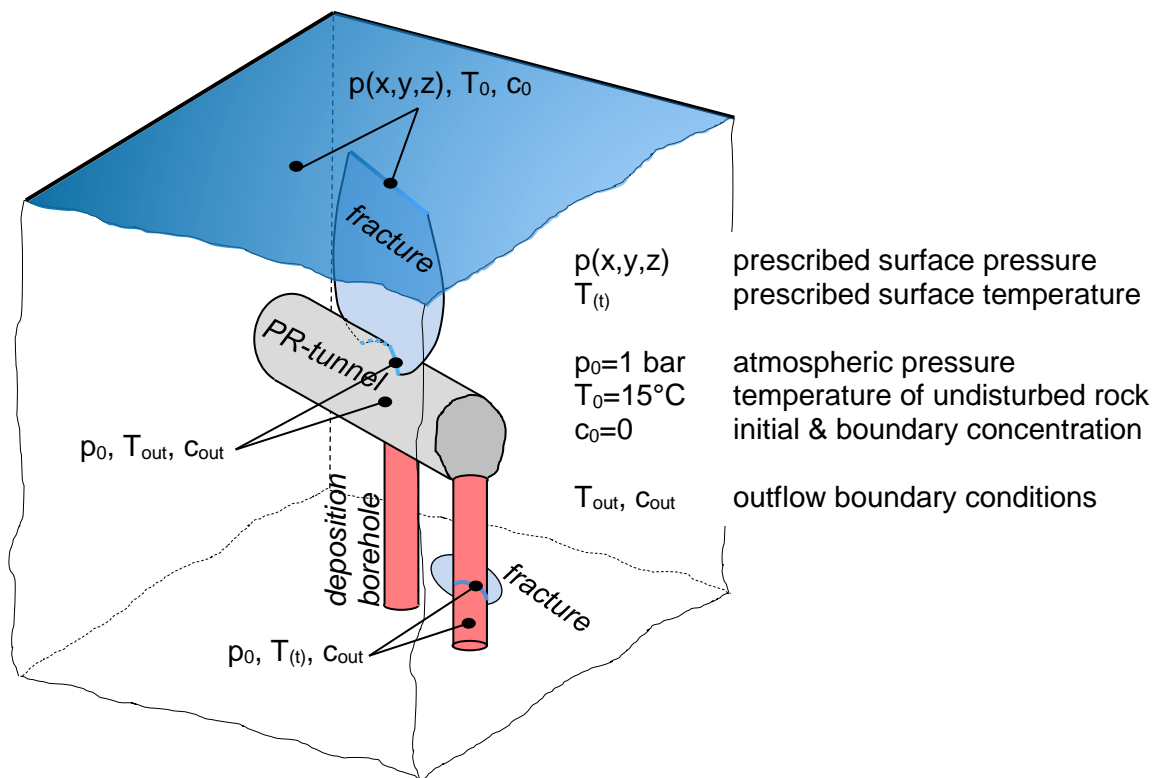


Fig. 6.3 Boundary conditions for the thermo-hydraulic model

6.4 Calibration targets

The thermo-hydraulic model discussed in this section is intended to provide only orientating information. Calibration was therefore not performed.

7 Results

7.1 Pre-installation flow

7.1.1 Calibration

Calibration was basically performed on the basis of three outflow measurement campaigns along the PR-tunnel as well as on measured outflow into the deposition boreholes. It required a series of four increasingly improved models. Data and approaches from the BRIE-model /KRÖ 17b/ were applied to the first model (**model 1**) where appropriate. This led immediately to a good agreement of model results with the outflow data for the six deposition holes but underestimated flow into the PR-tunnel. The results of this first as well as of all the following calibration steps are compiled in Fig. 7.1.

An increase of the matrix permeability by a factor of 5 (**model 2**) improved the fit for the outflow into the tunnel considerably. One exception, though, was found at the tunnel section that was presumably influenced by the assumed fracture. Here, the calculated outflow was not nearly reflecting the measured high outflow rate.

Since the choice of the permeability for the assumed fracture offered naturally a certain degree of freedom, the permeability was also increased by a factor of 5 (**model 3**). This led to a satisfying if a bit low profile for the outflow along the tunnel. No significant changes occurred in the outflow rates for the deposition boreholes from model 2 to model 3.

However, outflow into the boreholes was now overestimated. As a final measure the permeability of the borehole skins was divided by a factor of 5 (**model 4**) which resulted in a reasonably good match of calculation and measurement for the tunnel as well as for the boreholes.

It has to be mentioned here that there were also outflow data for the G-, the I+- and the J+-tunnel (see section 3.4.3). The outflow rates for these tunnels calculated with model 4 lay up to two orders of magnitude below the measured values. However, the calculated rates represent only outflow over the matrix because there had been no means to incor-

porate fractures appropriately. Flow from such fractures could have contributed considerably to the total outflow rate.

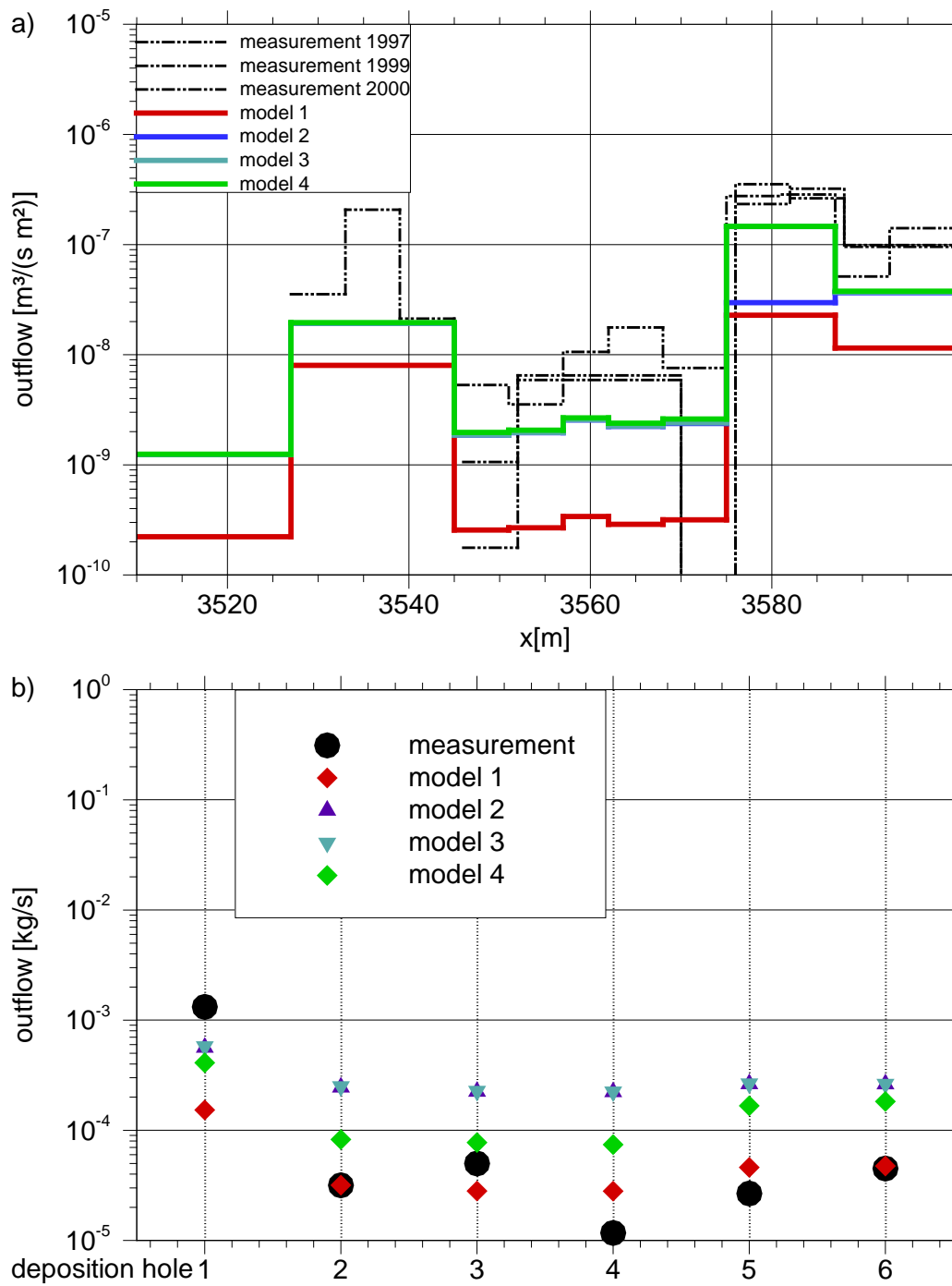


Fig. 7.1 Outflow measurements and model results; a) flux density along the PR-tunnel, b) total outflow into the six deposition boreholes

Matching the calculated outflow from the rock to the measured outflow distribution along the PR-tunnel and the outflow into the six “deposition boreholes” required only a moderate modification of the initially used permeabilities. The approach for modelling flow at the BRIE-site can thus be considered to be successfully transferred to the Prototype Repository as all geometrical and flow data are acknowledged.

7.1.2 Outflow rates

The calculated outflow rates for the steady-state isothermal flow model are compiled in Tab. 7.1. Of particular interest is the relation between the distributed outflow over the 2d-surfaces of the geotechnical openings and the local outflow from the fractures. This relation concerns the PR-tunnel as a whole as well as specifically those tunnel segments that are intersected by the large fractures (see Fig. 7.2). In the same sense this applies also to deposition boreholes 1 (see Fig. 7.3), 5 and 6 (see Fig. 7.4) as these are intersected by minor discrete fractures. Since deposition borehole 6 is divided into several sections like the PR-tunnel, the relation of different minor fractures to the single sections is also considered. In Tab. 7.2 are thus compared

- distributed outflow,
- local outflow from fractures,
- total outflow, and
- percentage of the contribution of local outflow from fractures flow to total outflow.

According to the data in Tab. 7.2 outflow into tunnel or borehole sections containing a deterministic fracture is mostly dominated by the flow from the fractures. This holds still also true if the whole tunnel or whole deposition holes are considered. In all cases except from section dep.h.6-ou in borehole 6 (see Fig. 7.4) between two thirds and almost all the outflow is accounted for by flow from fractures. Only the contribution of minor fracture 5 to section dep.h.6-ou is very low. This, however, is probably a consequence of the permeability of minor fracture 5 which is quite low in comparison to all other discrete fractures (see Tab. 4.2). Taking into account that the transmissivity and thus also the permeability of a fracture at Äspö is roughly a function of fracture size /VID 17/ corroborates furthermore the assumption that undetected, even smaller fractures can be lumped together as an equivalent porous medium.

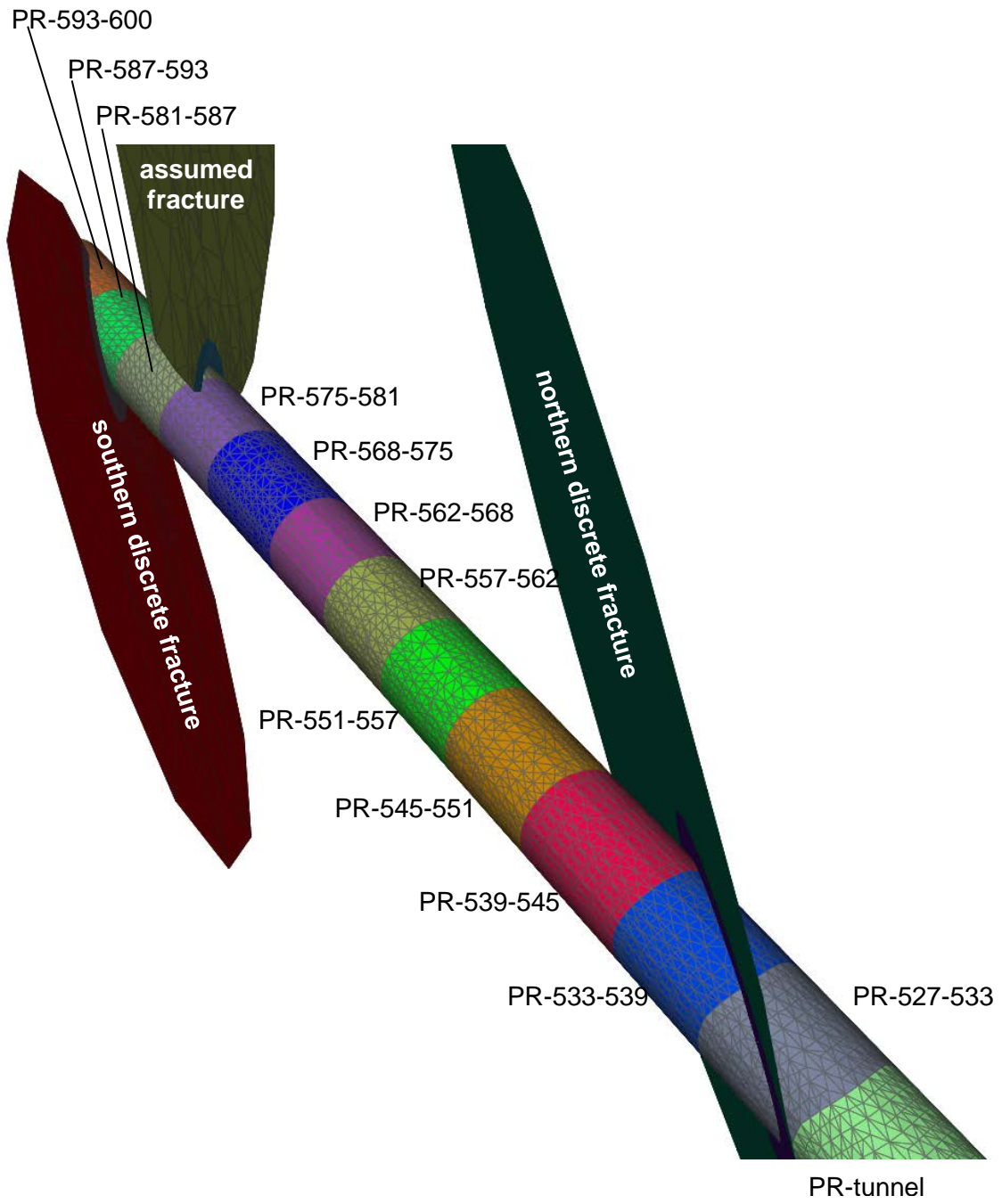


Fig. 7.2 PR-tunnel as well as intersecting large fractures

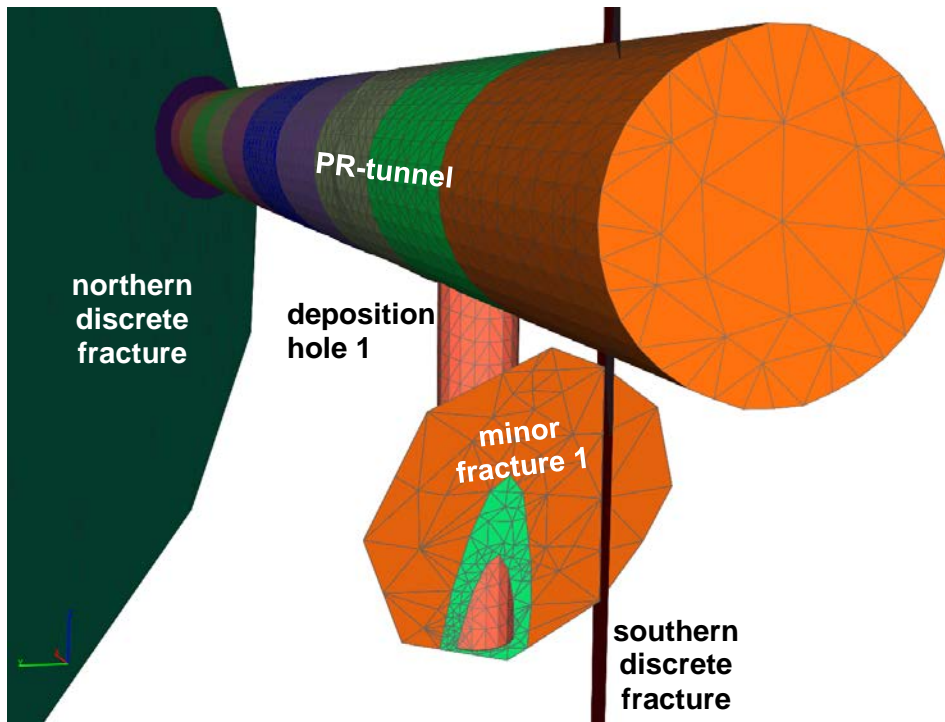


Fig. 7.3 Deposition borehole 1 as well as intersecting minor fracture 1

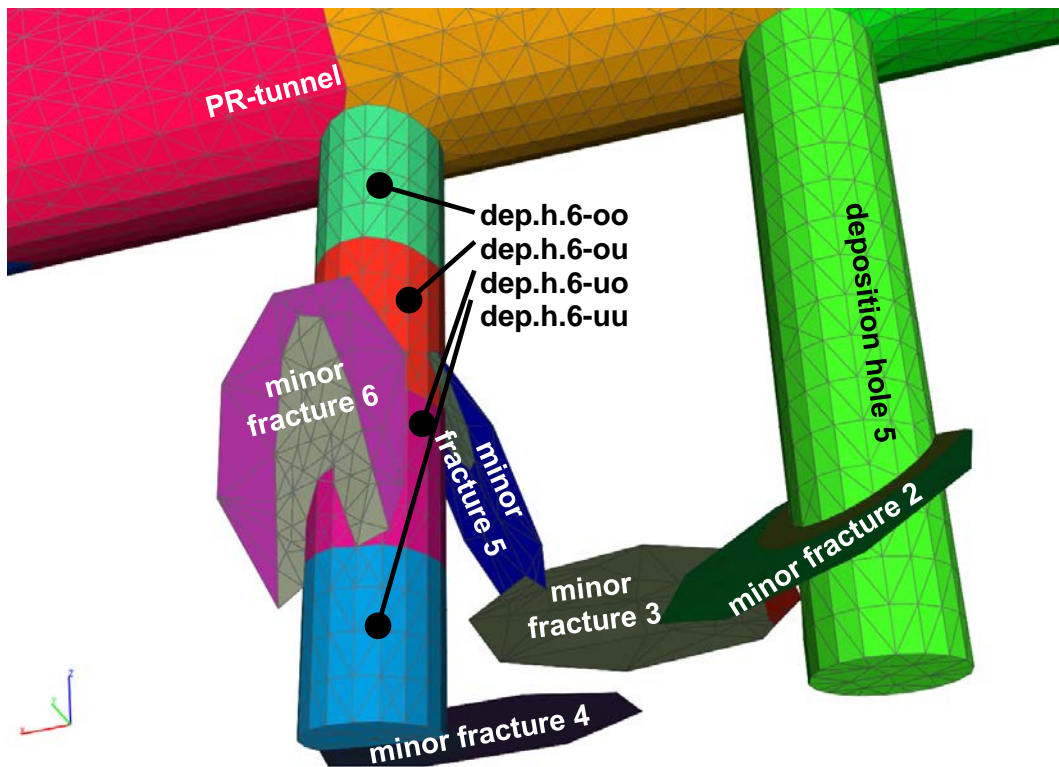


Fig. 7.4 Deposition boreholes 5 and 6 as well as intersecting fractures

Tab. 7.1 Outflow rates for the steady-state isothermal flow model

Distributed outflow over 2d-surfaces		Outflow from fractures	
Subset name	Outflow rate [kg/s]	Subset name	Outflow rate [kg/s]
PR-tunnel		Large fractures	
PR-527-533	$1.40 \cdot 10^{-04}$	Northern fracture	$6.55 \cdot 10^{-03}$
PR-533-539	$1.67 \cdot 10^{-04}$	Southern fracture	$9.31 \cdot 10^{-03}$
PR-539-545	$2.37 \cdot 10^{-04}$	Assumed fracture	$3.97 \cdot 10^{-02}$
PR-545-551	$2.39 \cdot 10^{-04}$	Minor fractures	
PR-551-557	$2.52 \cdot 10^{-04}$		
PR-557-562	$2.74 \cdot 10^{-04}$	1	$4.95 \cdot 10^{-04}$
PR-562-568	$2.99 \cdot 10^{-04}$	2	$1.61 \cdot 10^{-04}$
PR-568-575	$3.88 \cdot 10^{-04}$	-	-
PR-575-581	$3.74 \cdot 10^{-04}$	4	$5.56 \cdot 10^{-05}$
PR-581-587	$4.14 \cdot 10^{-04}$	5	$5.04 \cdot 10^{-07}$
PR-587-593	$3.92 \cdot 10^{-04}$	6	$1.41 \cdot 10^{-04}$
PR-593-600	$7.74 \cdot 10^{-04}$	Total outflow (distributed plus fractures)	
PR-tunnel-rest	$4.27 \cdot 10^{-04}$		
PR-tunnel (sum)	$4.38 \cdot 10^{-03}$	PR-tunnel	$5.99 \cdot 10^{-02}$
Deposition boreholes		Deposition hole 1	$6.12 \cdot 10^{-04}$
		Deposition hole 5	$2.36 \cdot 10^{-04}$
Deposition hole 1	$1.17 \cdot 10^{-04}$	Deposition hole 6	$2.61 \cdot 10^{-04}$
Deposition hole 2	$1.19 \cdot 10^{-04}$		
Deposition hole 3	$1.09 \cdot 10^{-04}$		
Dep.h.4-bottom	$7.55 \cdot 10^{-06}$		
Dep.h.4-east	$2.52 \cdot 10^{-05}$		
Dep.h.4-north	$2.72 \cdot 10^{-05}$		
Dep.h.4-west	$2.04 \cdot 10^{-05}$		
Dep.h.4-south	$2.28 \cdot 10^{-05}$		
Dep.h.4 (sum)	$1.03 \cdot 10^{-04}$		
Deposition hole 5	$7.46 \cdot 10^{-05}$		
Dep.h.6-oo	$2.05 \cdot 10^{-05}$		
Dep.h.6-ou	$1.25 \cdot 10^{-05}$		
Dep.h.6-uo	$1.35 \cdot 10^{-05}$		
Dep.h.6-uu	$1.69 \cdot 10^{-05}$		
Dep.h.6 (sum)	$6.34 \cdot 10^{-05}$		
Other tunnels			
G-tunnel	$4.15 \cdot 10^{-03}$		
I+-tunnel	$1.31 \cdot 10^{-04}$		
J+-tunnel	$5.03 \cdot 10^{-04}$		

Tab. 7.2 Comparison of particular outflow rates

Location	Distributed outflow \dot{m}_d [kg/s]	Location	local outflow \dot{m}_f [kg/s]	Total outflow \dot{m}_t [kg/s]	Ratio $\frac{\dot{m}_f}{\dot{m}_t}$ [%]
PR-527-533 PR-533-539 PR-539-545	$5.45 \cdot 10^{-04}$	Northern discrete fracture	$6.55 \cdot 10^{-03}$	$7.10 \cdot 10^{-03}$	92
PR-587-593 PR-593-600	$1.17 \cdot 10^{-03}$	Southern discrete fracture	$9.31 \cdot 10^{-03}$	$1.05 \cdot 10^{-02}$	89
PR-575-581 PR-581-587	$7.88 \cdot 10^{-04}$	Assumed fracture	$3.97 \cdot 10^{-02}$	$4.05 \cdot 10^{-02}$	98
PR-tunnel	$4.38 \cdot 10^{-03}$	Northern, Southern, assumed fracture	$5.56 \cdot 10^{-02}$	$5.99 \cdot 10^{-02}$	93
dep.h.1	$1.17 \cdot 10^{-04}$	Minor fr. 1	$4.95 \cdot 10^{-04}$	$6.12 \cdot 10^{-04}$	81
dep.h.5	$7.46 \cdot 10^{-05}$	Minor fr. 2	$1.62 \cdot 10^{-04}$	$2.36 \cdot 10^{-04}$	68
dep.h.6-ou	$1.25 \cdot 10^{-05}$	Minor fr. 5	$5.04 \cdot 10^{-07}$	$1.30 \cdot 10^{-05}$	4
dep.h.6-uo	$1.35 \cdot 10^{-05}$	Minor fr. 6	$1,41 \cdot 10^{-04}$	$1.55 \cdot 10^{-04}$	91
dep.h.6-uu	$1.69 \cdot 10^{-05}$	Minor fr. 4	$5.56 \cdot 10^{-05}$	$7.25 \cdot 10^{-05}$	77
dep.h.6	$6.34 \cdot 10^{-05}$	Minor fr.s 4 to 6	$1.97 \cdot 10^{-04}$	$2.61 \cdot 10^{-04}$	76

7.1.3 Pressure

The pressure plot in Fig. 7.5 shows the zones of higher pressure being shifted towards the tunnels and boreholes because of the skin. Also the footprint of the three large deterministic fractures is clearly visible. As expected, the pressure gradients point generally from the model boundary towards the geotechnical openings.

7.1.4 Flow

The resulting velocity field is rather complex. Shown in Fig. 7.6 is a horizontal cross-section through the PR depicting only the scalar field of the absolute velocity. A closer look into this plot reveals two phenomena that are specific for fracture flow. The first one can be observed at the rim of the fractures. Very high velocities are found here because the catchment volume at the rim of the fracture is much larger than at its face. This is illustrated by a close-up exemplarily done for the northern discrete fracture in

Fig. 7.7. A theoretical investigation of distortions in an unidirectional flow field caused by differently orientated fractures has been reported by /MAT 04/ where the authors come to the same conclusions. Much in the same way also tunnel ends attract more water than the lateral tunnel surfaces (see also Fig. 7.7).

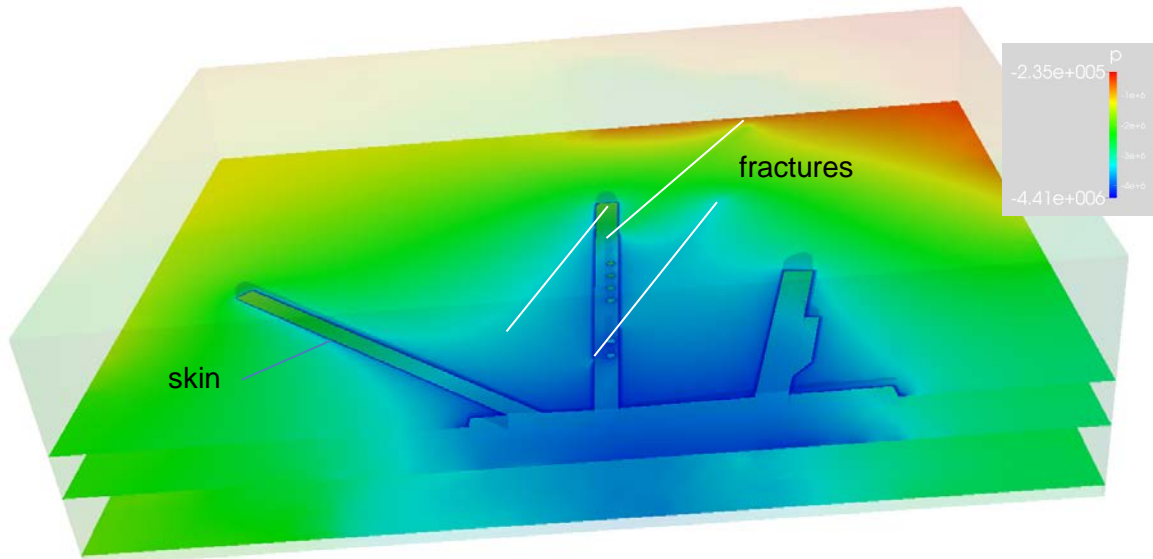


Fig. 7.5 Horizontal cross-sections through the spatial pressure field

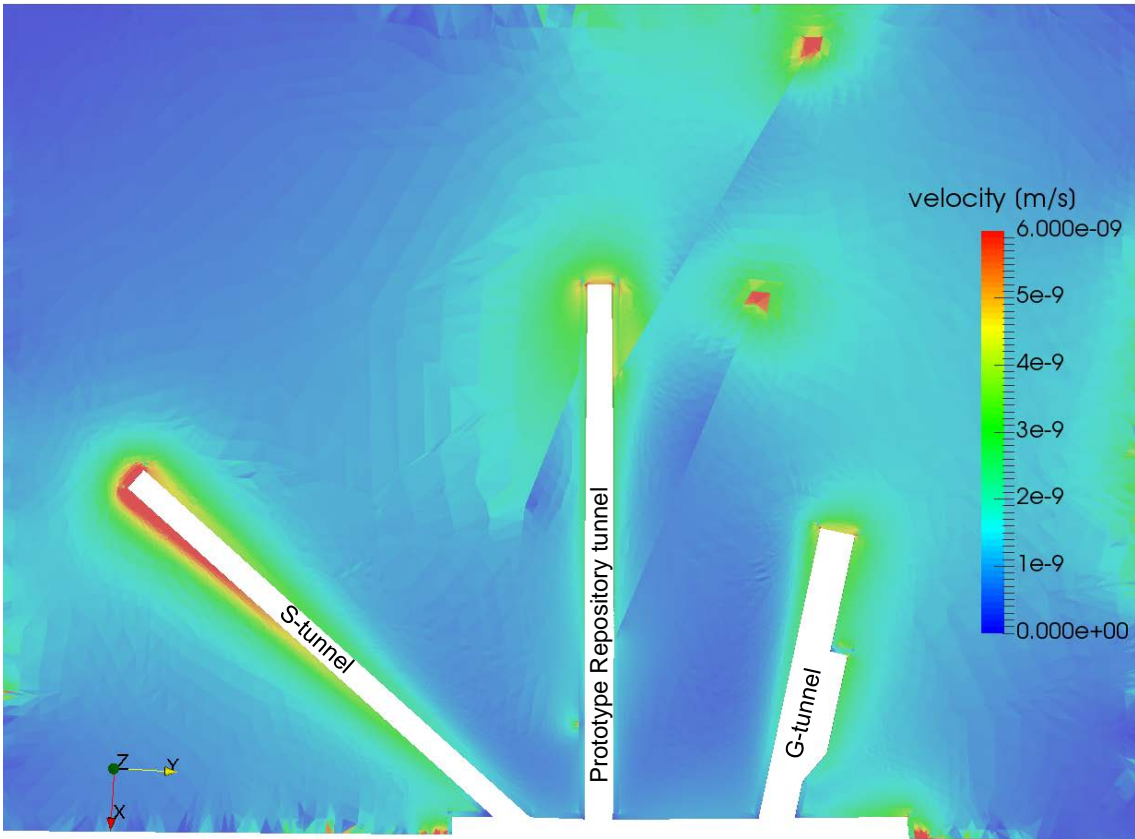


Fig. 7.6 Absolute velocity in a horizontal cross-section

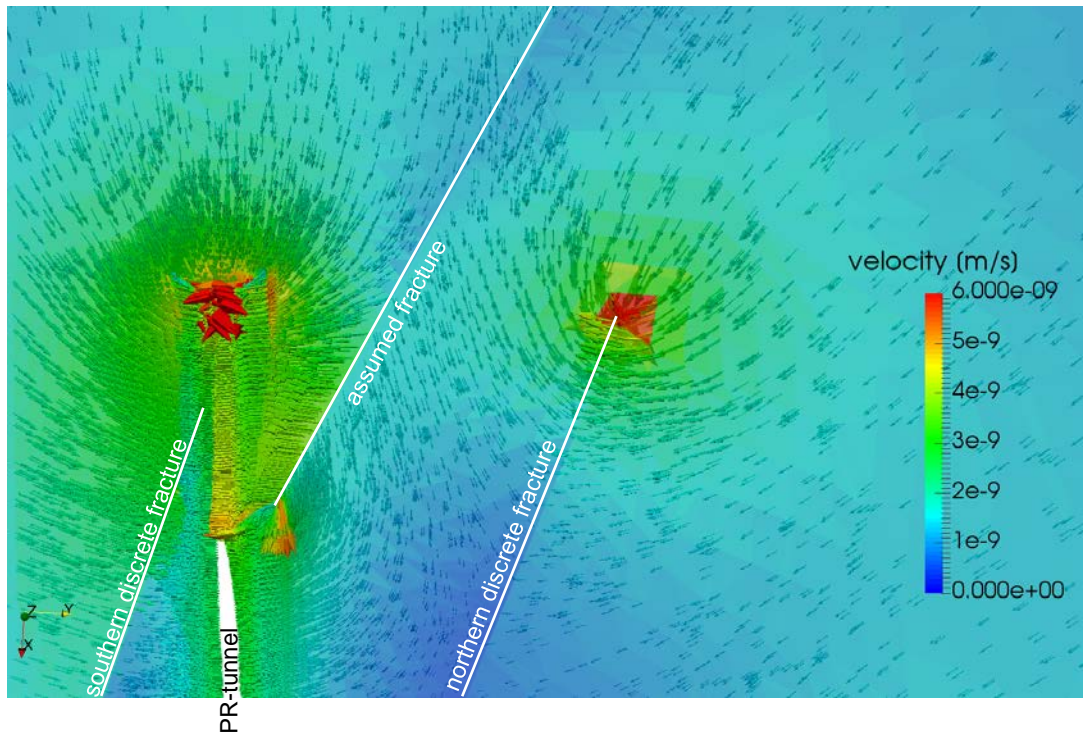


Fig. 7.7 Velocity at the end of the PR-tunnel and at the northern discrete fracture

The second phenomenon concerns the sharp velocity contrasts across the fractures. In Fig. 7.6 the position of the fractures can clearly be identified by this phenomenon. These contrasts form where water reaching a fracture from the matrix is diverted along the fracture because of the comparatively high fracture permeability.

Depending on the overall flow conditions and the permeability distribution, several local flow conditions can prevail at a fracture: water can (a) be drawn from both sides of the fracture, (b) be drawn from one side but also released at the other side, and (c) be released at both sides. Additionally, in case (b) there can be either more water drawn than released (b1) or the reverse (b2). In case (b1) the result is a “hydraulic shading” of the region beyond the fracture.

All variations occur in the flow field around the assumed fracture as shown in Fig. 7.8. Looking along the assumed fracture in Fig. 7.8 from top to bottom, case (a) can be identified first. However, significantly more water is drawn from the left than from the right hand side. Following the fracture trace downwards, the inflow from the right hand side decreases until inflow becomes outflow and case (b1) applies. Even further down outflow to the right eventually exceeds the inflow from the left hand side (case b2). Eventually, at

the bottom of the plot even case (c) can be found where water is apparently strongly attracted to the northern discrete fracture as well as to the PR-tunnel.

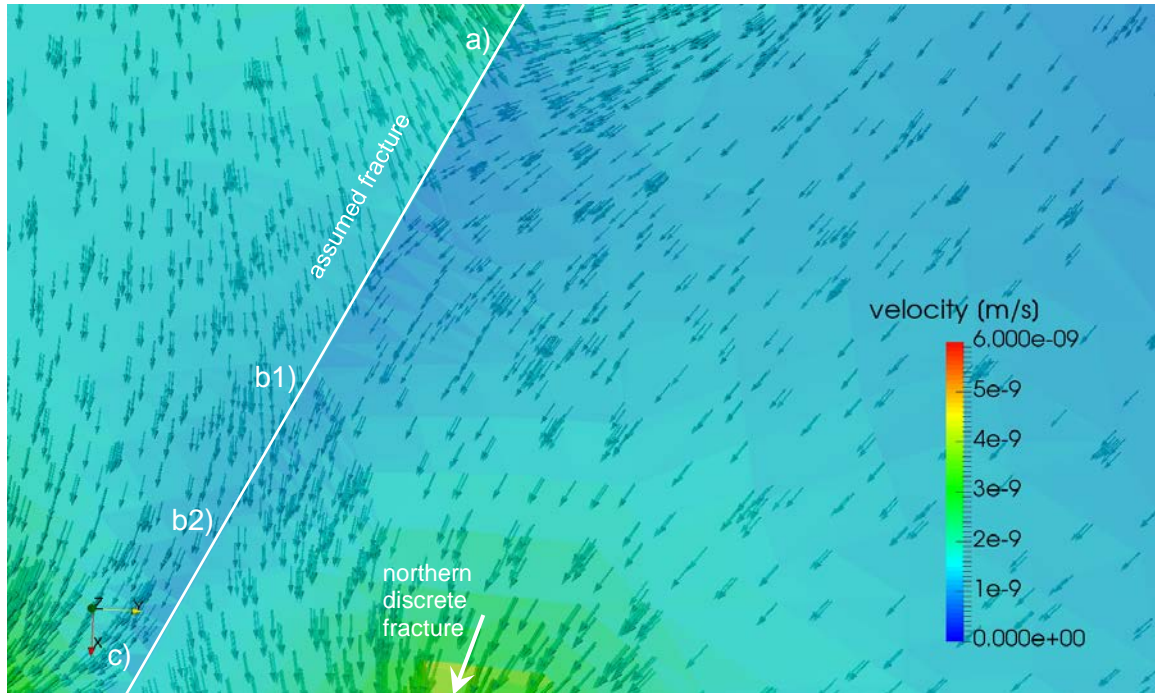


Fig. 7.8 Flow across the northern deterministic fracture (square II in Fig. 7.14)

Another interesting flow phenomenon can be observed at the top of the boreholes as exemplarily shown for borehole 1 in Fig. 7.9. The flow pattern is here clearly influenced by the skin zones around borehole and tunnel. These skin zones are depicted in Fig. 7.10 where the top of the tunnel skin as well as one side of the skin of deposition borehole 1 is cut open. Fig. 7.10 shows that the tunnel skin had been assumed to be thicker than the borehole skin and that it is not considered to be interrupted by the borehole skin. However, the same permeability had been assigned to both skin types anyway (see Tab. 4.2).

What plays a role here, though, are the different diameters of tunnel and borehole as well as the different thicknesses of the skin. Outside the skin zones water is preferentially drawn towards the tunnel instead of the borehole because of its much larger diameter. The less converging streamlines result in a more favourable pressure distribution for the flow. Close to the skin, though, at the contact of tunnel and borehole skin, less resistance to flow is established by the borehole skin because of the lower thickness. Water is therefore locally diverted towards the borehole leading to a significantly increased

flow velocity. As a consequence, flow into the borehole within the tunnel skin is by contrast quite low. It would be highly interesting whether this phenomenon could be confirmed in situ.

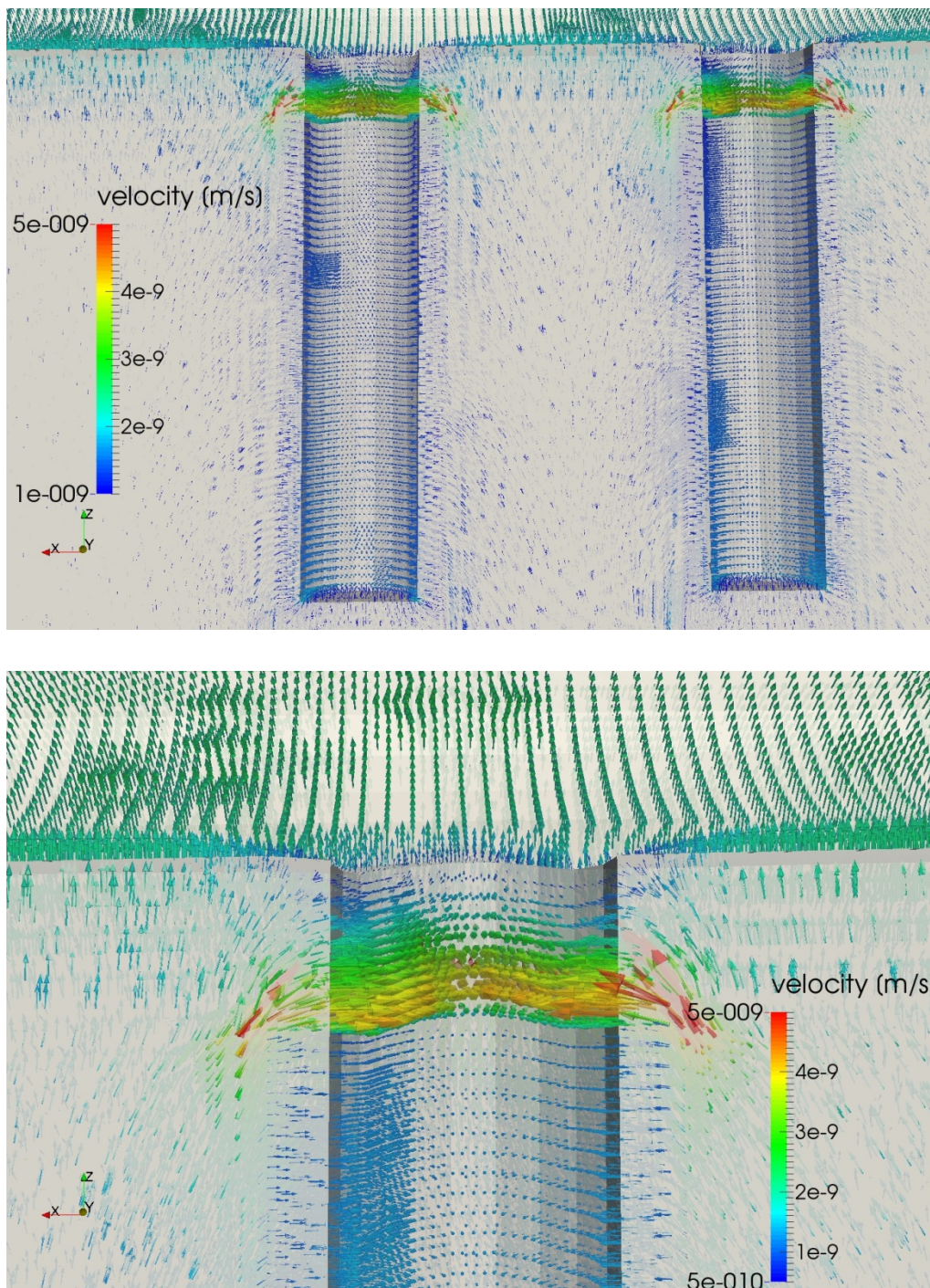


Fig. 7.9 Flow at the top of borehole 1 at different spatial resolutions

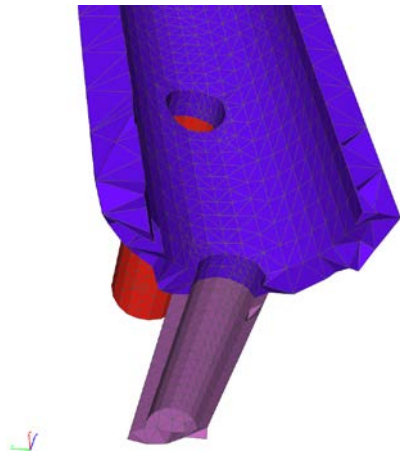


Fig. 7.10 Skin zones of the PR tunnel and borehole 1 sliced open

One more flow effect can be observed in Fig. 7.11. As the PR-tunnel is attracting water from the boundaries the stream lines that are essentially radially converging towards the tunnel. Water is therefore accelerated in the direction of flow which becomes evident in the immediate vicinity of the tunnel. The increased flow velocity can be identified in Fig. 7.11 by the green zone around the tunnel. Note that the above discussed effects of increased flow velocity at the end of the tunnel, at the rim of the southern discrete fracture and close to the top of the boreholes can also be recognised in this figure.

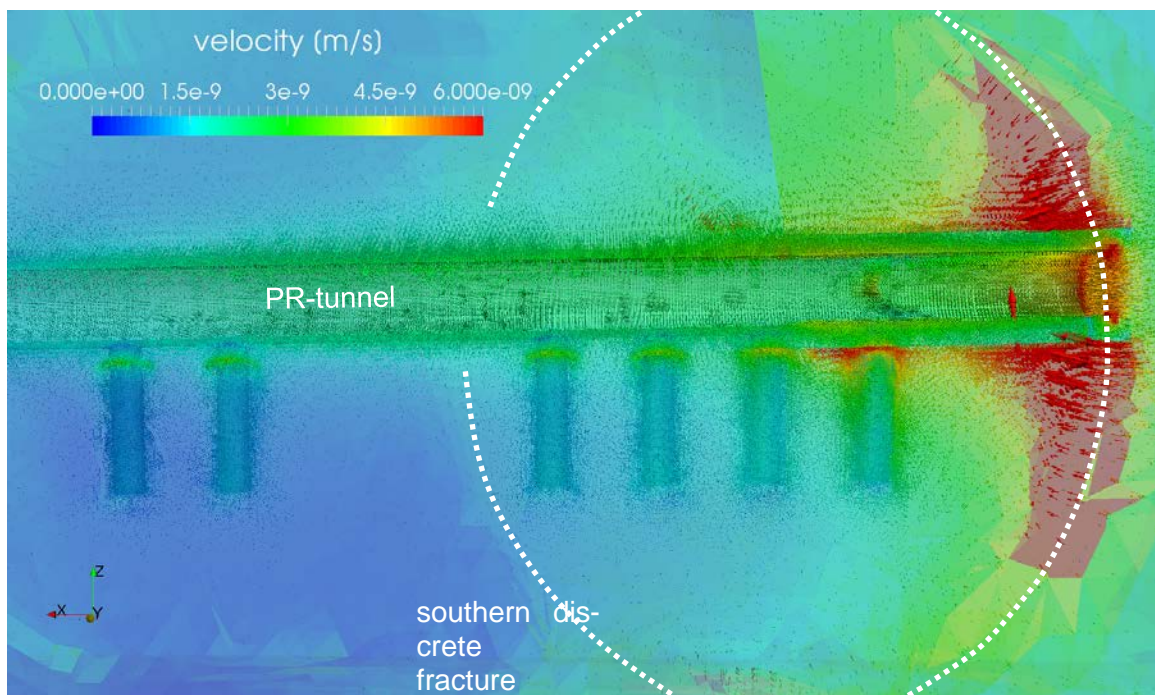


Fig. 7.11 Flow field in a vertical semi-transparent slice of finite thickness

7.2 Heat transport

7.2.1 Calibration

First, the calculated temperature data were checked exemplarily against measurements in the rock and in the tunnel backfill for deposition holes 5 and 6. The position of the temperature sensors as well as the comparison of measured and calculated data are depicted in Fig. 7.12 for deposition hole 5 and in Fig. 7.13 for deposition hole 6. The match between measurements and calculation is already rather satisfying without calibration.

The biggest error of about 2 – 3 °C occurs at the bottom of the tunnel backfill above the deposition hole which is probably caused by a mistake in the model set-up. Compacted bentonite had been assigned to the top metre of the boreholes where the backfill material of the tunnel should have been. The backfill material has a 50 % higher thermal conductivity than the compacted bentonite which explains the comparatively slow temperature increase in the borehole close to the bottom of the tunnel. The resulting errors appear to be local, though, as the fit of measurement and calculation is much better already for the nearest sensor in the lower third of the tunnel cross-section.

All in all the results are already satisfying without further calibration. As an input for the non-isothermal flow model the accuracy of the heat flow model results appears to be sufficient. This conclusion corroborates in turn the validity of the simplifications of the geometry and the heat source data.

7.2.2 Heating dynamics

Fig. 7.12 and Fig. 7.13 show that the most dynamic period of temperature changes are the first 500 days after switching on the respective heater. Later, the changes become negligibly small for all practical purposes after a period of 1000 to 3000 days.

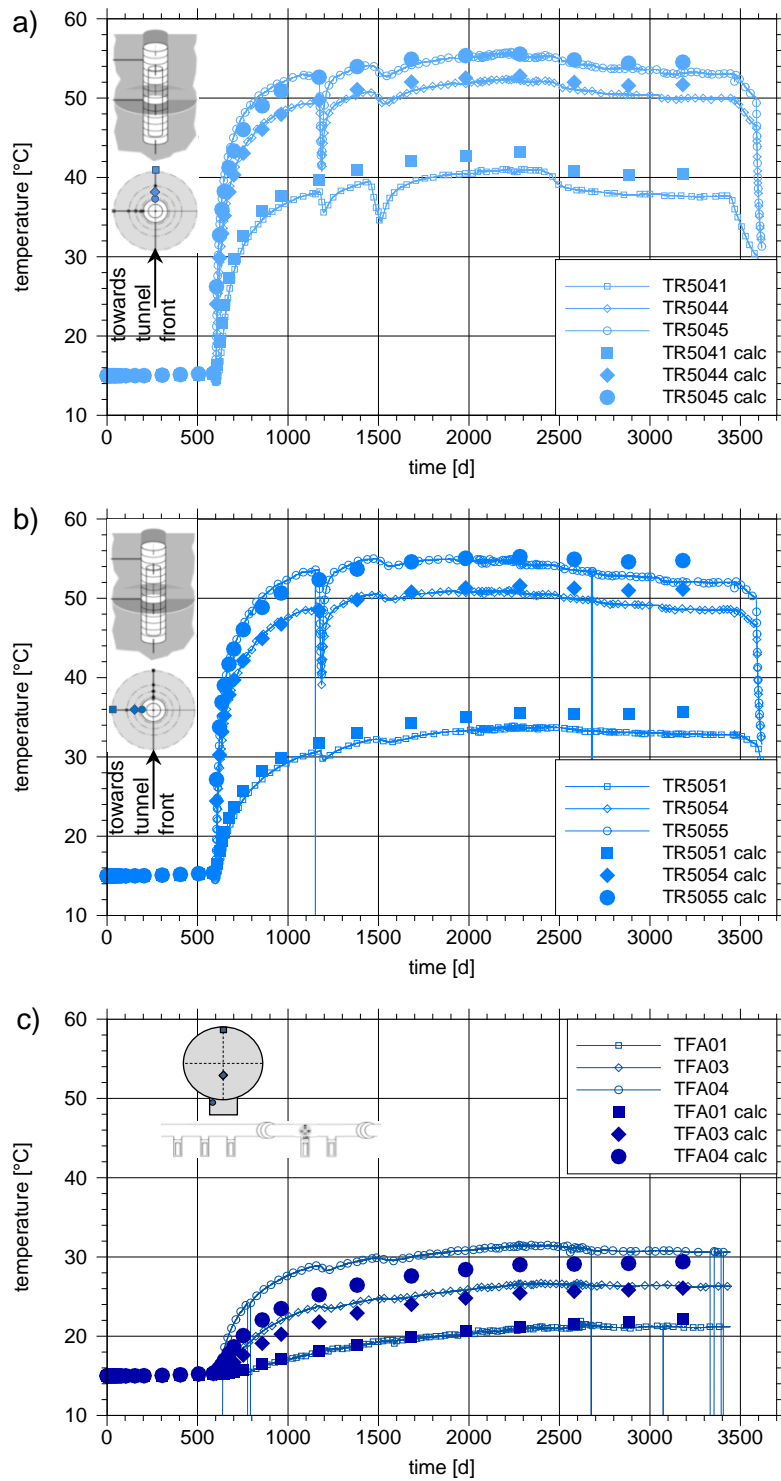


Fig. 7.12 Temperature development at some of the sensors in borehole 5;
a) sensors in the rock in the direction of the tunnel,
b) sensors in the rock orthogonal to the direction of the tunnel,
c) sensors in the backfill

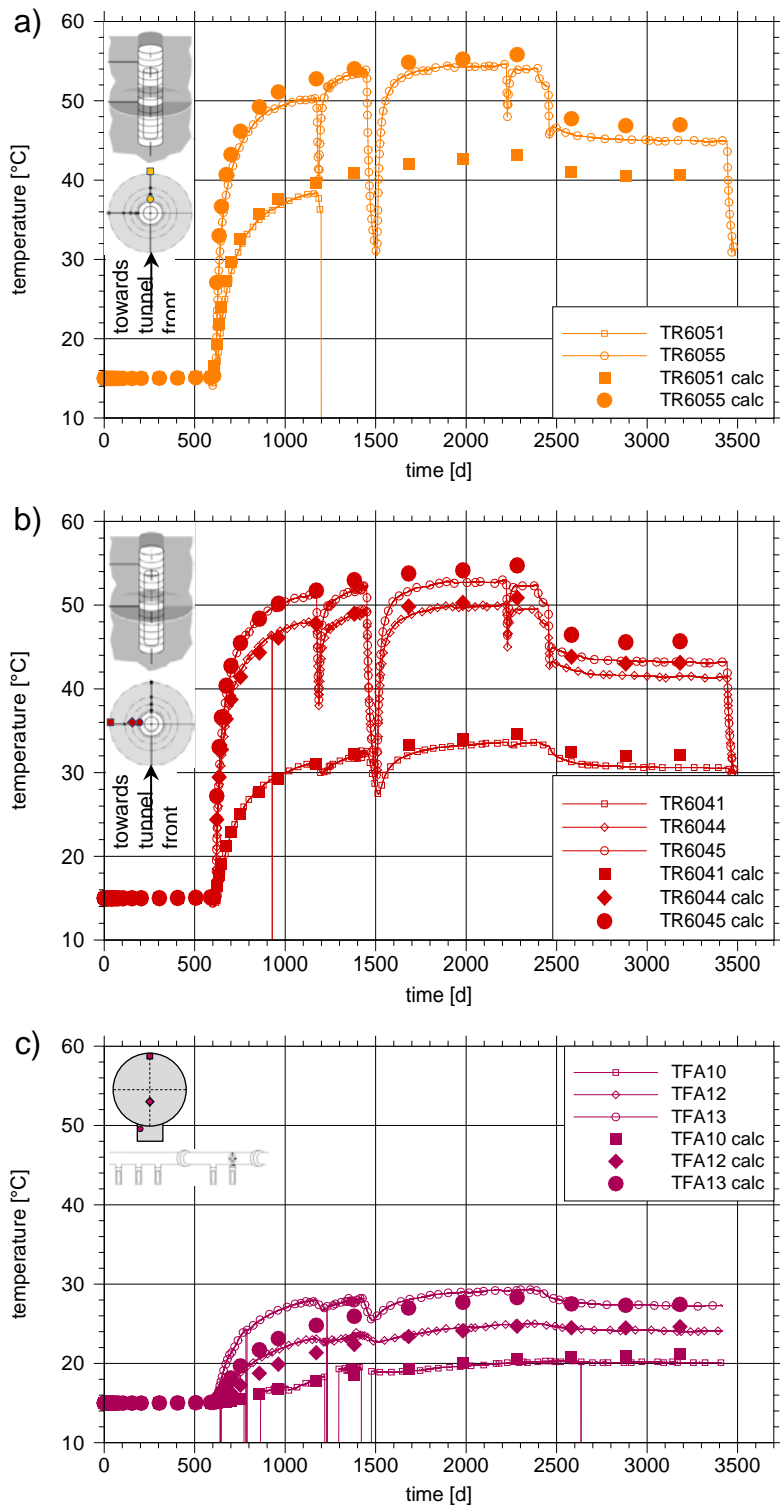


Fig. 7.13 Temperature development at some of the sensors in borehole 6;
 a) sensors in the buffer in the direction of the tunnel,
 b) sensors in the buffer orthogonal to the direction of the tunnel,
 c) sensors in the backfill

One reason for this slowing-down of the temperature increase is of course the slightly decreasing power input into the heaters as shown in Fig. 5.3. Another one, however, is the principle dimensionality of heat transport that changes with time and with the size of the heated volume as depicted in Fig. 7.14. The model results shown here represent isoplanes for an increase of 10 °C above initial temperature for boreholes 5 and 6.

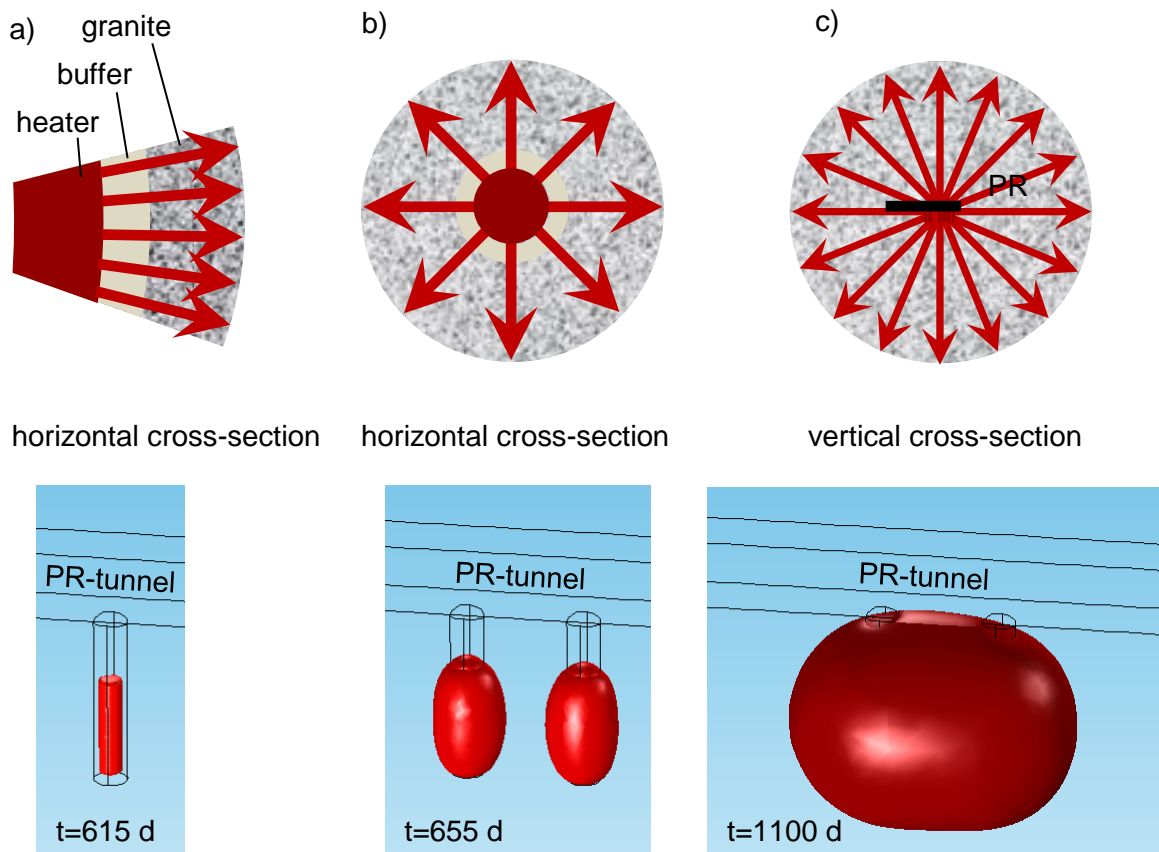


Fig. 7.14 Idealised modes of heat flux over time; sketches and model results for deposition holes 5 and 6

- a) initially: approximately 1d flow
- b) subsequently: radial flow
- c) finally: spherical flow

In the very beginning heat enters the buffer orthogonal to the heater surface which can be approximated by a 1D-transport as shown in Fig. 7.14 a) for a short period of time. Basically, this is the situation of a semi-infinite beam where a constant heat flux is induced at the boundary and where the heat migrates further into that beam by heat conduction. The characteristics of the resulting temperature distributions depend strongly on

the boundary condition i.e. the mechanism by which heat is brought into the beam. In case of Dirichlet boundary conditions the well-known characteristic decay-curves develop with time where the temperature at the inflow boundary is constant and the related gradient converges to zero. But for the problem at hand a flux boundary condition is relevant meaning that the gradient at the boundary is kept constant. The temperature in immediate vicinity of the boundary is increasing with time due to the inflow of heat so that in order to keep the gradient constant the boundary temperature must rise as well. In principle the temperature rises for all times as an analytical solution for this problem shows /CAR 59/. This increase is especially fast in case of 1D-heat transport.

However, in case of the PR heat flow changes quickly to a more or less 2D radial pattern around the canisters as long as the penetration depth of the heat is less than the heater length. This situation is depicted in Fig. 7.14 b). The temperature increase at the heater is significantly less pronounced in this situation because now there is not only a radial but also a tangential spreading of heat resulting in much higher temperature gradients than in 1D at the same flux rate. However, the temperature at the centre of the heater exceeds eventually all limits with time yet.

Finally, on a very large scale, when the spreading heat of neighbouring heaters overlaps to the extent that the complex structure of the six heaters cannot be resolved in the heat affected volume, a somewhat spherical flow evolves as indicated by Fig. 7.14 c). This situation is different from the straight 1D- or the radial 2D-flow because there is a finite steady-state temperature for a constant point source in space /CAR 59/.

A comparison of temperature curves derived from the three analytical solutions mentioned above is given in Fig. 7.15. The input data is the same as for the thermal model of the PR. In all three cases a constant heat flow of 1800 J/s is distributed over the boundary or prescribed as a point source, respectively. Cross-section area of the beam is 1 m², thickness of the plane is 1 m.

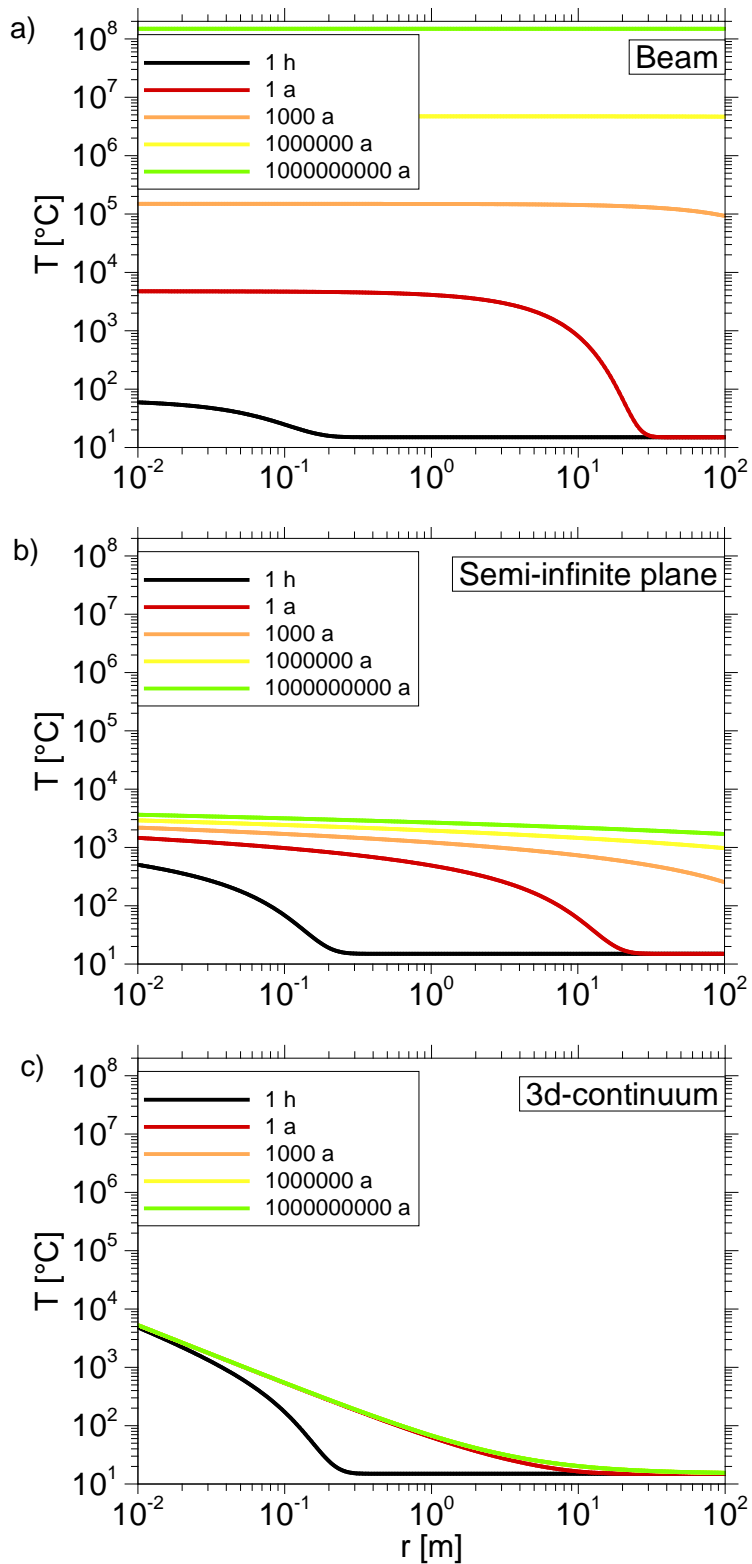


Fig. 7.15 Temperature distributions resulting from a fixed inflow into a) a beam, b) a semi-infinite plane and c) in a 3d-continuum

The effect of constraining the heat to the beam with a constant cross-section can clearly be seen in Fig. 7.15 a) by the fast increase of the boundary temperature in comparison to Fig. 7.15 b) for the plane where a tangential spreading of the temperature front is allowed. The boundary temperature in the plane seems to converge to the steady-state value of the three-dimensional solution depicted in Fig. 7.15 c).

Taking these considerations into account it becomes apparent by looking at Fig. 7.16 that the spherical phase of heat spreading has not yet been reached after 3500 days by any means. It has thus to be concluded that the temperature evolution at the PR has become rather slow but without any further decrease of the heater power it would still increase for quite some time.

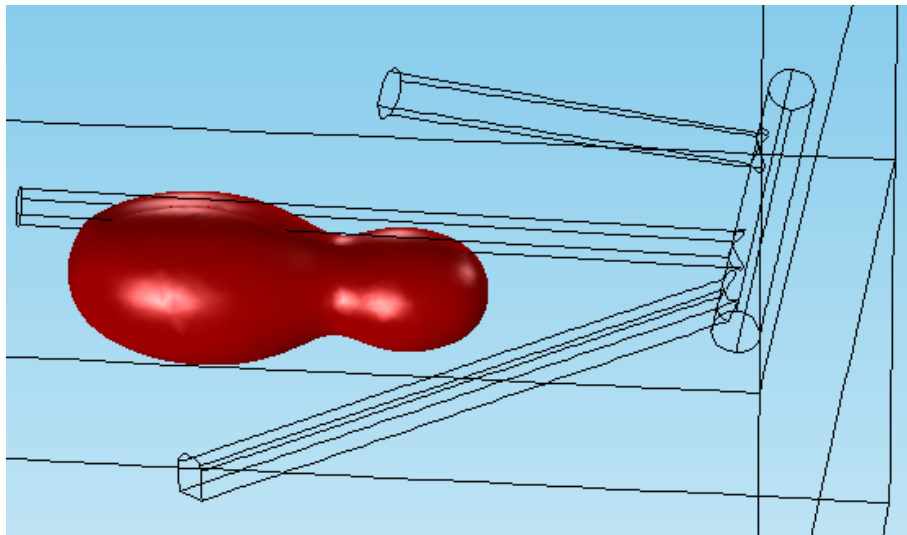


Fig. 7.16 Isoplane for an increase of 10 °C above initial temperature after 3500 days

In case of a significantly longer heating period the model domain has to be expanded. In this case difficulties arise in a standard numerical model with the boundary conditions. Defining Dirichlet or Neumann boundary conditions requires knowledge of the temperature or the temperature gradient at the boundary which can only be known from the calculation that is intended. The remaining natural boundary condition sets the temperature gradient to zero thereby closing the boundary for heat flow. This problem can only be circumvented by a sufficiently large model domain that keeps all the introduced heat inside. Otherwise the temperature field becomes distorted as in Fig. 7.17 which shows the same isoplane as in Fig. 7.16 for a continued simulation over 5000 days.

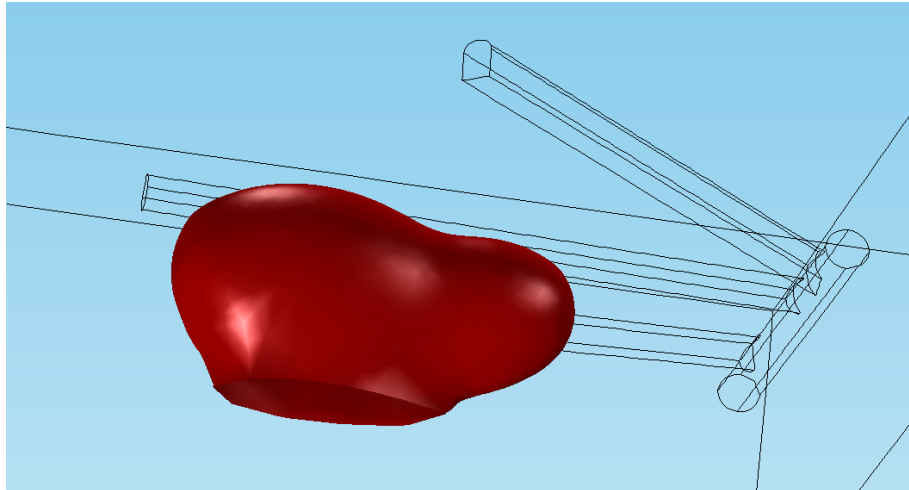


Fig. 7.17 Isoplane for an increase of 10 °C above initial temperature after 5000 days

The resulting temperature distribution after 650 days – that is about 7 weeks after switching on the heaters 5 and 6 – are shown in Fig. 7.18 to put the preceding isoplane plots into perspective. Significant temperature increase is thus rather limited to the range closely around the heaters. The plot is supplemented by Fig. 7.19 showing a vertical cross-section through heater 3 after 1100 days. This figure illustrates the transition between the rectangular heater area in this cross-section to the circular spreading pattern at a certain distance from the heater.

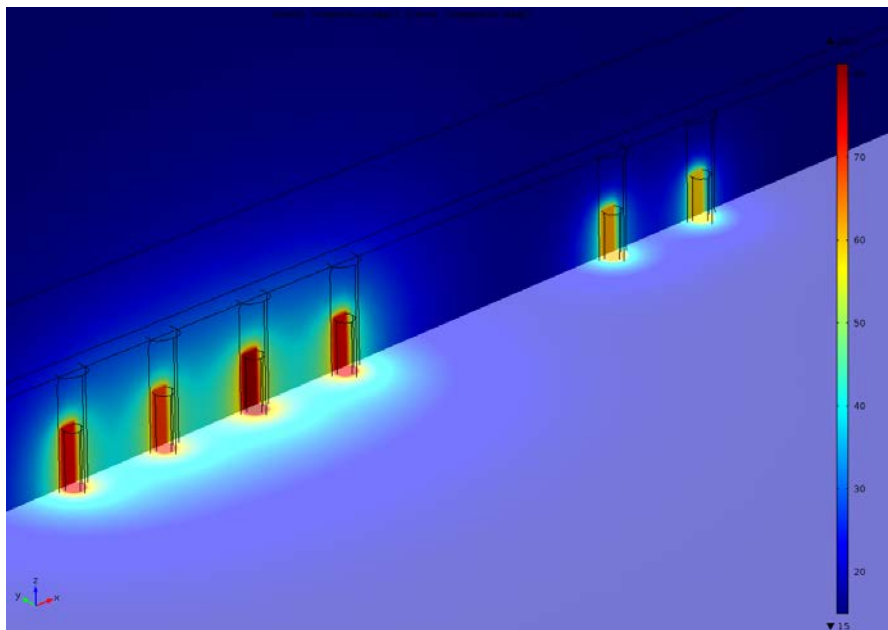


Fig. 7.18 Temperature distribution 650 days after switching on the first four heaters

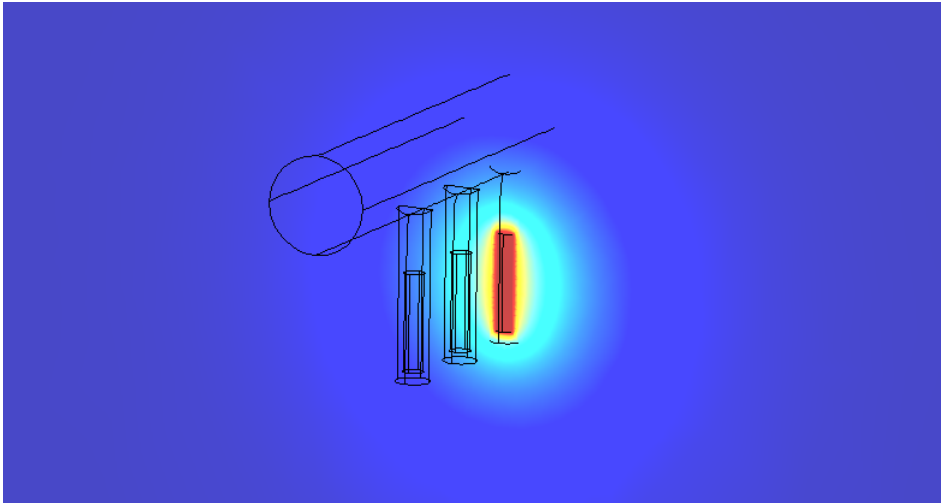


Fig. 7.19 Temperature distribution after 1100 days across heater 3

From the results of this model the evolution of the mean temperature on the borehole surface could easily be derived by a post-processing procedure in COMSOL (see section 6.3.2). The resulting data depicted in Fig. 7.20 was then used as input for the thermo-hydraulic model.

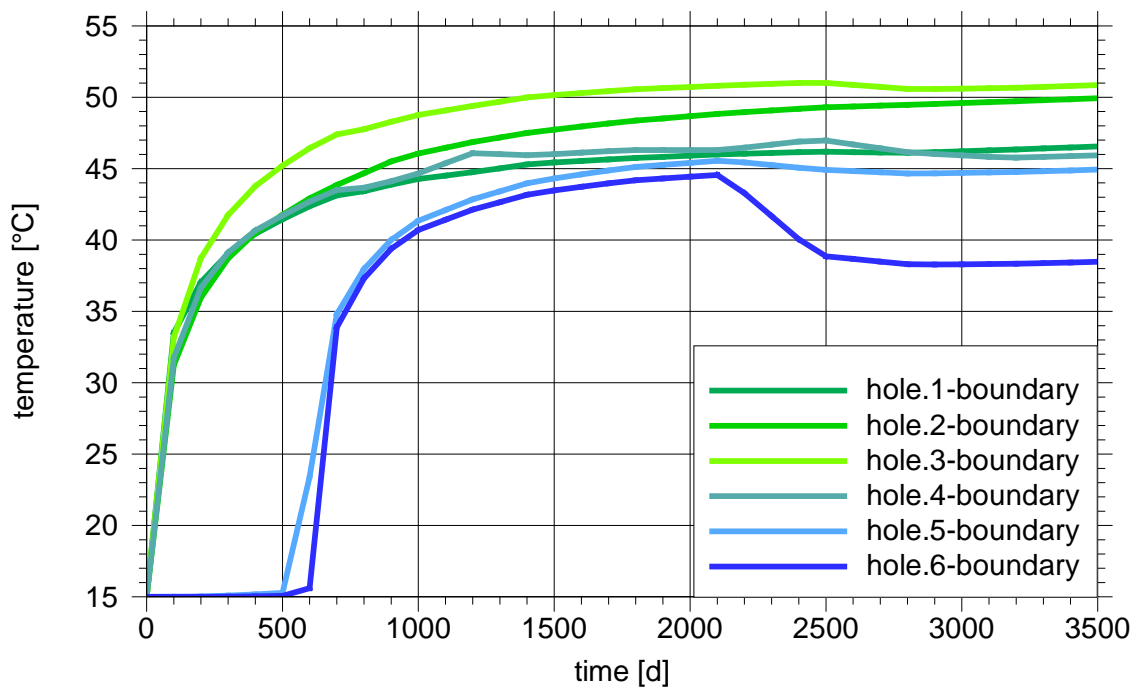


Fig. 7.20 Temperature evolution on the surface of the deposition boreholes

7.3 Thermo-hydraulic flow

7.3.1 State variables

As the maximum temperature in the thermo-hydraulic flow model is defined by the boundary conditions at the deposition boreholes whose evolution in time is depicted in Fig. 7.20, the temperature ranges between 15 °C and about 52 °C. The related water densities are 1017.5 kg/m³ and 991 kg/m³, respectively /IAP 03/, and $1.14 \cdot 10^{-3}$ Pa·s and $0.53 \cdot 10^{-3}$ Pa·s, respectively, /IAP 03/. For reference: Assuming that the Baltic Sea at Äspö can be approximated by a NaCl-solution of 4 % salinity, the difference to pure water is characterised by a density change of about 7 kg/m³ and a difference in viscosity of about $0.02 \cdot 10^{-3}$ Pa s.

7.3.2 Flow field

Based on the assumption that changes in the velocity field due to varying temperatures can most clearly be seen in a vertical cross-section through the PR-tunnel, the modelling results are presented in the following figures in such cross-sections. Fig. 7.21 represents the isothermal state, where the top plot allows for reference to the deterministic fractures while the plot at the bottom also includes the velocity field. Colouring as well as the vector length is logarithmically scaled. While the velocity vectors are only shown for the vertical cross-section, they have still their 3D-orientation meaning that they are not necessarily lying in the plane of the vertical cross-section.

As in the isothermal model, groundwater flow is generally directed from the model boundaries towards the geotechnical openings. Where the velocity field is not substantially influenced by the fractures it forms basically a radial flow pattern with converging streamlines at the PR-tunnel (see Fig. 7.22). This means that the groundwater velocity increases along the streamlines reaching its maximum at the tunnel wall. The flow velocity found here amounts to about $1 \cdot 10^{-9}$ to $2 \cdot 10^{-9}$ m/s. All areas with a groundwater velocity in excess of these $1 \cdot 10^{-9}$ to $2 \cdot 10^{-9}$ m/s are clearly related one way or another to the deterministic fractures.

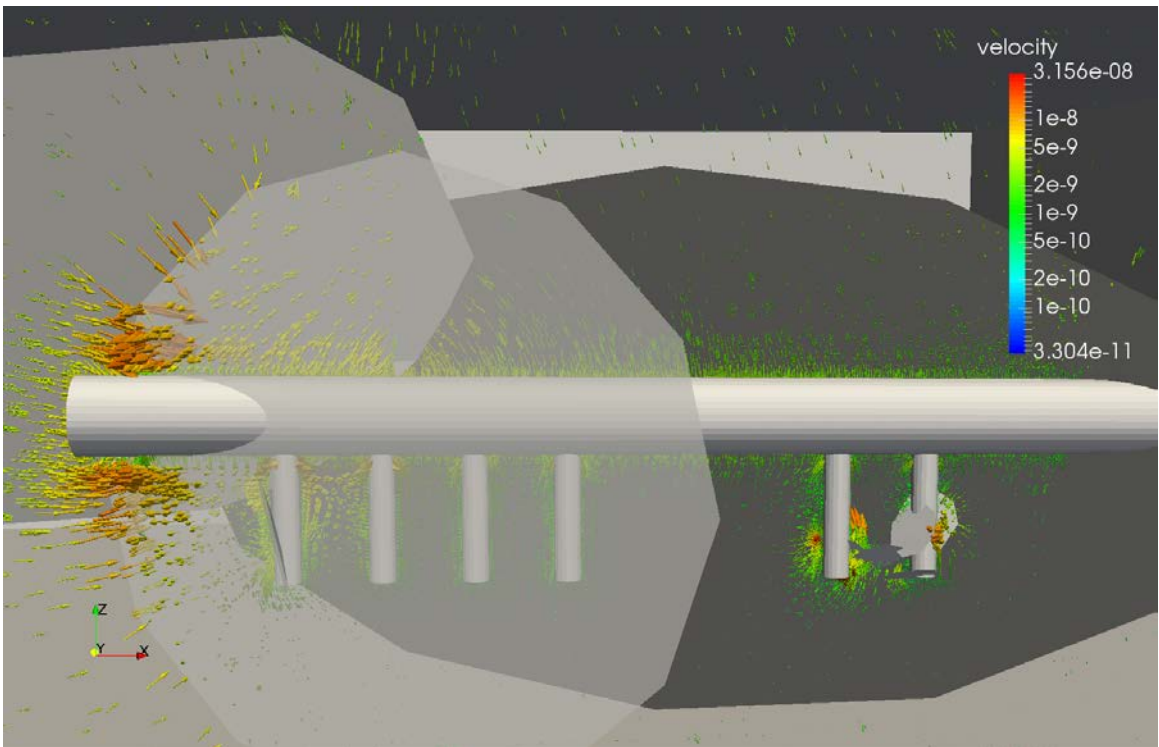
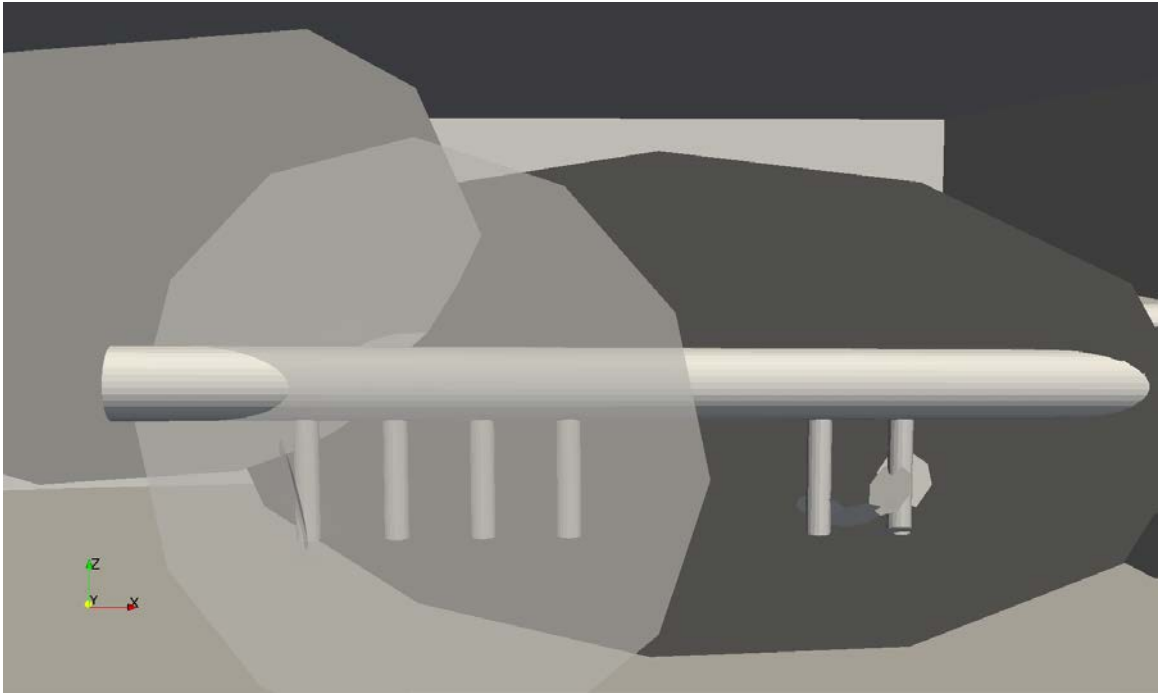


Fig. 7.21 Isothermal, steady-state flow in a vertical cross-section

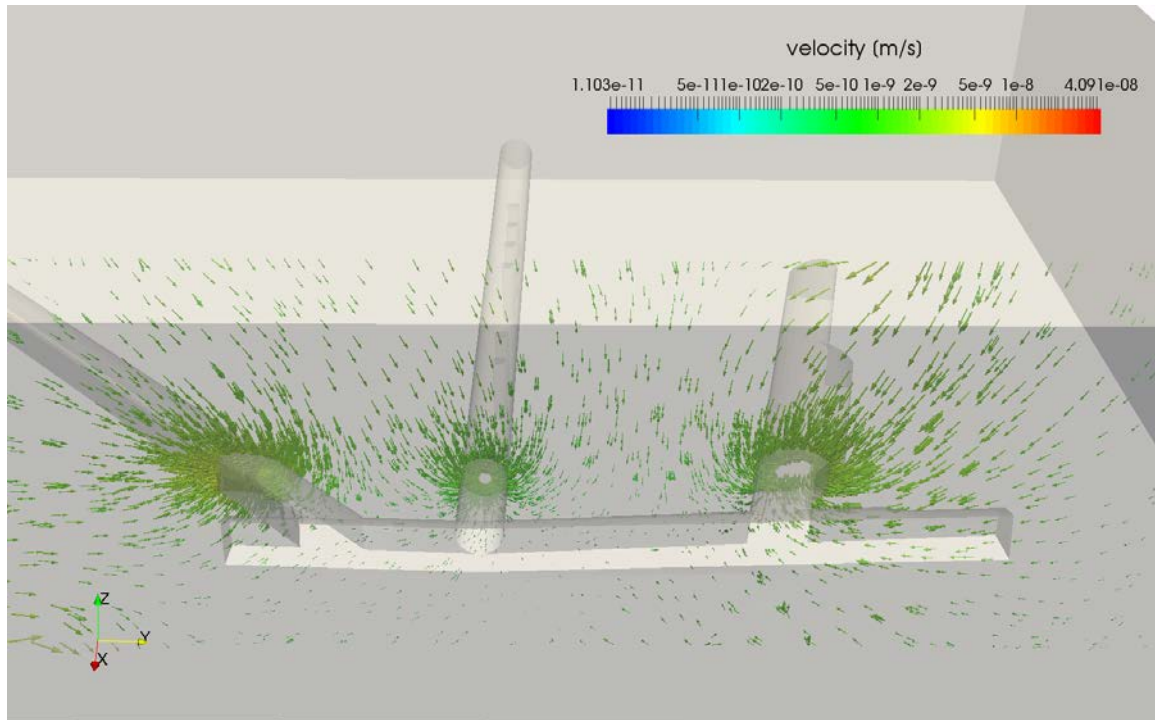


Fig. 7.22 Velocity field around the tunnels after 5 years of heating

The following three figures, Fig. 7.23 to Fig. 7.25, show the flow and temperature field in a vertical and a horizontal cross-section, respectively. Each figure consists of three plots that show flow and heat around the PR-tunnel at the beginning of heating which represents the isothermal conditions, after 500 days shortly before switching on heaters 5 and 6, and after about 5 years. While Fig. 7.23 depicts the situation around the whole PR-tunnel, Fig. 7.24 provides more details in a close-up of section I and Fig. 7.25 shows a close-up of section II. The observable differences in terms of flow velocity are very small and do not amount to a factor of significantly more than 2. No patterns of density-driven flow such as convection cells can be detected in the flow fields in any of these figures.

Heating has essentially the effect of decreasing the flow resistance exerted by the water. The density differences due to heating amount to less than 10 % and are thus negligible. But the temperature induced decrease of viscosity amounting to a factor of $1.14 \cdot 10^{-3} / 0.53 \cdot 10^{-3} = 2.15$ fits fairly well the observed local increase of the flow velocity.

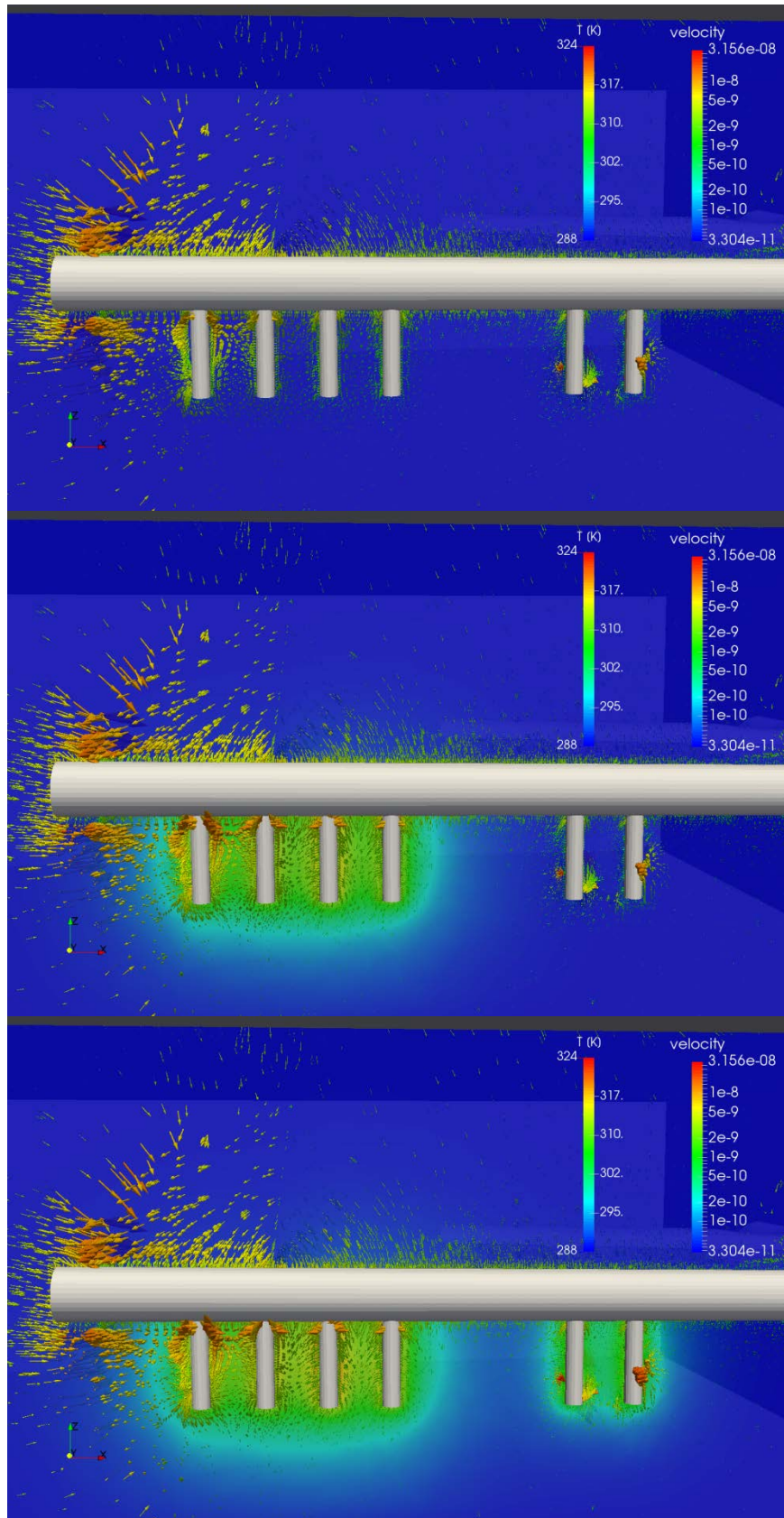


Fig. 7.23 Temperature and flow field after 0, 500 days and 5 years of heating

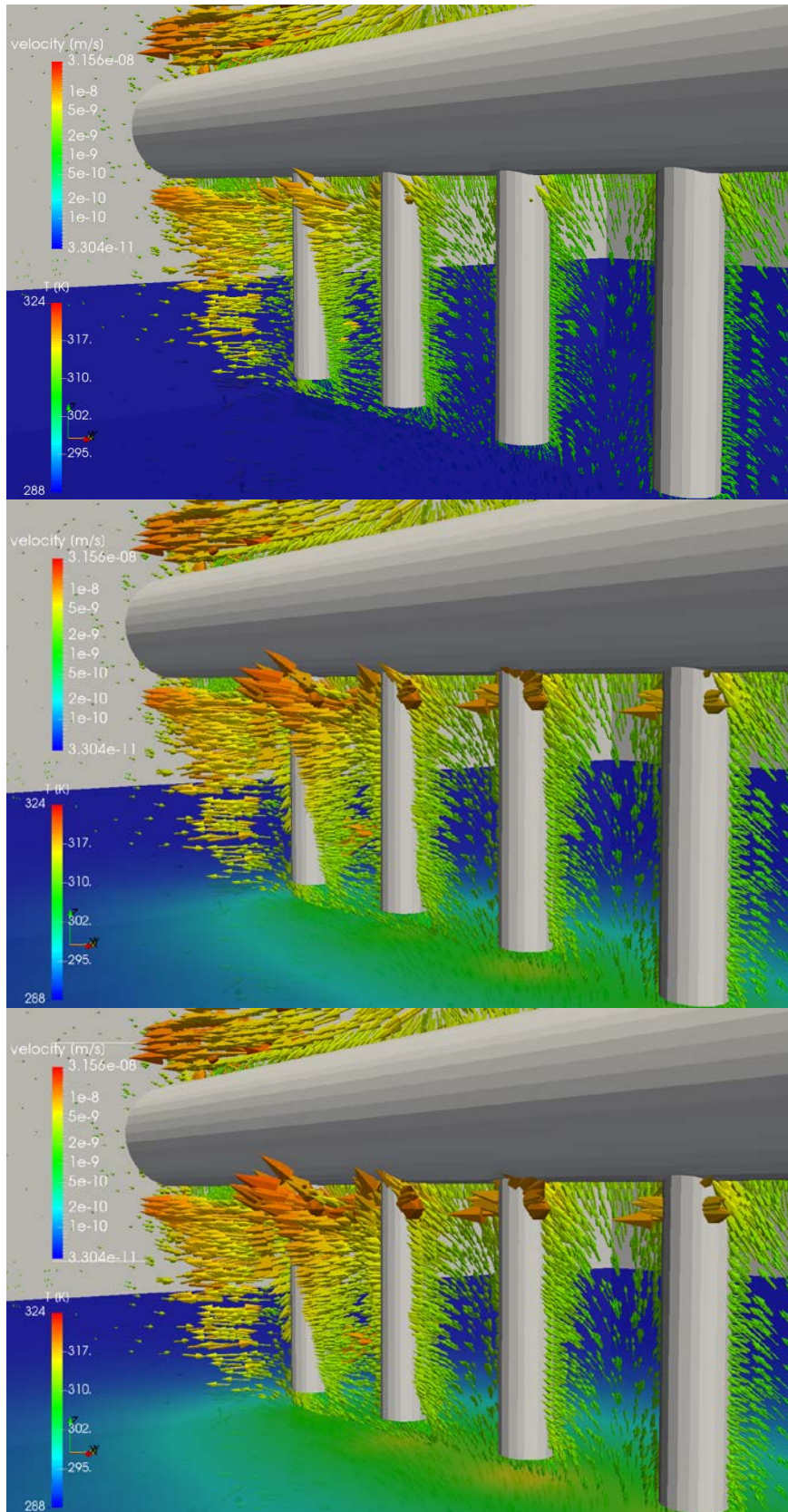


Fig. 7.24 Temperature and flow field in section I after 0, 500 days and 5 years

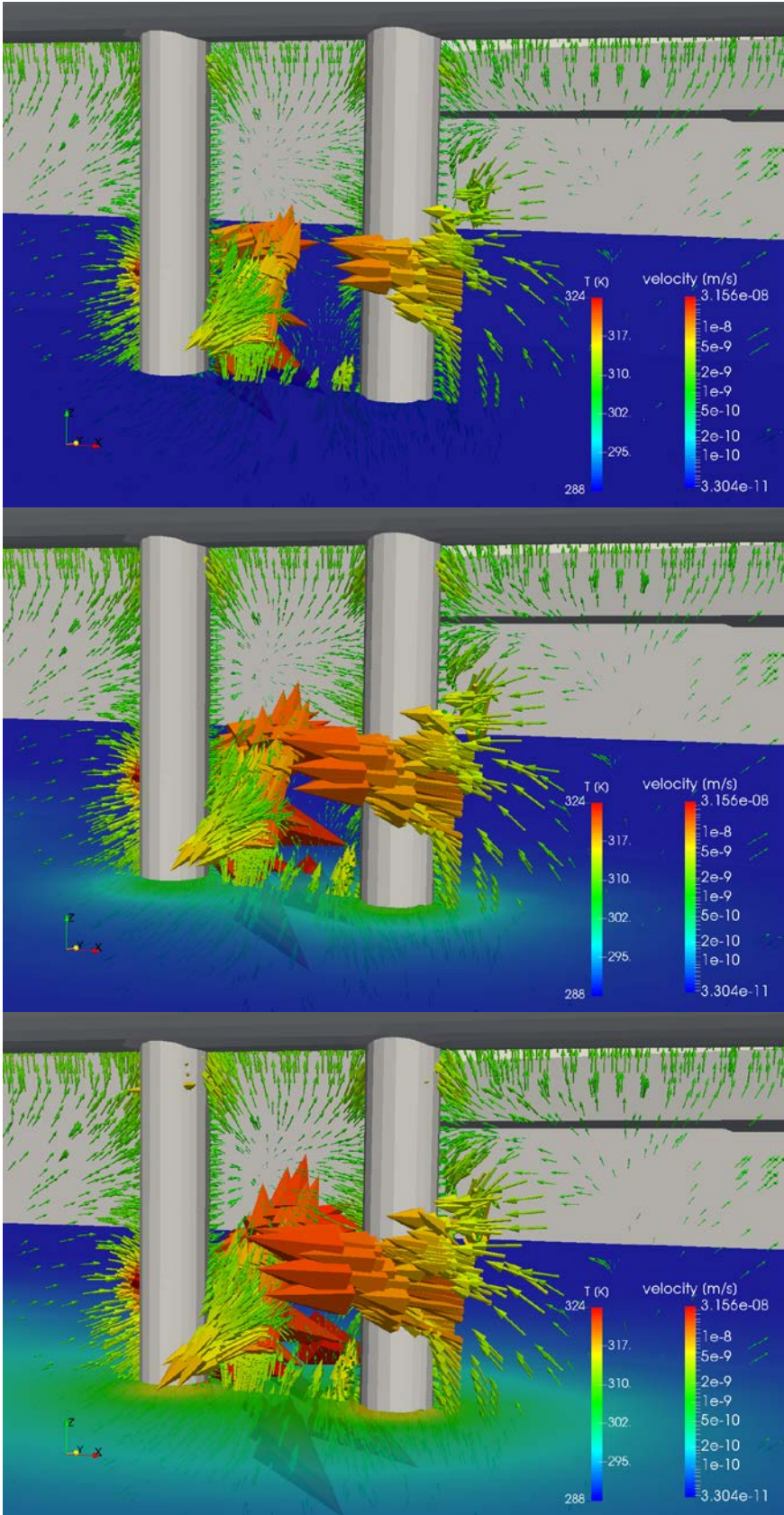


Fig. 7.25 Temperature and flow field in section II after 0, 500 days and 5 years

7.3.3 Outflow

The thermo-hydraulic model starts with isothermal conditions, meaning when the heaters were not being switched on, yet. The results at the beginning of the simulation in terms of outflow rates should therefore be essentially the same as those for the isothermal model as described in section 7.1.2. In the following, three things are compared with the isothermal results: the initial outflow rate, the dynamics of changes in outflow rates induced by heating and the maximum difference in outflow between initial and end state of the simulation.

Deposition holes

The fluxes depicted in Fig. 7.26 at the beginning of the simulation are consistent with the results of the isothermal model (see Tab. 7.3). Calculated outflow into the depositions boreholes of section I (holes 1 to 4) begins to increase immediately at the beginning of the simulation while it remains at the initial value for about 550 days at deposition boreholes 5 and 6 (section II). Only then, the outflow rate increases there as well. All six curves seem to converge towards a steady-state value even if this is not entirely clear for holes one and two. After ten years of simulated time the outflow rates have increased by a factor of 1.4 to 1.7 under the influence of heating (see Tab. 7.3).

Tab. 7.3 Outflow rates [kg/s] without contribution of the fractures

Outflow at	dep.h 1	dep.h 2	dep.h 3	dep.h 4	dep.h 5	dep.h 6
Isothermal ¹²	$1.17 \cdot 10^{-04}$	$1.19 \cdot 10^{-04}$	$1.09 \cdot 10^{-04}$	$1.03 \cdot 10^{-04}$	$7.46 \cdot 10^{-05}$	$6.34 \cdot 10^{-05}$
TH-model; t=0a	$1.15 \cdot 10^{-04}$	$1.17 \cdot 10^{-04}$	$1.07 \cdot 10^{-04}$	$1.01 \cdot 10^{-04}$	$7.32 \cdot 10^{-05}$	$6.22 \cdot 10^{-05}$
TH-model; t=10a	$1.76 \cdot 10^{-04}$	$1.89 \cdot 10^{-04}$	$1.84 \cdot 10^{-04}$	$1.58 \cdot 10^{-04}$	$1.04 \cdot 10^{-04}$	$8.84 \cdot 10^{-05}$
ratio	1.53	1.62	1.72	1.56	1.42	1.42

Since changes in the outflow rate are apparently correlated with the local temperature, the dynamics of outflow can be explained by interpreting the results of the thermal model. It is thus that outflow in section I begins to increase immediately as the simulation begins with switching on the heaters in section I while heating in section II commences only after about 550 days causing an increased outflow at those deposition boreholes

¹² from Tab. 7.1

afterwards. The decrease of flow into deposition borehole 6 appears to be result of the temporary power shortage in heater 4 between days 1880 and 2190 and the continued decrease by one third in heater 6 over days 2290 to 2470.

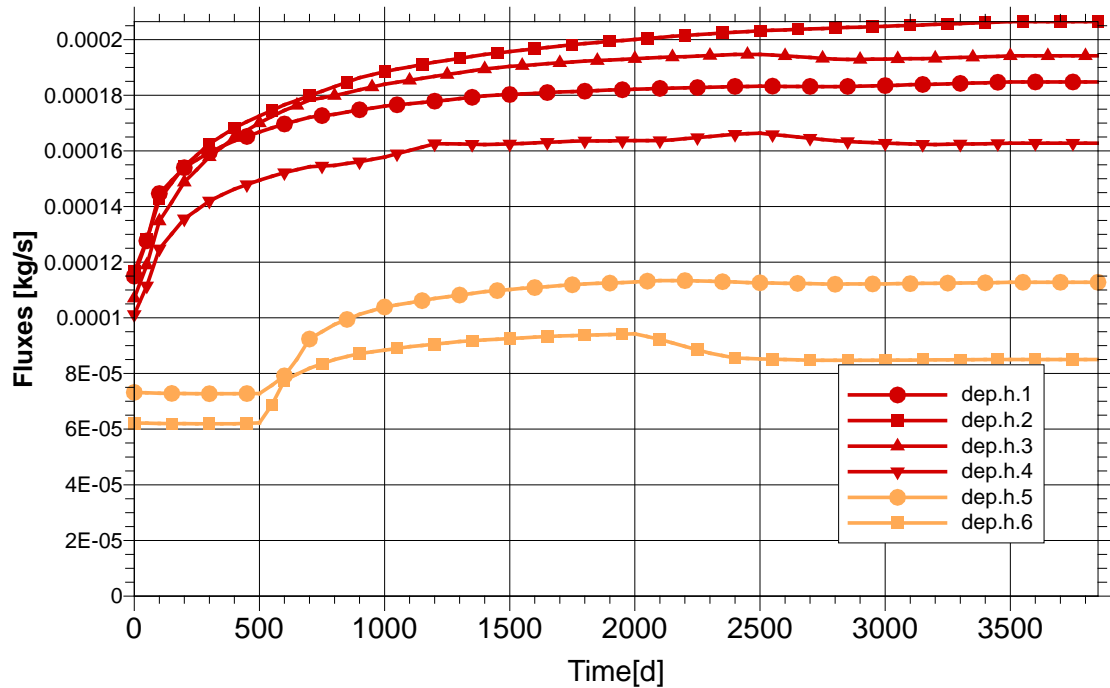


Fig. 7.26 Outflow dynamics for the deposition holes

Boreholes 2 and 3 are flanked by boreholes 1 and 4 they and should therefore show a higher temperature and thus a higher outflow rate than the flanking ones. This holds true even despite the loss of heater 2 after about 1200 days.

Large deterministic fractures

There is no significant change of outflow with heating from the large fractures as depicted in Fig. 7.27 and underpinned by Tab. 7.4. Maximum change is by about 6 %. Increase in the assumed fracture is monotonic until the maximum is reached at about 2000 days simulated time.

Tab. 7.4 Comparison of outflow rates of large deterministic fractures

Outflow [kg/s] at:	Northern fracture	Southern fracture	Assumed fracture
Isothermal	$6.55 \cdot 10^{-03}$	$9.31 \cdot 10^{-03}$	$3.97 \cdot 10^{-02}$
TH-model; t=0a	$6.43 \cdot 10^{-03}$	$9.13 \cdot 10^{-03}$	$3.82 \cdot 10^{-02}$
TH-model; t=10a	$6.66 \cdot 10^{-03}$	$9.65 \cdot 10^{-03}$	$4.06 \cdot 10^{-03}$
ratio	1.04	1.06	1.06

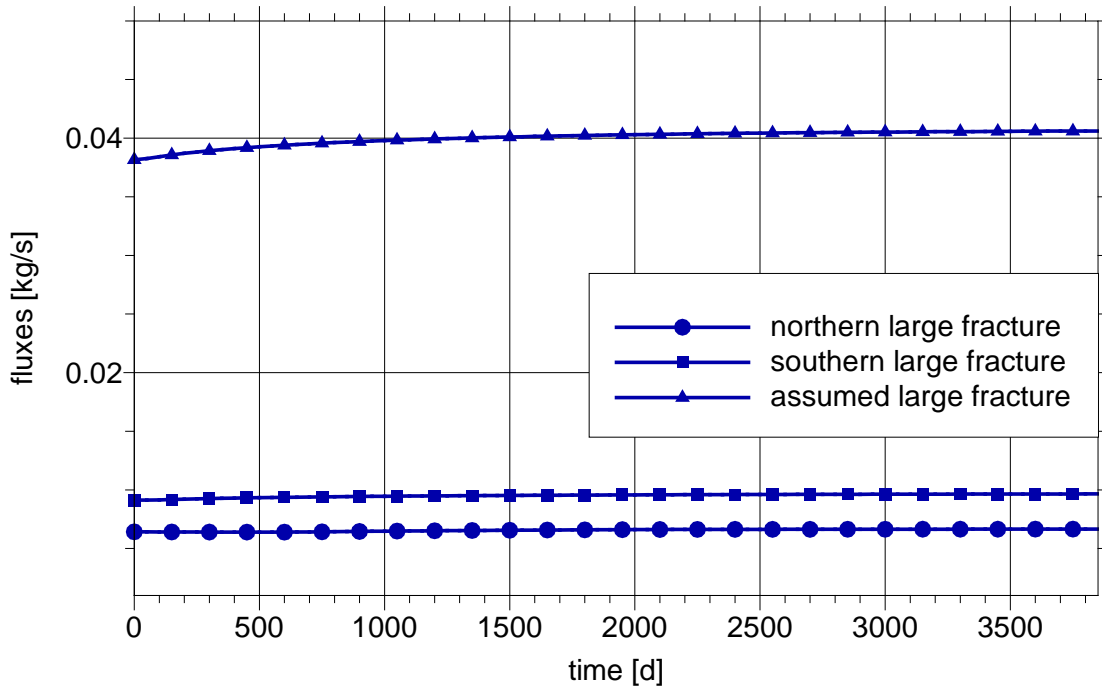


Fig. 7.27 Outflow dynamics for the large fractures

As the close-up in Fig. 7.29 shows, the assumed as well as the southern fracture react to turning on the heaters in section I while the northern fracture responds rather to switching on heaters in section II. This is of course consistent with the location where these three fractures intersect the geotechnical openings of the PR-excavations.

The comparatively low sensitivity of outflow from the large fractures to heating may be explained by the temperature distributions in these fractures. Fig. 7.29 and Fig. 7.30 show clearly that only a fraction of the intersection with the PR-tunnel is affected by heating if at all. Particularly the circumferences of the fractures that contribute a considerable fraction to the flow in the fracture (see section 7.1.4) have basically not been heated. The increase in outflow can therefore be attributed to the faces of the fractures where a significant increase of temperature can be observed.

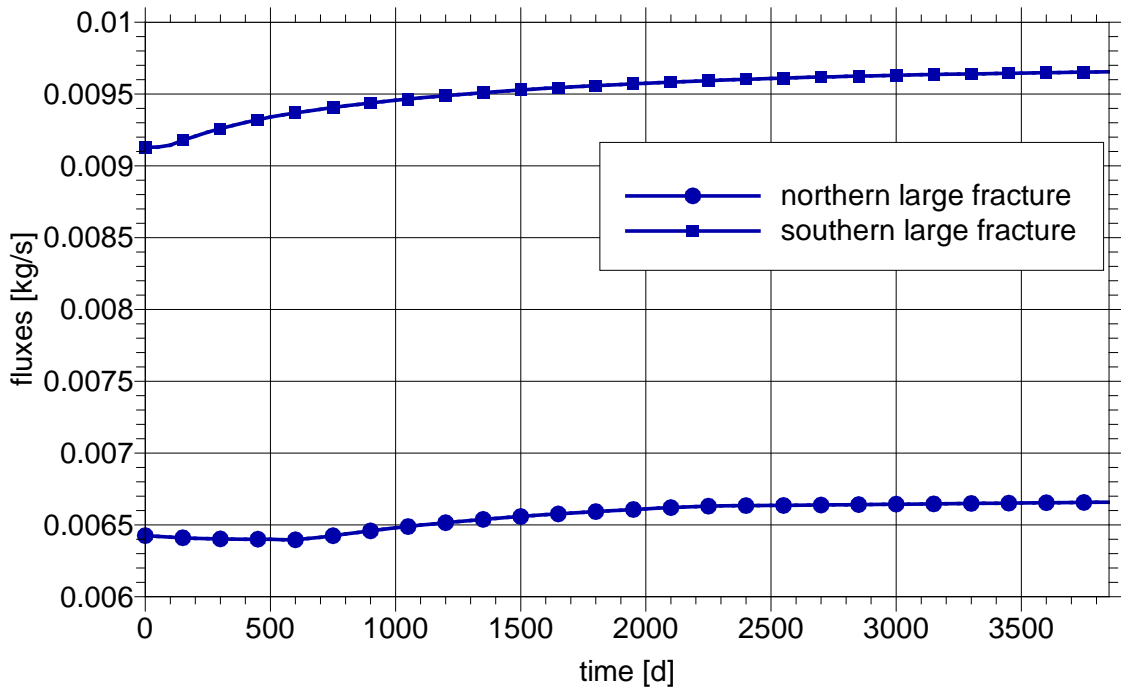


Fig. 7.28 Outflow dynamics for the northern and the southern fracture (close-up)

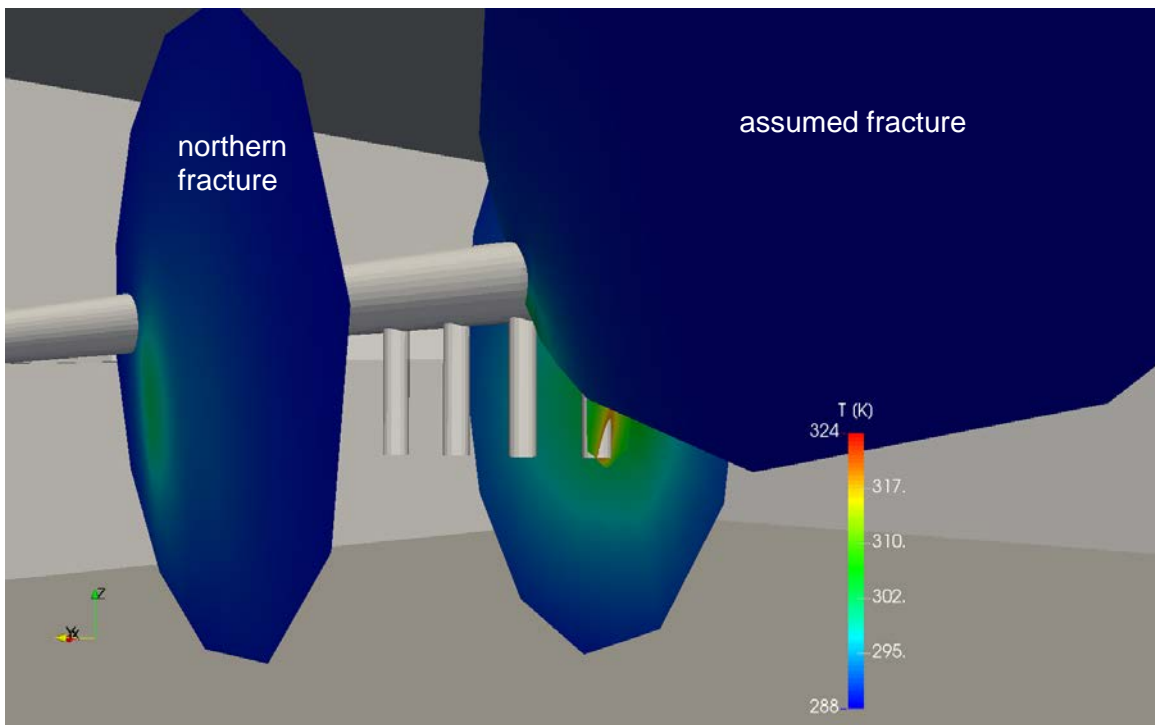


Fig. 7.29 Temperature distribution in the large fractures after 10 years model time

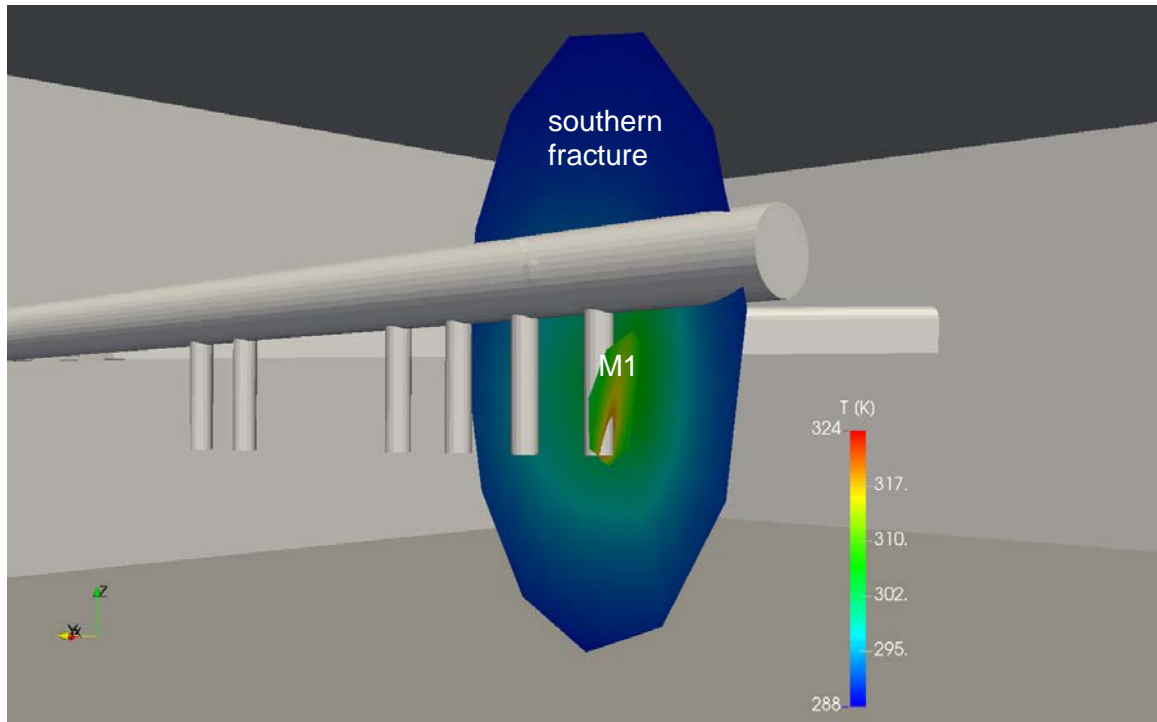


Fig. 7.30 Temperature in the southern deterministic fracture and fracture M1 after 10 years model time

Minor deterministic fractures

The TH-model is again confirmed by the comparison of the flux data with the results from the isothermal model as compiled in Tab. 7.5.

Tab. 7.5 Comparison of outflow rates for minor deterministic fractures¹³

Outflow [kg/s] at:	M1	M2	M4	M5	M6
Isothermal	$4.95 \cdot 10^{-04}$	$1.61 \cdot 10^{-04}$	$5.56 \cdot 10^{-05}$	$5.04 \cdot 10^{-07}$	$1.41 \cdot 10^{-04}$
TH-model; t=0a	$4.87 \cdot 10^{-04}$	$1.59 \cdot 10^{-04}$	$5.46 \cdot 10^{-05}$	$4.95 \cdot 10^{-07}$	$1.39 \cdot 10^{-04}$
TH-model; t=10a	$7.50 \cdot 10^{-04}$	$2.35 \cdot 10^{-04}$	$7.31 \cdot 10^{-05}$	$6.81 \cdot 10^{-07}$	$1.88 \cdot 10^{-04}$
ratio	1.54	1.48	1.34	1.38	1.35

Minor deterministic fracture M1 cuts through deposition hole 1 (see Fig. 7.30) and is thus located in the immediate vicinity of a heater. As M1 intersects hole 1 almost entirely,

¹³ Note that minor fracture M3 does not connect to any deposition hole.

outflow from M1 increases by a factor of 1.54 (see Tab. 7.5) which is in line with the general increase of outflow into hole 1 by a factor of 1.53 (see Tab. 7.3).

Since M1 is the only minor fracture in section I, the referring flux curve is the only minor fracture responding immediately to heating as depicted in Fig. 7.31. All others show a flux increase rather when heating in section II was commenced at about day 550. The absolute value of the fluxes differ considerably but not because of heating which affects all minor fractures more or less in the same way (see Fig. 7.32). These differences are due to fracture permeability that was already applied in the isothermal model.

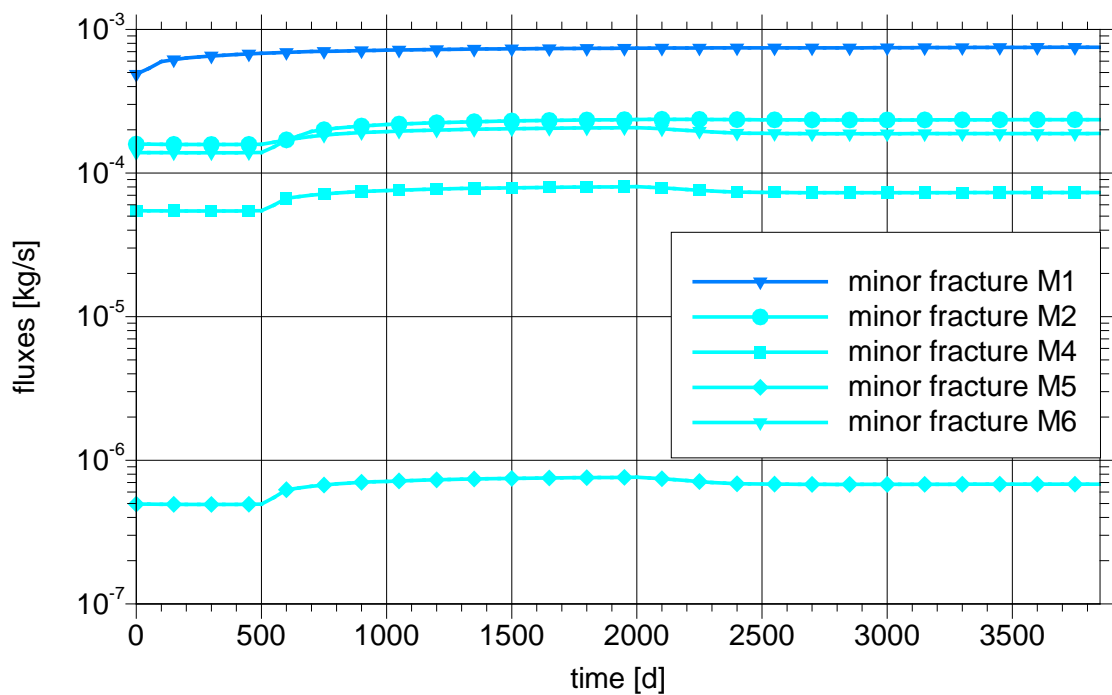


Fig. 7.31 Outflow dynamics for the minor fractures

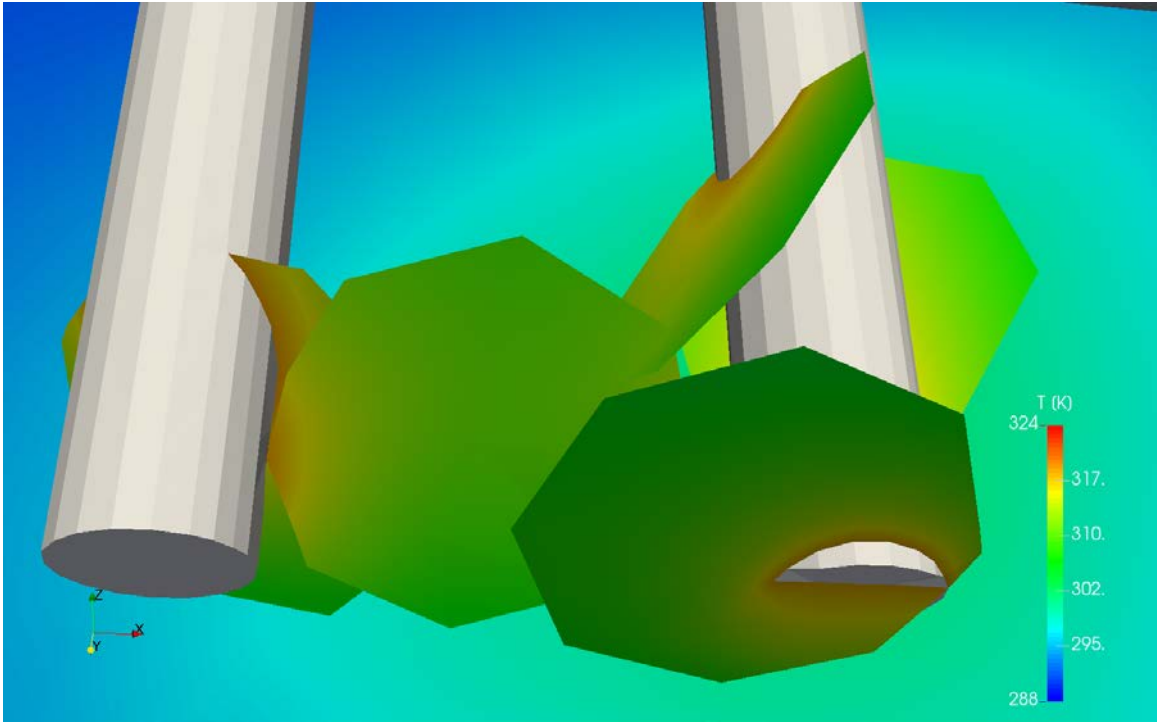


Fig. 7.32 Temperatures for the minor fractures after 10 years model time

PR-tunnel (detailed)

The differences between fluxes from the isothermal and the TH-model are slightly higher than the previously discussed ones, but not disturbingly so (see Tab. 7.6). The maximum increase in flow rate does not exceed 16 % which can be found for tunnel sections related to heater section I (PR-568-575 to PR-581-587). Also above 10 % are the tunnel section related to heater section II (PR-545-551 to PR-551-557). The evolution of fluxes for these tunnel sections is again related to the different switch-on times of sections I and II as depicted in Fig. 7.33. This, however, is hardly recognisable among all the similar other curves.

Tab. 7.6 Outflow rate for segments of the PR-tunnel without flow from the fractures

Outflow [kg/s] at	Isothermal	TH-model; t=0a	TH-model; t=10a	ratio	
PR-tunnel-rest	$4.27 \cdot 10^{-04}$	$4.18 \cdot 10^{-04}$	$4.20 \cdot 10^{-04}$	1.00	
PR-527-533	$1.40 \cdot 10^{-04}$	$1.38 \cdot 10^{-04}$	$1.40 \cdot 10^{-04}$	1.01	
PR-533-539	$1.67 \cdot 10^{-04}$	$1.64 \cdot 10^{-04}$	$1.70 \cdot 10^{-04}$	1.04	
PR-539-545	$2.37 \cdot 10^{-04}$	$2.33 \cdot 10^{-04}$	$2.50 \cdot 10^{-04}$	1.07	
PR-545-551	$2.39 \cdot 10^{-04}$	$2.34 \cdot 10^{-04}$	$2.61 \cdot 10^{-04}$	1.12	Section II
PR-551-557	$2.52 \cdot 10^{-04}$	$2.48 \cdot 10^{-04}$	$2.72 \cdot 10^{-04}$	1.10	
PR-557-562	$2.74 \cdot 10^{-04}$	$2.70 \cdot 10^{-04}$	$2.89 \cdot 10^{-04}$	1.07	
PR-562-568	$2.99 \cdot 10^{-04}$	$2.93 \cdot 10^{-04}$	$3.25 \cdot 10^{-04}$	1.11	
PR-568-575	$3.88 \cdot 10^{-04}$	$3.82 \cdot 10^{-04}$	$4.43 \cdot 10^{-04}$	1.16	Section I
PR-575-581	$3.74 \cdot 10^{-04}$	$3.70 \cdot 10^{-04}$	$4.30 \cdot 10^{-04}$	1.16	
PR-581-587	$4.14 \cdot 10^{-04}$	$4.12 \cdot 10^{-04}$	$4.67 \cdot 10^{-04}$	1.13	
PR-587-593	$3.92 \cdot 10^{-04}$	$3.87 \cdot 10^{-04}$	$4.16 \cdot 10^{-04}$	1.07	
PR-593-600	$7.74 \cdot 10^{-04}$	$7.60 \cdot 10^{-04}$	$7.74 \cdot 10^{-04}$	1.02	

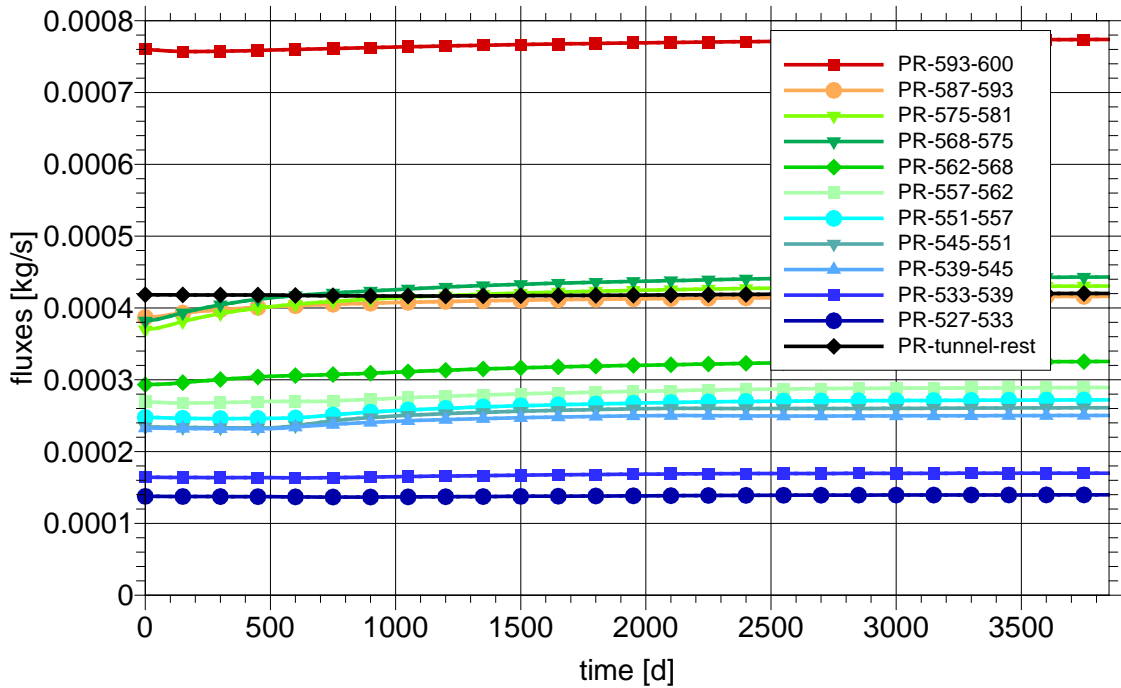


Fig. 7.33 Outflow dynamics for sections of the PR-tunnel

Whole tunnels

Integral flow rates for four tunnels/tunnel sections, namely the PR-tunnel, the G-tunnel and the I+- as well as the J+-section, were determined as well. As the flux curves in Fig. 7.34 and the flow rates compiled in Tab. 7.7 show, there is virtually no influence from heating recognisable in any other tunnel than the PR. Total outflow in the PR-tunnel increases only by 6 %.

Tab. 7.7 Comparison of outflow rates for whole tunnels

Outflow [kg/s] at	PR-tunnel	G-tunnel	I+-tunnel	J+-tunnel
Isothermal	$5.99 \cdot 10^{-02}$	$4.15 \cdot 10^{-03}$	$1.31 \cdot 10^{-04}$	$5.03 \cdot 10^{-04}$
TH-model; t=0a	$5.80 \cdot 10^{-02}$	$4.07 \cdot 10^{-03}$	$1.29 \cdot 10^{-04}$	$4.93 \cdot 10^{-04}$
TH-model; t=10a	$6.16 \cdot 10^{-02}$	$4.08 \cdot 10^{-03}$	$1.29 \cdot 10^{-04}$	$4.93 \cdot 10^{-04}$
ratio	1.06	1.00	1.00	1.00

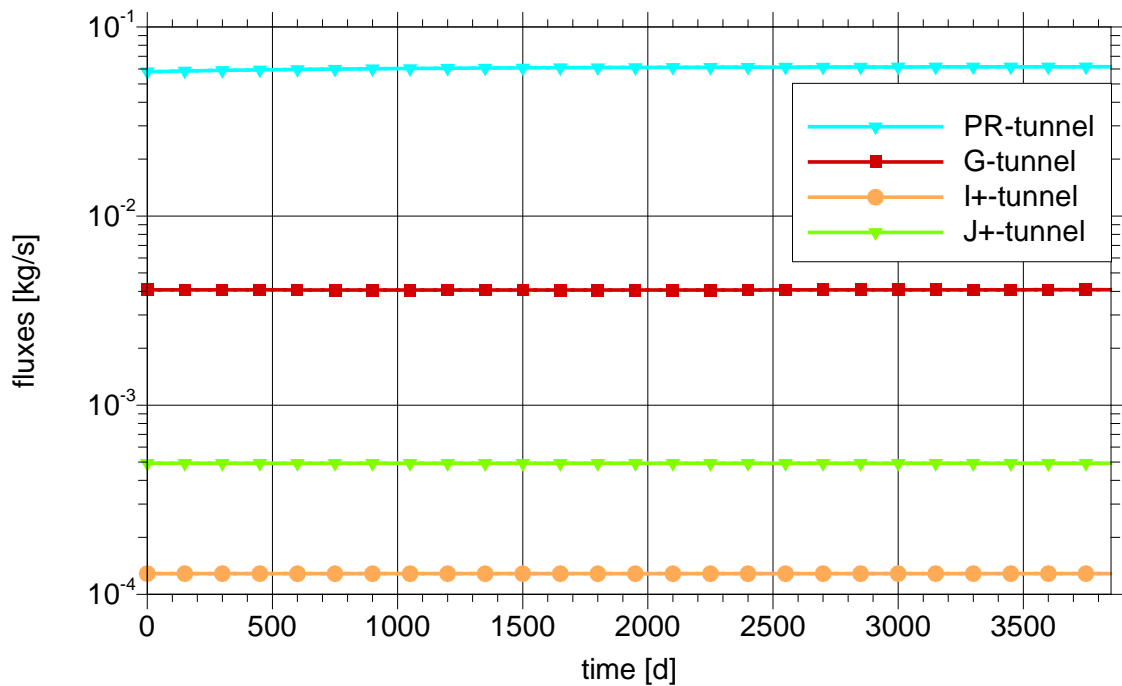


Fig. 7.34 Outflow dynamics for the tunnels in the model

8 Discussion

Three models for groundwater and heat flow in the granitic rock around the PR-tunnel at the HRL Äspö have been set up. The isothermal groundwater flow model provides a reference for the isothermal flow conditions, the heat flow model provides temperature boundary conditions and the thermo-hydraulic groundwater flow model investigates the influence of heat flow from the heated canisters on groundwater flow by comparison of the resulting flow field with the isothermal flow.

A hybrid approach as used for modelling the BRIE has been chosen to represent the rock in the model¹⁴. While large fractures are deterministically embedded in the rock, the hydraulic effect of the background fractures is captured by an appropriate increase of rock permeability. Also as being found necessary for successfully modelling flow at the BRIE, a narrow skin zone with a decreased permeability was assumed around tunnels and boreholes.

Large deterministic fractures were firstly constructed from trace lines along tunnels and boreholes in concordance with the results from outflow measurements. Becoming only later aware of the extensive hydrotesting by /RHÉ 01/ allowed for an interesting comparison of the theoretically derived fractures and the hydraulically determined ones. There was a surprisingly good match of location and orientation of both sets of fractures. In terms of fracture detection both methods complimented each other. Realistic size and permeability, however, could only be determined in the field. The outflow measurements in the PR-tunnel indicated a missing large deterministic fracture in the area of an untested sector in the otherwise dense field of test boreholes. Based on the trace lines as well as the properties of the known fractures another large one was assumed for the model.

Processes considered in the models are single-phase, single-component groundwater flow and heat conduction in the water-rock system as well as heat convection in the moving groundwater. A possible influence of salinity was neglected due to the little differences of the salt concentration found in the groundwater.

¹⁴ Alternative concepts to represent the fractures are discussed in more detail in /KRÖ 17a/.

Of the three outflow measurements in the depositions boreholes – total outflow, localized outflow and the diaper measurements in deposition holes 2, 3, 5, and 6 – the total outflow measurements appeared to be the most helpful ones. Localized outflow is only very loosely related to the fracture traces in the boreholes and bears no relation at all to the minor deterministic fractures determined by the hydrotesting. The same applies to the diaper measurements where, additionally, the pattern of water distribution indicated by the diapers looks very much like flow from the top of the borehole rather than flow from the borehole wall.

Very helpful were the section-wise measurements of outflow along the PR-tunnel. Reliability of fracture detection was increased by detailed information about outflow rates. It also proved to be valuable for model calibration. By contrast, outflow data from other tunnels was less decisive for calibration purposes not least because very little was known about the fractures around these other tunnels.

The dense array of temperature sensor in the buffer, in the rock around the deposition boreholes and in the backfill in the PR-tunnel provided an excellent data base for the heat flow model. Calculated temperatures show a satisfying match between measurements and model results even without calibration. This is once more evidence of the good-naturedness of the thermal problem. But it demonstrates also the admissibility of decoupling the thermal from the hydraulic calculation, in other words, it shows that the impact of convective heat transport is negligible.

Pressure boundary conditions were chosen for both groundwater flow models. Hydraulic pressure for the outer boundaries meaning the planar sides of the model, were extracted from a regional scale flow model. These data were provided by SKB. Atmospheric pressure was assigned to tunnel and borehole walls. For the flow models this means that all model boundaries were open to flow which requires some attention. During the operational phase of the experiment, the PR-tunnel and the deposition boreholes were filled with backfill and buffer material, respectively. As discussed in more detail in Appendix C the open flow boundary can nevertheless be considered to be realistic for the first few hundred days of the experiment since the bentonite in these geotechnical openings draws potentially more water than can be provided by the rock. At later times the model becomes unrealistic but gives an impression about what to expect from further heating.

For the heat flow model, the initial rock temperature of 15 °C was maintained at the outer boundaries while the recorded power consumption for each of the six heaters were distributed over the volume of the related deposition boreholes. Note, where heaters, buffer and backfill had been emplaced before the heaters were switched on there were no inner boundaries.

The performance of d^{3f}++ with respect to ambitious features in the flow field was satisfying. The results included sharp velocity contrasts across the fractures in terms of magnitude and direction, increased flow at tunnel ends and fracture edges as well as the complex flow field where matrix, tunnel skin and borehole skin met. A concentration of outflow where tunnel and borehole skin intersect, could be observed.

Calibration of the isothermal model based on the available outflow data required an increase of matrix permeability and of the permeability of the assumed fracture by a factor of 5 while skin permeability had to be decreased by a factor of 5. Representation of pre-installation flow conditions at the PR based on the model concept for flow at the BRIE can thus be considered to be successful. Note that in preparation of a large-scale model for Äspö, the hydrologic data collected by SKB in the region showed a relation between hydraulic conductivity and test scale. Comparing the permeability of the matrix including background fractures and model size for the BRIE and the PR ($k_{\text{BRIE}}=1 \cdot 10^{-10} \text{m}^2$, $K_{\text{PR}}=5 \cdot 10^{-10} \text{m}^2$, $l_{\text{max BRIE}}=40 \text{m}$, $l_{\text{max PR}}=150 \text{m}$) reveals the same trend as the data based on hydrotesting (see Fig. 8.1).

The maximum temperature measured by the sensors that were used for calibrating the heat flow model, amounted to about 56 °C and was found at the wall of deposition borehole 6 at mid-height of the heater. The biggest error in the model of about 2 – 3 °C occurred at the bottom of the tunnel backfill above the deposition hole which is probably caused by a mistake in the model set-up. A significant temperature increase meaning more than 10 °C is rather limited to the range closely around the heaters and does not reach the top of the PR-tunnel even after 3500 days.

The principle mode of heat transport changes with time from 1-d to 2-d to 3-d. Heat flow is radially directed away from the cylindrical heater and can be approximated as a one-dimensional process in the first instance. Later on, the radial character of this heat flow

dominates except at the ends of the heater. Even later, the heated areas around the heaters overlap and form eventually a more or less spherical zone.

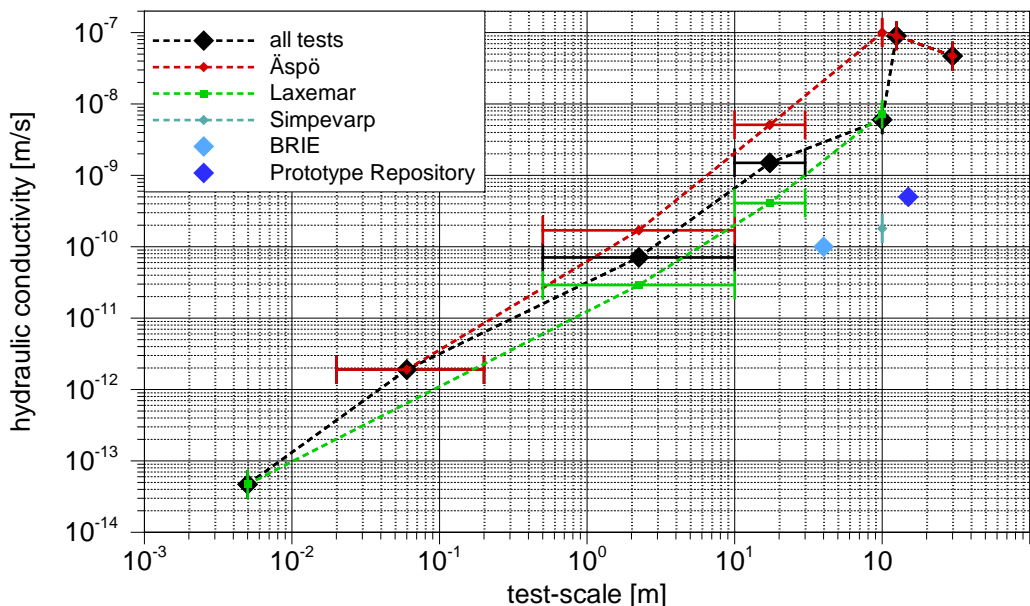


Fig. 8.1 Relation of test/model scale and measured/calibrated hydraulic conductivity

The results from the non-isothermal groundwater flow model show that heating in the flow model has essentially the effect of decreasing the flow resistance exerted by the groundwater. The flow pattern meaning the streamlines, are basically unaffected. Changes in the outflow rate into the deposition boreholes coincide with an increase in temperature and are thus limited to the vicinity of the deposition holes. The minor deterministic fractures lie in the heated rock volume and therefore show an increase in flow up to about 50 %. By contrast, no significant change of outflow with heating can be observed from the large fractures because water is mostly drawn from areas without significant temperature increase. While the influence of heating is noticeable along the PR-tunnel it is largely negligible as it leads to a local increase of outflow of not significantly more than 10 %. The total increase over the PR-tunnel amounts even only to 6 %. Tunnels G, I+ and J+ being located far outside the heated range show no influence of heating in terms of outflow changes at all.

9 Conclusions

Judging from the successful calibration exercise for the BRIE- and for the PR-model, the hybrid approach for representing the rock at Äspö with respect to hydrology appears to be viable. Smearing the effect of background fractures over the matrix, however, seems to require a certain scaling. While two data points are certainly not enough for an extrapolation to other possible model domains the trend to higher permeabilities in the background fracture-matrix system with increasing model size can also be found in the data for hydraulic testing in the general area of Äspö. It would stand to reason to assume that the probability of stronger conducting features increases with testing/model size resulting in an increased overall permeability. The undoubtedly existing relation between the length of a test borehole and the resulting determined permeability should thus give an indication for the extent of the influence of background fractures on the flow.

Heating by the canister dummies in the PR-test affected only a very limited rock volume in the vicinity of the heaters. The effect was basically that of locally lowering the resistance to flow by changing density and viscosity of the water. At that, even the maximum temperature increase in the rock adjacent to the deposition boreholes was quite moderate, not exceeding 56 °C, leading to a local increase of outflow by not more than a factor of about 2.

The boundary conditions for the deposition boreholes and the PR-tunnel could have been better adapted to the conditions of the operational phase of the PR if they had been switched from free outflow to prescribed outflow according to the uptake of buffer and backfill. As it was, the results of the thermo-hydraulic model were only representative for the first few hundred years. It can be speculated, though, how the flow field would have evolved later on, had proper boundary conditions been applied. Since the flow system would have had the potential to provide more water than buffer and backfill could take up, the general evolution would have been that of a slowing flow field converging towards complete standstill. If the density differences could have triggered a convection cell remains to be clarified because it requires gravity taking effect on density differences in the fluid to overcome viscous damping.

The thermo-hydraulic model could thus still be of interest in the future if several features would be changed. Obviously, a more realistic representation of a deposition tunnel in-

cluding the deposition boreholes could be achieved using more appropriate boundary conditions the buffer and backfill filled geotechnical openings. This would require re-saturation calculations to determine the water uptake rates as a function of time, though.

References

- /ALM 05/ Alm, P., Forsmark, T., Rhén, I.: Prototype Repository Installations for measurements of flow Repository into tunnels, water pressure in rock Repository and hydromechanical responses in Repository boreholes during operation phase. International Progress Report IPR-05-04, SKB, 2005.
- /CAR 59/ Carslaw, H.S. and Jaeger, J.C.: Conduction of Heat in Solids, Oxford 1959.
- /COM 13/ COMSOL: COMSOL Multiphysics Reference Manual version 4.4, COMSOL AB, 2013.
http://www2.humusoft.cz/ftp/comsol/guides/COMSOL_ReferenceManual.pdf
- /DER 03/ Dershowitz, W., Winberg, A., Hermanson, J., Byegård, J., Tullborg, E.-L., Andersson, P., Mazurek, M.: Äspö Task Force on modelling of groundwater flow and transport solutes; Task 6c - A semi-synthetic model of block scale conductive structures at the Äspö HRL. International Progress Report IPR-03-13, Swedish Nuclear Fuel and Waste Management Company (SKB), 2003.
- /FOR 01/ Forsmark, T., Rhén, I., Andersson, Ch.: Prototype Repository: Hydrogeology – Deposition- and lead-through boreholes: Inflow measurements, hydraulic responses and hydraulic tests. International Progress Report IPR-00-33, SKB, 2001.
- /FOR 05/ Forsmark, T. and Rhén, I.: Prototype Repository: Hydrogeology – Hydrogeology – diaper measurements in DA3551G01 and DA3545G01, flow measurements in section II and tunnel G, past grouting activities. International Progress Report IPR-05-03, SKB, 2005.
- /FRA 17/ Fransson, Å., Åkesson, M., Andersson, L.: Bentonite Rock Interaction Experiment Characterization of rock and installation, hydration and dismantling of bentonite parcels. Report R-14-11, Swedish Nuclear Fuel and Waste Management Company (SKB), Stockholm, 2017.

- /KRI 07/ Kristensson, O. and Hökmark, H.: Prototype Repository - Thermal 3D modelling of Äspö Prototype Repository. Report IPR-07-01, Svensk Kärnbränslehantering AB (SKB), Stockholm, 2007.
- /KRI 10/ Kristensson, O. and Johannesson, L.-E.: Description of the Prototype Repository Test compiled for EBS Task-Force. (includes accompanying data files) Clay Technology Ab, draft version, 2010.
- /KRÖ 04/ Kröhn, K.-P.: Modelling the re-saturation of bentonite in final repositories in crystalline rock. Abschlussbericht des BMWA-Vorhabens 02 E 9430, Bericht GRS-199, GRS Braunschweig, 2004.
- /KRÖ 10/ Kröhn, K.-P.: State Variables for Modelling Thermohaline Flow in Rocks. FKZ 02 E 10336 (BMW i), Gesellschaft für Anlagen- und Reaktorsicherheit (GRS) mbH, GRS-268, Köln, 2010.
- /KRÖ 11/ Kröhn, K.-P.: Code VIPER - Theory and Current Status. Status report, FKZ 02 E 10548 (BMW i), Gesellschaft für Anlagen- und Reaktorsicherheit (GRS) mbH, GRS-269, Köln, 2011.
- /KRÖ 17a/ Kröhn, K.-P.: Characterizing groundwater flow in the fractured rock at Äspö, Sweden. Computing and Visualization in Science, Springer, Volume 18, Issue 4–5, pp 185–192, 2017a. <https://doi.org/10.1007/s00791-017-0279-5>
- /KRÖ 17b/ Kröhn, K.-P.: Hydraulic Interaction of Engineered and Natural Barriers – Task 8b-8d,8f of SKB. Summary report, FKZ 02 E 10336, 02 E 10548, 02 E 10558, 02 E 11102, and 02 E 11213 (BMW i), Gesellschaft für Anlagen- und Reaktorsicherheit (GRS) mbH, GRS-430, Köln, 2017b.
- /KRÖ 18/ Kröhn, K.-P.: Re-saturation of compacted bentonite under repository-relevant flow conditions. FKZ 02 E 11102 (BMW i). Geomechanics for Energy and the Environment, Elsevier, 2018. DOI:10.1016/j.gete.2018.09.003

- /MAT 04/ Matthäi, S.K. and Belayneh, M.: Fluid flow partitioning between fractures and a permeable rock matrix. Geophysical Research Letters, vol. 31, L07602, doi: 10.1029/2003GL019027, 2004.
- /PAT 97/ Patel, S., Dahlstrom, L.-O., Stenberg, L.: Characterisation of the Rock Mass in the Prototype Repository at Äspö HRL Stage 1. Report HRL-97-24, Svensk Kärnbränslehantering AB (SKB), Stockholm, 1997.
- /RHÉ 01/ Rhén, I. and Forsmark, T.: Prototype Repository - Hydrogeology - Summary report of investigations before the operation phase. International Progress Report IPR-01-65, SKB, 2001.
- /SCN 12/ Schneider, A. (ed.): Enhancement of d^3f und r^3t (E-DuR). Final report, FKZ 02 E 10336 (BMW), Gesellschaft für Anlagen- und Reaktorsicherheit (GRS) mbH, GRS-292, 2012.
- /STI 01/ Stigsson, M., Outters, N., Hermansson, J.: Prototype Repository – Hydraulic DFN model no:2. International Progress Report IPR-01-39, Svensk Kärnbränslehantering AB (SKB), Stockholm, 2001.
- /STI 14/ personal communication.
- /SUN 05/ Sundberg, J., Back, P.-E., Hellström, G.: Scale dependence and estimation of rock thermal conductivity. Report R-05-82, Svensk Kärnbränslehantering AB (SKB), Stockholm, 2005.
- /SVE 12/ Svensson, U.: Task 8 Modelling a one m³ block of granite. Presentation at the 28th Meeting of the Task Force on Groundwater and Transport of Solutes, Berlin, 2012.
- /VID 17/ Vidstrand, P., Stigsson, M., Åkesson, M., Fransson, Å.: SKB Task Forces EBS and GWFTS - Modelling the interaction between engineered and natural barriers - A compilation of Task 8 descriptions. Report P-16-05, Svensk Kärnbränslehantering AB (SKB), Solna, 2017.

/VIL 07/ Vilks, P.: Forsmark site investigation – Rock matrix permeability measurements on core samples from borehole KFM01D. Report P-07-162, Svensk Kärnbränslehantering AB (SKB), Stockholm, 2007.

Table of figures

Fig. 3.1	Experiments at the Äspö URL.....	9
Fig. 3.2	Sketch of the tunnel system around the Prototype Repository	10
Fig. 3.3	Floor plan of the area around the Prototype Repository	10
Fig. 3.4	Ground plan showing the PR-tunnel and the G-tunnel	11
Fig. 3.5	Schematic view of the Prototype Repository	12
Fig. 3.6	Location and size of the secondary test boreholes	13
Fig. 3.7	Deterministic fractures according to /RHÉ 01/ and assumed fracture	14
Fig. 3.8	Outflow into the PR-tunnel related to location of the deposition boreholes.....	16
Fig. 3.9	Fracture traces and localised outflow locations in the deposition holes.....	19
Fig. 3.10	Outflow from diaper measurements	22
Fig. 3.11	Estimated outflow into different tunnel sections	23
Fig. 4.1	Matrix block including cut through the IJ-tunnel	27
Fig. 4.2	3d-subsets of the model (except matrix) including their names.....	28
Fig. 4.3	Relation of large fractures to the outer model surface.....	28
Fig. 4.4	3d-subsets of the model; close-up at the end of the PR tunnel	29
Fig. 4.5	3d-subsets of the model; close-up at deposition boreholes 5 and 6.....	29
Fig. 4.6	Visualization of 2d-subsets with boundary conditions	31
Fig. 4.7	Prescribed pressure distribution at the model boundaries.....	32
Fig. 4.8	2d-subsets of the model to which atmospheric pressure is assigned.....	33
Fig. 4.9	Visualization of fracture boundary edges with boundary conditions	34
Fig. 5.1	Domain of the thermal model.....	38
Fig. 5.2	Objects of different properties.....	40
Fig. 5.4	Heater power consumption simplified for modelling	42
Fig. 6.1	Temperature in a vertical cross-section through heater 1 after 3000 days ..	44
Fig. 6.2	Temperatures in boreholes 1, 3, and 6	45
Fig. 6.3	Boundary conditions for the thermo-hydraulic model	47
Fig. 7.1	Outflow measurements and model results	50
Fig. 7.2	PR-tunnel as well as intersecting large fractures	52
Fig. 7.3	Deposition borehole 1 as well as intersecting minor fracture 1.....	53
Fig. 7.4	Deposition boreholes 5 and 6 as well as intersecting fractures	53
Fig. 7.5	Horizontal cross-sections through the spatial pressure field.....	56

Fig. 7.6	Absolute velocity in a horizontal cross-section	57
Fig. 7.7	Velocity at the end of the PR-tunnel and at the northern discrete fracture...	58
Fig. 7.8	Flow across the northern deterministic fracture (square II in Fig. 7.14)	59
Fig. 7.9	Flow at the top of borehole 1 at different spatial resolutions.....	60
Fig. 7.10	Skin zones of the PR tunnel and borehole 1 sliced open.	61
Fig. 7.11	Flow field in a vertical semi-transparent slice of finite thickness.	61
Fig. 7.12	Temperature development at some of the sensors in borehole 5;.....	63
Fig. 7.13	Temperature development at some of the sensors in borehole 6;.....	64
Fig. 7.14	Idealised modes of heat flux over time.....	65
Fig. 7.15	Temperature distributions resulting from a fixed inflow into a) a beam, b) a semi-infinite plane and c) in a 3d-continuum	67
Fig. 7.16	Isoplane for an increase of 10 °C above initial temperature after 3500 days.....	68
Fig. 7.17	Isoplane for an increase of 10 °C above initial temperature after 5000 days.....	69
Fig. 7.18	Temperature distribution 650 days after switching on the heaters.....	69
Fig. 7.19	Temperature distribution after 1100 days across heater 3	70
Fig. 7.20	Temperature evolution on the surface of the deposition boreholes	70
Fig. 7.21	Isothermal, steady-state flow in a vertical cross-section.....	72
Fig. 7.22	Velocity field around the tunnels after 5 years of heating	73
Fig. 7.23	Temperature and flow field after 0, 500 days and 5 years of heating	74
Fig. 7.24	Temperature and flow field in section I after 0, 500 days and 5 years.....	75
Fig. 7.25	Temperature and flow field in section II after 0, 500 days and 5 years.....	76
Fig. 7.26	Outflow dynamics for the deposition holes.....	78
Fig. 7.27	Outflow dynamics for the large fractures.....	79
Fig. 7.28	Outflow dynamics for the northern and the southern fracture (close-up)	80
Fig. 7.29	Temperature distribution in the large fractures after 10 years model time ...	80
Fig. 7.30	Temperature in the southern deterministic fracture and fracture M1 after 10 years model time	81
Fig. 7.31	Outflow dynamics for the minor fractures.....	82
Fig. 7.32	Temperatures for the minor fractures after 10 years model time	83
Fig. 7.33	Outflow dynamics for sections of the PR-tunnel.....	84
Fig. 7.34	Outflow dynamics for the tunnels in the model.....	85
Fig. 8.1	Relation of test/model scale and measured/calibrated hydraulic conductivity	90

Fig. A.1	Humidity in the PR-tunnel from August 1999 to April 2000.....	105
Fig. A.2	Seasonal bandwidths of the humidity in the PR-tunnel	105
Fig. A.3	Humidity in the deposition holes from August 1999 to March 2000	108
Fig. A.4	Seasonal bandwidths of the humidity in the deposition holes.....	108
Fig. A.5	Humidity profiles in the deposition holes 3 and 6	109
Fig. B.1	Outflow into the PR-tunnel related to location of the deposition boreholes.....	112
Fig. B.2	Fracture traces at the Prototype Repository.....	113
Fig. B.3	Water-producing fracture in the section between 3593 m and 3600 m.....	114
Fig. B.4	Water-producing fractures in the section between 3587 m and 3593 m....	115
Fig. B.5	Water-producing fractures in the section between 3575 m and 3587 m....	116
Fig. B.6	Water-producing fractures at the outer seal	117
Fig. B.7	Fracture orientations, top view including TASS-tunnel	119
Fig. B.8	Assumed hydraulic features for the model.....	120
Fig. B.9	Identification of deterministic fractures.....	121
Fig. B.10	Borehole sections and deterministic fractures.....	122
Fig. B.11	Relation of fractures C and D and the northern major fracture	122
Fig. B.12	Relation of fracture zone I and the southern major fracture.....	123
Fig. B.13	Relation of minor fracture 1 a) to fracture B and b) to southern fracture....	123
Fig. B.14	Relation of minor fractures 2 to 6 to fracture B.....	124
Fig. B.15	Assumed fracture replacing fracture zone II.....	125

List of tables

Tab. 3.1	Approximate geometric data of the Prototype Repository	11
Tab. 3.2	Approximate geometric data of the deposition holes.....	12
Tab. 3.3	Outflow into the PR-tunnel measured by means of weirs.....	15
Tab. 3.4	Outflow into the PR-tunnel in terms of flux densities	17
Tab. 3.5	Total outflow into the deposition boreholes	18
Tab. 3.6	Localised outflow into the deposition boreholes	20
Tab. 3.7	Total, localised and areal outflow into the deposition boreholes.....	20
Tab. 3.8	Outflow (absolute and per metre tunnel) into the drift system	24
Tab. 3.9	Characterisation of the deterministic fractures	25
Tab. 4.1	Coordinates of the nodes of the boundary box.....	28
Tab. 4.2	Hydraulic data.....	30
Tab. 4.3	Subsets with pressure data from the rock	32
Tab. 4.4	Subsets with atmospheric pressure	33
Tab. 4.5	Outflow into the sections of the PR-tunnel	35
Tab. 4.6	Outflow into the deposition boreholes	36
Tab. 4.7	Outflow into other drifts.....	36
Tab. 5.1	Heat capacities at 25 °C	39
Tab. 5.2	Material data for the heat transport model	39
Tab. 7.1	Outflow rates for the steady-state isothermal flow model.....	54
Tab. 7.2	Comparison of particular outflow rates.....	55
Tab. 7.3	Outflow rates {kg/s} without contribution of the fractures.....	77
Tab. 7.4	Comparison of outflow rates of large deterministic fractures	79
Tab. 7.5	Comparison of outflow rates for minor deterministic fractures.....	81
Tab. 7.6	Outflow rate for segments of the PR-tunnel without flow from the fractures	84
Tab. 7.7	Comparison of outflow rates for whole tunnels.....	85
Tab. A.1	Relative humidity in the PR-tunnel	104
Tab. A.2	Relative humidity in the deposition holes	107
Tab. A.3	Relative humidity profiles in two deposition holes	109
Tab. C.1	Outflow density for the deposition holes in [kg/(m ² s)].....	127

Appendix A Humidity measurements

Different measurement campaigns brought forward humidity data for the Prototype Repository (PR) tunnel as well as for the depositions boreholes. They show a seasonal variation for the tunnel and allow an estimation of the referring bandwidth. By comparison almost no such variations can be observed in the deposition boreholes. In case of deposition boreholes 3 and 6 even a profile along the borehole depth can be provided.

A.1 PR-tunnel

Between October 1999 and April 2000 the humidity in the PR tunnel was measured at six different locations. Data from /FOR 01/ listed in Tab. A.1 was used to plot the humidity evolution at these six locations (see Fig. A.1) as well as the bandwidth of the seasonal variations (see Fig. A.2).

The two data points with a relative humidity of about 63 % were measured in January 2000 at an unusually high local temperature of about 20 °C. During this time tests with heated fans were performed in the deposition holes which probably explains the increased temperature and the concurrent comparatively low values. Ignoring these two points in Fig. A.1 leaves the impression of a seasonal low in the relative humidity during the winter time. This is a well-known phenomenon related to tunnel ventilation. The air blown from the outside into the URL carries less water due to the low vapour saturation pressure at the low temperature outside while more or less the same temperature prevails in the underground.

Fig. A.2 shows that the humidity usually varies within a bandwidth of 10 % except for the end of the tunnel. Changes up to 20 % appear to be possible here which might indicate a less efficient ventilation towards the end of the tunnel.

Note that more recent humidity measurements close to the PR-tunnel appear to show values exceeding 90 % significantly quite often.

Tab. A.1 Relative humidity in the PR-tunnel; from /FOR 01/

Date	Tunnel chainage (m)	Relative Humidity (%)	Temperature (° C)
1999-10-08	3555	90	15.9
1999-11-09	3555	88	15.8
-"-	3590	94	16.2
1999-12-02	3548	76.8	12.7
-"-	3589	73.3	15.4
1999-12-15	3555	84 +/- 1	13.5
-"-	3586	81 +/- 1	14.7
2000-01-11	3548	80.3	12.4
-"-	3586	80.5	14.8
2000-01-15	3548	70.2	14.4
-"-	3586	62.7	19.8
2000-01-17	3548	71.4	15.9
-"-	3586	63.2	21.4
2000-01-19	3548	71.4	12.4
-"-	3586	74.4	15.2
2000-01-21	3548	69	11.5
-"-	3586	75.9	14.1
2000-03-17	3548	76.1	-
-"-	3590	80.1	-
2000-04-19	3530	84.2	12.7
-"-	3560	91	13.4
-"-	3590	89.6	13

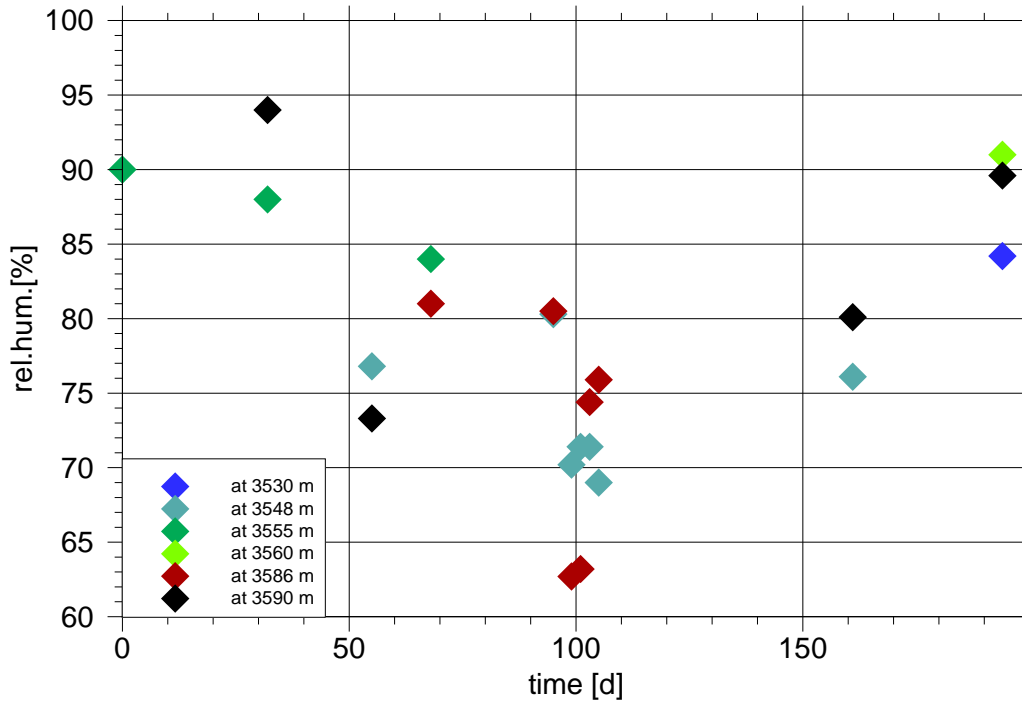


Fig. A.1 Humidity in the PR-tunnel from August 1999 to April 2000

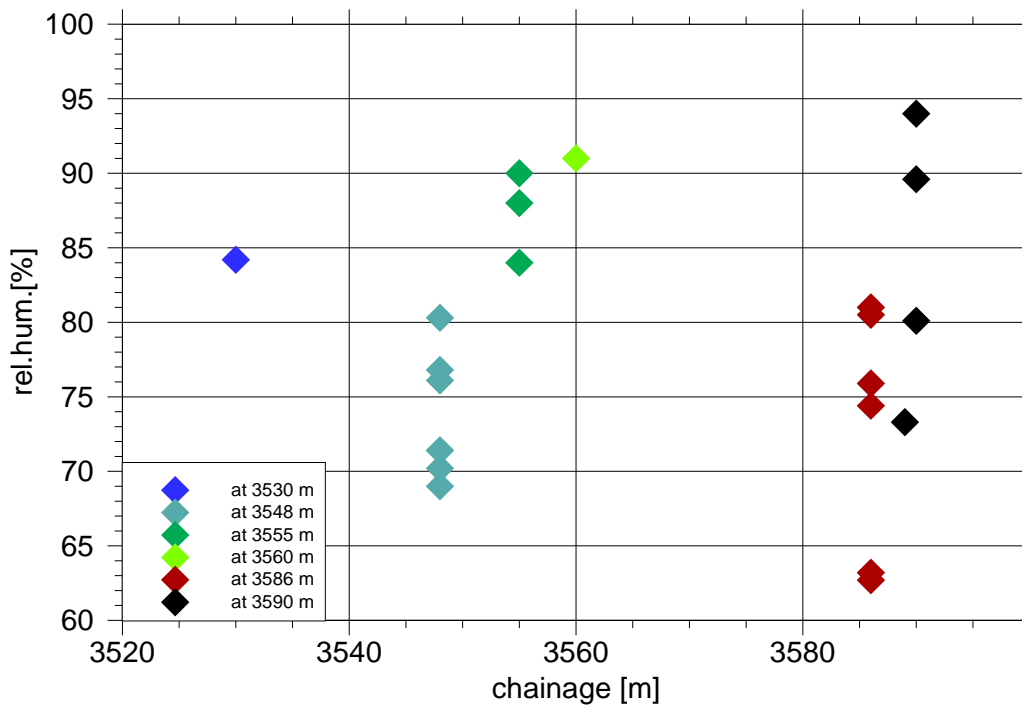


Fig. A.2 Seasonal bandwidths of the humidity in the PR-tunnel

A.2 Deposition boreholes

Relative humidity was also measured in the deposition boreholes between October 1999 and March 2000 at about two metres below the tunnel floor. On at least two occasions heaters and fans have been emplaced in the boreholes leading to irregularly low humidity values. While they are listed in Tab. A.2 they are omitted in Fig. A.3 and in Fig. A.4. There are nevertheless still four conspicuous data points below 80 % humidity that have been measured only one day after one of those heating campaigns. It can thus be speculated that these four data points were also compromised by the preceding heating. If so, the humidity in the boreholes of clearly above 85 % underwent no larger variations.

Because all these humidity measurements were performed at the same depth, they were supplemented by another measurement campaign in April 2000 where humidity profiles along the boreholes 3 and 6 borehole were also taken. The data are listed in Tab. A.3 and plotted in Fig. A.5. The profiles show rather little variations with depth except for the only data point below a depth of 8 m. In borehole 6 the humidity increases in the lowermost 2 m by 9 % possibly indicating free water at the bottom of the borehole. However, the level of 2 metres below the tunnel floor appears to be representative with respect to humidity for most of the boreholes thus increasing the confidence in the previously acquired data and the related conclusions.

Tab. A.2 Relative humidity in the deposition holes; from /FOR 01/

Date	Borehole	Relative Humidity (%)	Temperature (° C)	Comments
1999-10-08	DA3551G01	96.3	15.5	2 m below roadbed
1999-11-09	DA3551G01	94	15.7	2 m below roadbed
-"-	DA3575G01	57	24.3	Just below roadbed. Active fan in borehole.
1999-12-02	DA3545G01	88.2	13	2 m below roadbed
-"-	DA3551G01	87.7	13.4	2 m below roadbed
-"-	DA3575G01	88.8	13.8	2 m below roadbed
1999-12-15	DA3575G01	98.0	14.2	2 m below roadbed
-"-	DA3581G01	98.4	14.1	2 m below roadbed
1999-12-22	DA3545G01	96.8	13.8	2 m below roadbed
-"-	DA3581G01	96.2	14.5	2 m below roadbed
2000-01-11	DA3445G01	96.9	15	2 m below roadbed
-"-	DA3551G01	93.9	14.7	2 m below roadbed
2000-01-15	DA3551G01	43.2	23.5	2 m below roadbed. Active fan in borehole.
-"-	DA3581G01	93	14.9	2 m below roadbed. Active fan with no heat in hole.
2000-01-17	DA3545G01	31.4	28.5	2 m below roadbed. Active fan in borehole.
-"-	DA3581G01	47.3	27.2	2 m below roadbed. Active fan in borehole.
2000-01-19	DA3545G01	72.6	15	2 m below roadbed.
-"-	DA3581G01	73.7	15.6	2 m below roadbed.
2000-01-21	DA3545G01	74.8	13.5	2 m below roadbed.
-"-	DA3587G01	78	16	2 m below roadbed.
2000-03-17	DA3581G01	95.7	-	Borehole covered with plastic sheet to maintain RH

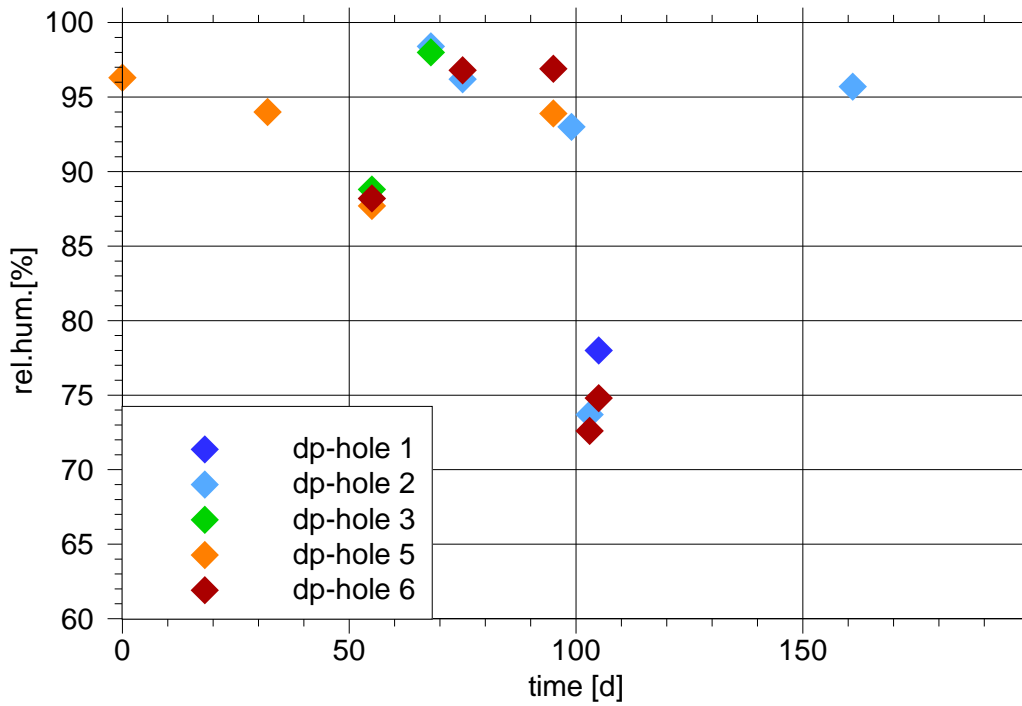


Fig. A.3 Humidity in the deposition holes from August 1999 to March 2000

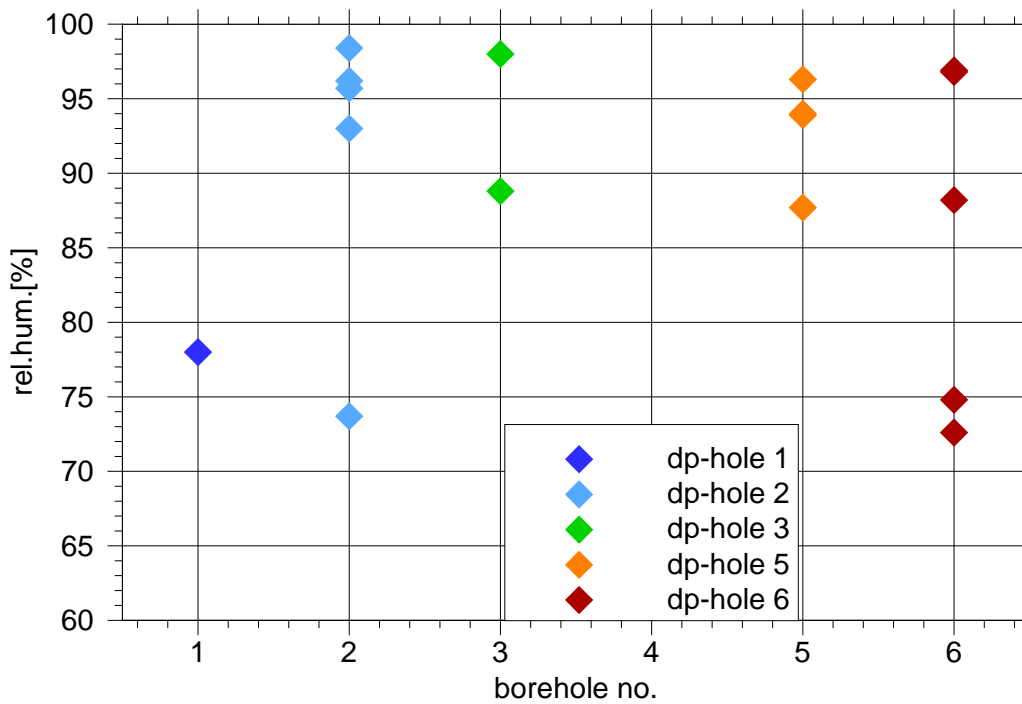


Fig. A.4 Seasonal bandwidths of the humidity in the deposition holes

Tab. A.3 Relative humidity profiles in two deposition holes; from /FOR 01/

Borehole	Level	RH (%)	Temp (° C)	Comments
DA3545G01	0.7	84.2	-	
“_“	2.7	83.8	-	
“_“	4.7	84.2	-	
“_“	6.7	85.7	-	
“_“	8.5	94.5	-	
DA3575G01	1.5	91.9	14.1	Close to borehole wall
“_“	4.0	94.3	13.6	Close to borehole wall
“_“	7.5	97.1	13.6	Close to borehole wall
“_“	1.5	96.8	13.6	At centre of borehole
“_“	4.0	95.8	13.5	At centre of borehole
“_“	7.5	94.0	13.5	At centre of borehole

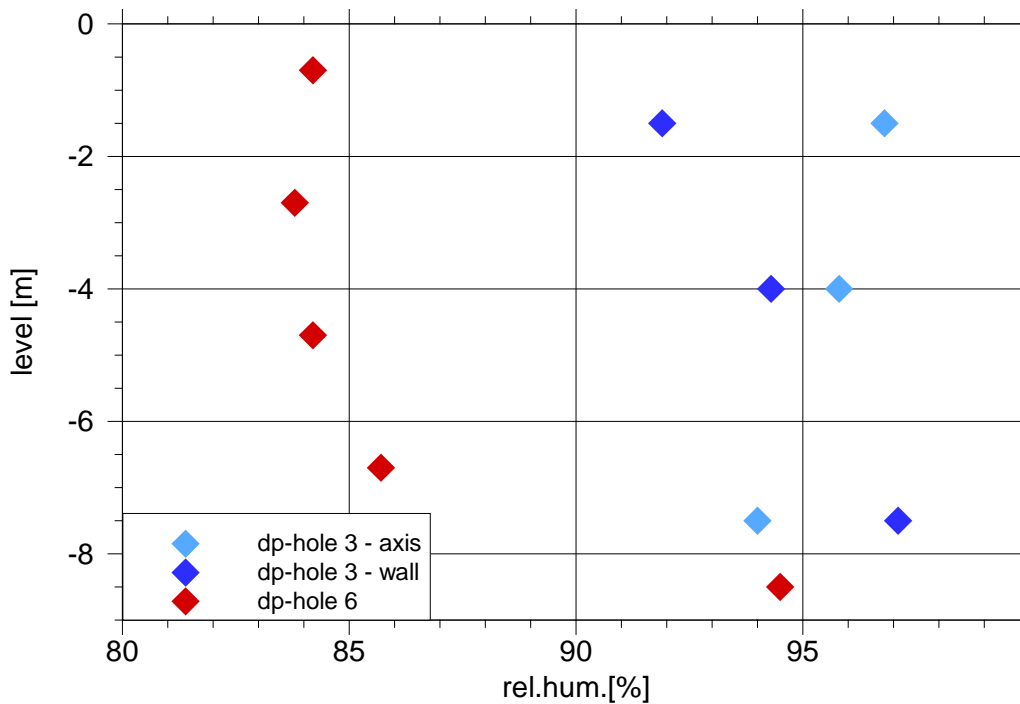


Fig. A.5 Humidity profiles in the deposition holes 3 and 6

Appendix B Deriving fracture locations from flow data and trace lines

This appendix is concerned with the task of defining a system of large deterministic fractures that is based on, and consistent with, the available evidence. In sections B.1 to B.6 conclusions are drawn exclusively from the outflow measurements in the PR-tunnel and the known fracture trace lines in the tunnel. Section B.7 was written later when the results of the extensive hydro-testing program /RHÉ 01/ were included in the considerations. A comparison between the fracture system assumed in section B.6 and the fracture system determined in the field (section B.7) showed an encouraging coincidence. The detected fracture system needed only one supplementary fracture to account for the high outflow rate at the end of the tunnel.

B.1 Deducing positions of highly water-producing features from outflow

Towards the end of the tunnel between 3593 m and 3600 m a highly conducting hydraulic feature (*feature 1*, see Fig. B.1) as indicated by the measurements in 1997 can safely be deduced. Less clear are the results of later measuring campaigns as just one weir had been installed at 3588 m instead of the two weirs at 3587 m and 3593 m in the first campaign. However, the later measurements confirm indirectly the results from the first campaign in that they provide roughly a mean of the two values from 1997.

Outflow rates in the section between 3587 m and 3593 m lay significantly below the rates of the neighbouring sections but also significantly higher than in the low water-producing zone between 3945 m and 3975 m. This could either indicate a separate hydraulic feature (*feature 4*, see Fig. B.1) or be the result of an overlapping of one or both hydraulic neighbouring features

Comparatively high outflow rates had been measured 1997 in the interval between 3575 m and 3587 m. In 1999 and 2000 the related weir positions had been shifted slightly to 3576 m and 3588 m but showed basically the same outflow rates. These results indicate either a strongly water producing fracture with a high dip and somewhat orientated along the tunnel axis, as to influence both weir sections or a local concentration of several more or less subvertical fractures that are spread over a distance of 5 to 10 m

(*feature 2*, see Fig. B.1). The fracture trace lines across the PR-tunnel depicted in Fig. B.2 suggest rather the second option.

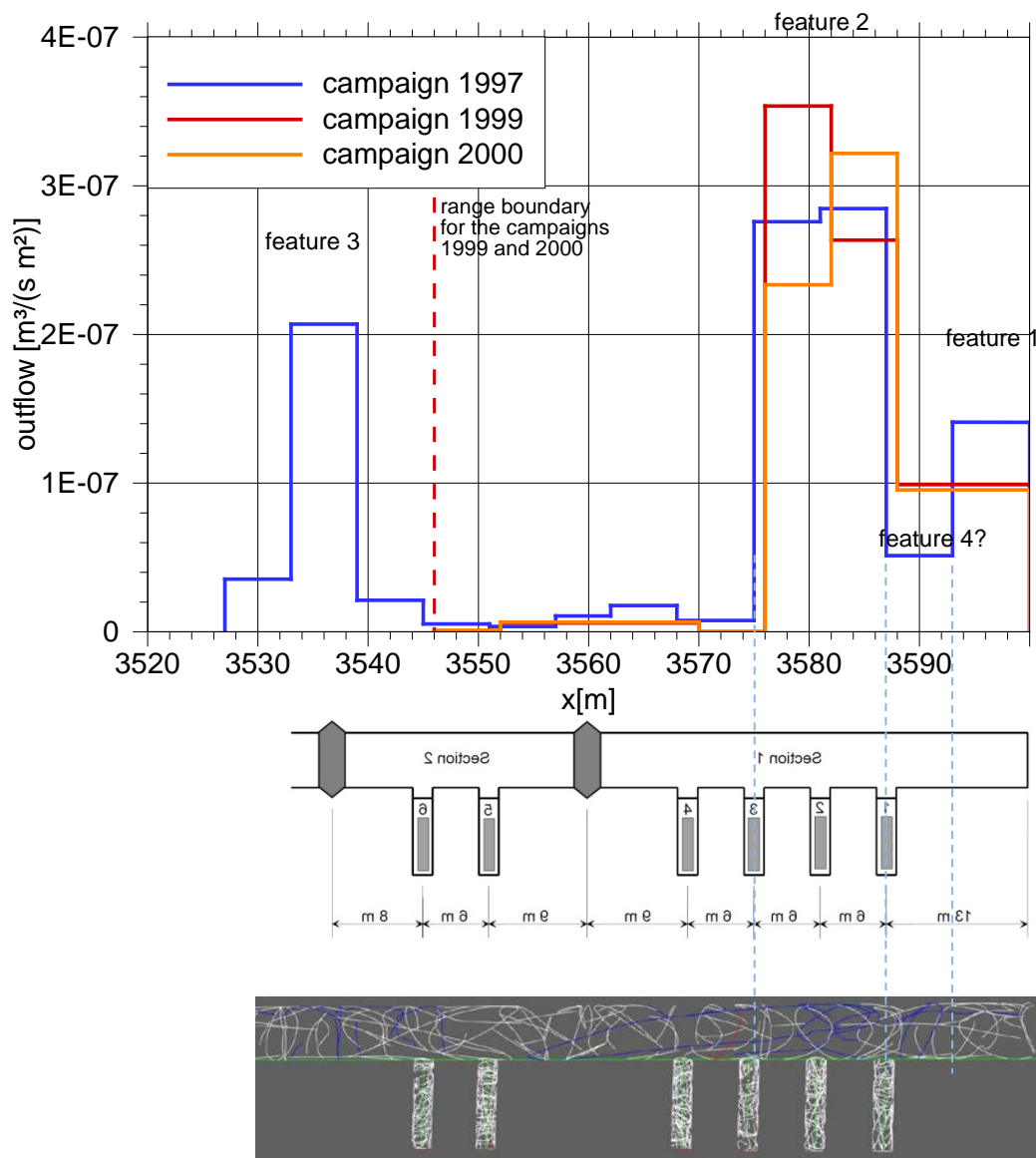


Fig. B.1 Outflow into the PR-tunnel related to location of the deposition boreholes; sketch of PR after /VID 17/, fracture traces after /KRI 10/

Yet another highly water-producing feature was found in the vicinity of the outer plug between 3527 m and 3545 m (*feature 3*, see Fig. B.1). It could only be detected in the first campaign as the later campaigns did not cover this area. Like the feature at 3580 m it is not restricted to just one weir but seems also to influence both neighbouring weirs.

B.2 Fracture trace lines

Fracture traces after /KRI 10/ are depicted in Fig. B.2 where water-bearing fractures are drawn in blue. Note that the blue traces indicate only locations, not productivity.

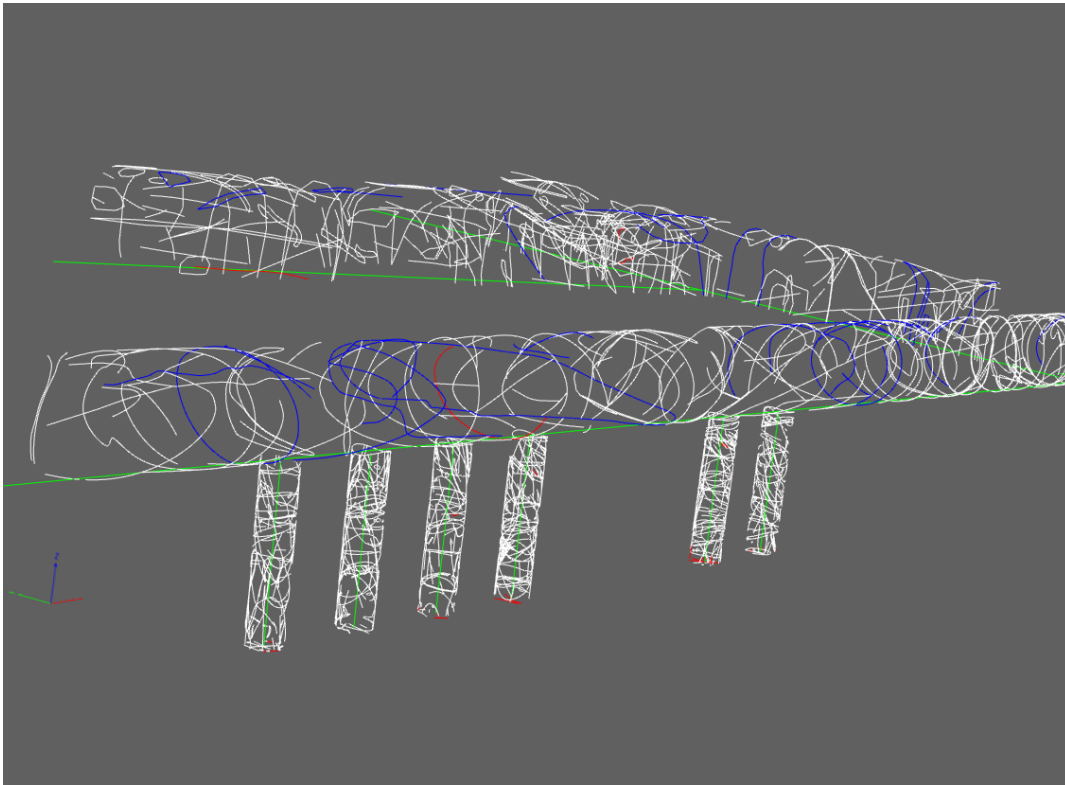


Fig. B.2 Fracture traces at the Prototype Repository; after /KRI 10/; water-bearing fractures are drawn in blue

The traces in the PR-tunnel are arranged in Fig. B.1 to relate to the measured outflow rates into the tunnel as a basis to find out about location and orientation of relevant water-producing fracture-like features in the vicinity of the PR-tunnel. In order to provide orientation also a sketch of the layout including seals and deposition holes is included.

B.3 Relation of the fracture trace lines and the outflow from the rock

Section from 3593 m to 3600 m

As discussed in section 3.4.1 the weir measurements indicate at least three separate features of high hydraulic conductivity. In the tunnel segment between 3593 m and 3600 m where feature 1 is presumed, just one water-bearing fracture trace at the tunnel ceiling had apparently been found, marked with dashed yellow line in Fig. B.3. This trace is orientated in the direction of the tunnel axis but has no counterpart at the floor or at the walls that would conclusively indicate an opened fracture. Size and orientation of the assumed feature 1 thus remain unclear.

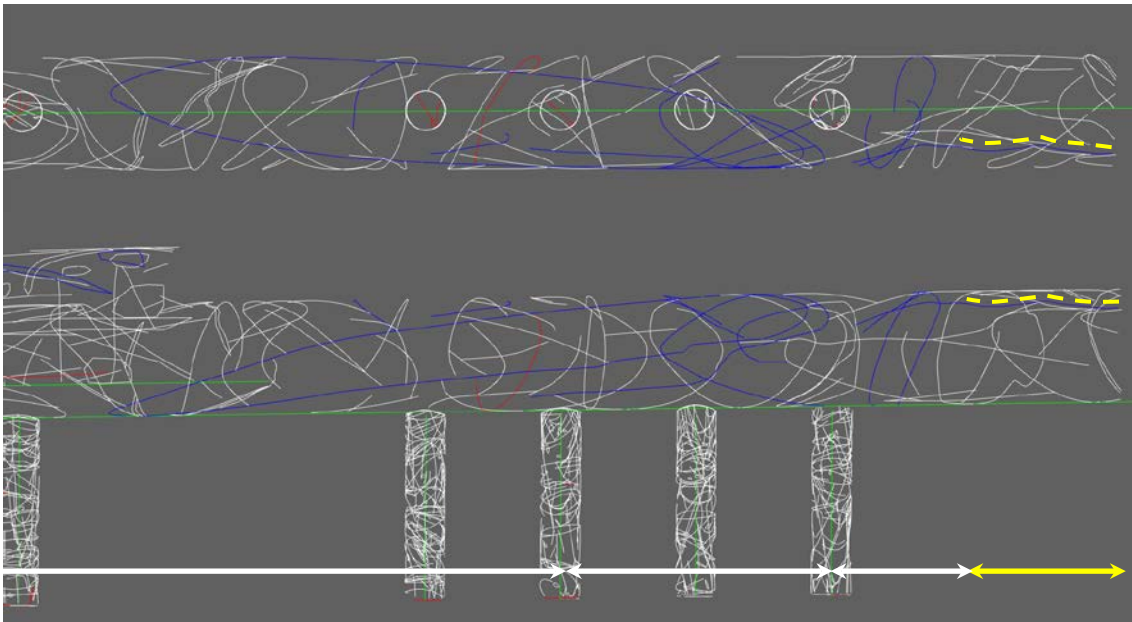


Fig. B.3 Water-producing fracture in the section between 3593 m and 3600 m marked with dashed yellow line; top and side view

Section from 3587 m to 3593 m

The tunnel section between 3587 m and 3593 m covering the possible feature 4 shows lower outflow rates than the neighboring sections, but is nevertheless quite productive in comparison to the rather dry zone between 3545 m and 3597 m. Here, three different traces of water-bearing fractures could be identified as depicted by coloured dashed lines in Fig. B.4. One is the continued fracture trace at the ceiling described in the previ-

ous section (yellow line), one is a similar but shorter trace (orange line) and one is a water-bearing fracture with a plunge of about 60° (light blue line).

Note that the latter steep fracture would cut through deposition hole DA3587G01 but not through DA3581G01, the neighboring one, if it was extrapolated in the direction that is indicated by the trace line. And indeed, two fracture traces in the borehole can be found that are consistent with such an extrapolation. This could be an explanation of the rather high outflow into DA3587G01 (see section 3.4.2). The fracture indicated by the blue line is therefore a promising candidate for the possible feature 4.

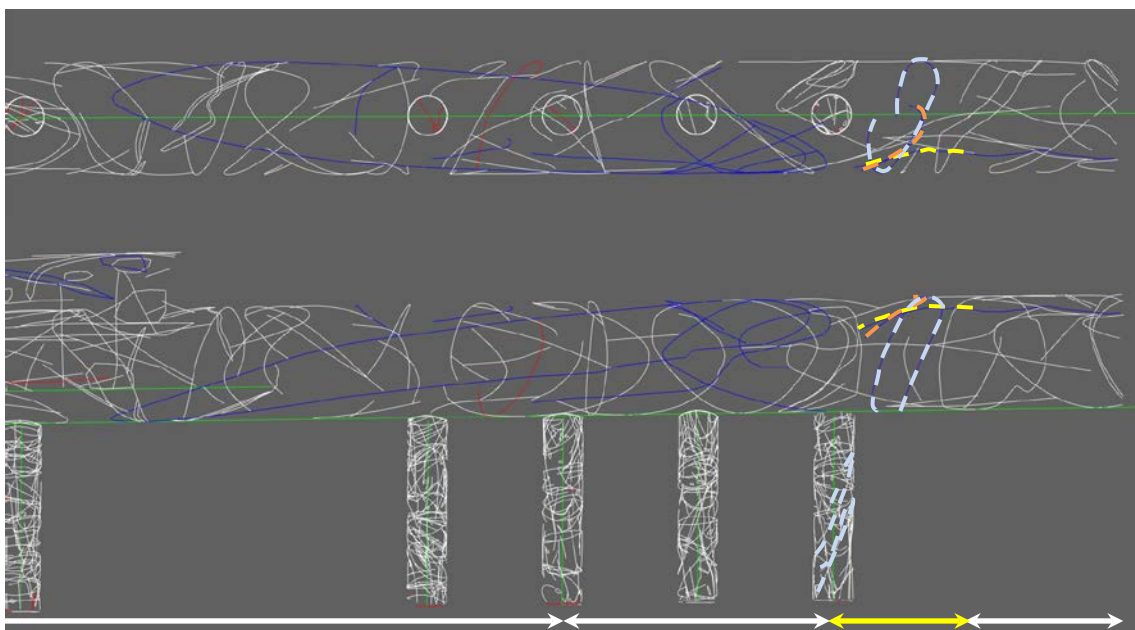


Fig. B.4 Water-producing fractures in the section between 3587 m and 3593 m marked with dashed lines; top and side view

Section from 3575 m to 3587 m

Feature 2 as assumed from the outflow measurements lies between holes DA3587G01 and DA3575G01 where indeed several traces of water-producing fractures had been found. However, none of them forms something even remotely resembling an oval shape that would indicate a cut through a fracture except a very large subhorizontal fracture indicated by the light blue dashed line in Fig. B.5. This fracture, however, lies only with one half in the strongly water-producing section. The other half is located in the neigh-

boring rather dry zone making it unreasonable to ascribe significant water outflow to this fracture. Again the trace lines of the water-bearing fractures provide no conclusive basis for the choice of size and orientation of a highly conductive feature 2.

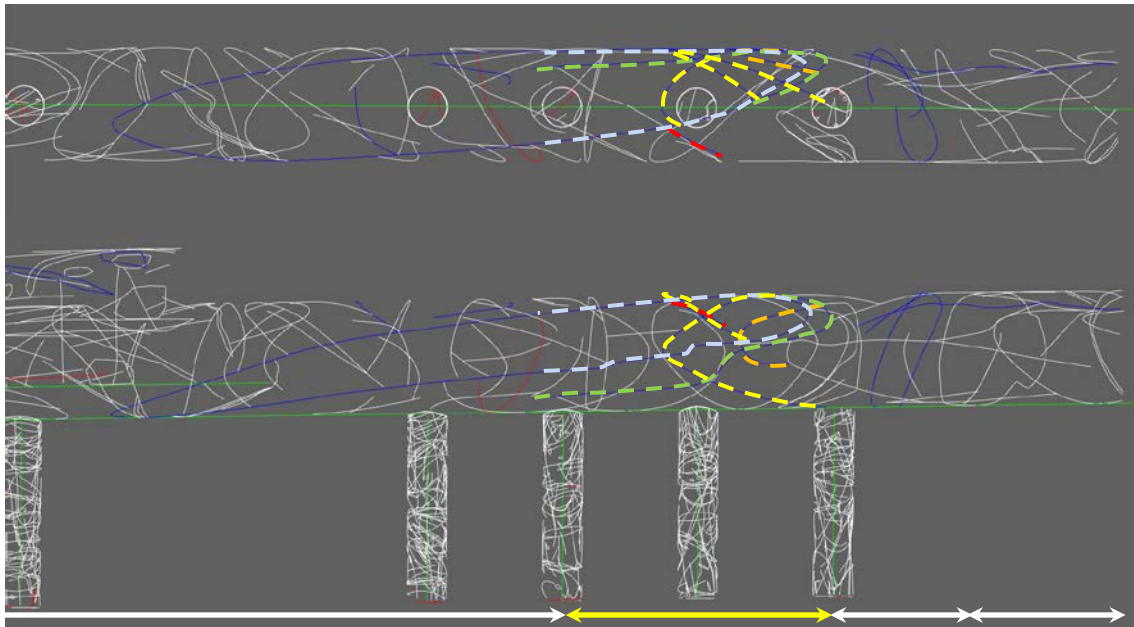


Fig. B.5 Water-producing fractures in the section between 3575 m and 3587 m marked with dashed lines; top and side view

Three equidistant sections from 3527 m to 3545 m

All three sections between 3527 m, 3533 m, 3539 m, and 3545 m show a rather high water outflow. Besides several trace lines of water-bearing fractures in these sections that do not connect across the tunnel wall there are indeed two more or less closed trace lines, marked in light blue in Fig. B.6, indicating a large fracture each. One appears to be located at 3537 m where the outer seal was later to be installed and the other is located at deposition hole DA3545G01. They have roughly the same orientation and might actually represent two large-scale fractures as they are approximately 8 m apart.

These two candidates for large-scale features cannot account, though, for the outflow in the section between 3527 m and 3533 m. But two suggestive trace lines marked with white dashed lines in Fig. B.6 can be found in this tunnel section. Even if they are not marked as water-producing they indicate nevertheless a third large-scale feature since

they show the same strike and dip as the other two. The previously assumed feature 3 might therefore actually be represented by three fractures.

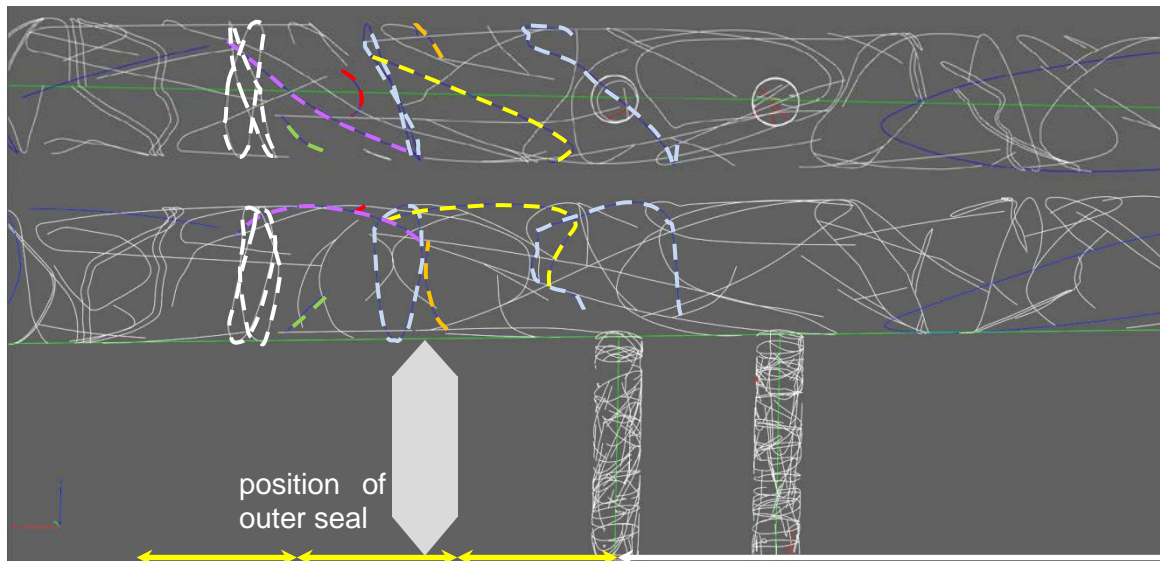


Fig. B.6 Water-producing fractures at the outer seal marked with dashed lines; top and side view

B.4 Value of the trace lines

On the whole the relation of the traces of water-bearing fracture and the water outflow rates measured by means of weirs appears to be rather loose. This has been shown here for the tunnel and in section 3.4.2 for the deposition holes. Only in case of features 3 and 4 there might be a relation between fracture traces and outflow rates. Reliable assumptions, however, concerning location and direction of water-conducting fractures on the bases of fracture trace lines only are not feasible.

Additionally, marking these fractures reveals that the majority does not connect to a complete loop around the tunnel surface which would indicate a fracture being large enough to be bored through by the PR-tunnel. Instead only fragments of such loops can be found which are located more often than not at the tunnel ceiling. This means that water-producing fractures in the vicinity of the PR-tunnel are either not very large in comparison to the tunnel cross-section or that they cannot be detected completely.

Note that there were alternative water-detection methods applied at the PR using paints that were more sensitive to water discharge than the actually applied conventional methods /STI 14/. In the same direction points recent evidence from the BRIE-experiment at Äspö. Columns of compacted bentonite installed in boreholes of 30 cm diameter showed after dismantling signs of wetting from fractures that had went unnoticed during the previously performed characterisation of the boreholes /FRA 17/.

B.5 Conclusions on fracture orientation

Earlier model concepts for the PR produced by the participants of the Task Force on EBS were based on the assumption that only large-scale features could explain the highly varying outflow rates that had been measured with the help of the weirs. This was underpinned by the fact that the section-wise mean outflow rates become very high if ascribed to localised flow from fractures as the mean rates vary already over two orders of magnitude (see Tab. 3.3). Assuming a similar geologic situation at the PR as at the BRIE-site leads again to the concept of fractures or deformation zones that continue downwards below the PR-tunnel although highly conducting features that occur at the ceiling but not at the bottom of the tunnel are hardly conceivable.

As the trace lines do not allow for an obvious choice of orientation of such large-scale features, at least a likely direction was sought here. For this purpose the whole ensemble of fracture traces in a ground floor plan of the tunnel system at the PR was investigated. In Fig. B.7 the apparent directions of all fracture traces are marked by short straight lines. They fall apparently into four groups, the groups being indicated by differently coloured lines. Each group represents roughly one fracture direction but the directions indicated by red and orange lines as well as by green and blue-green lines are quite similar. A reasonable choice of the large-scale fracture direction would be along one of these two general directions.

The slanted oval in Fig. B.7 indicates the position of a possible hydraulic feature that affects the PR- as well as the TASJ-tunnel. However, there is no such continuation of blue-green marked fracture traces from the PR-tunnel to the TASG-tunnel. This was taken as an indication that the assumed large-scale features are more orientated in the direction of the reddish marked fracture traces. All detected large outflow rates were therefore attributed to large-scale fractures that do not cross the TASG-tunnel.

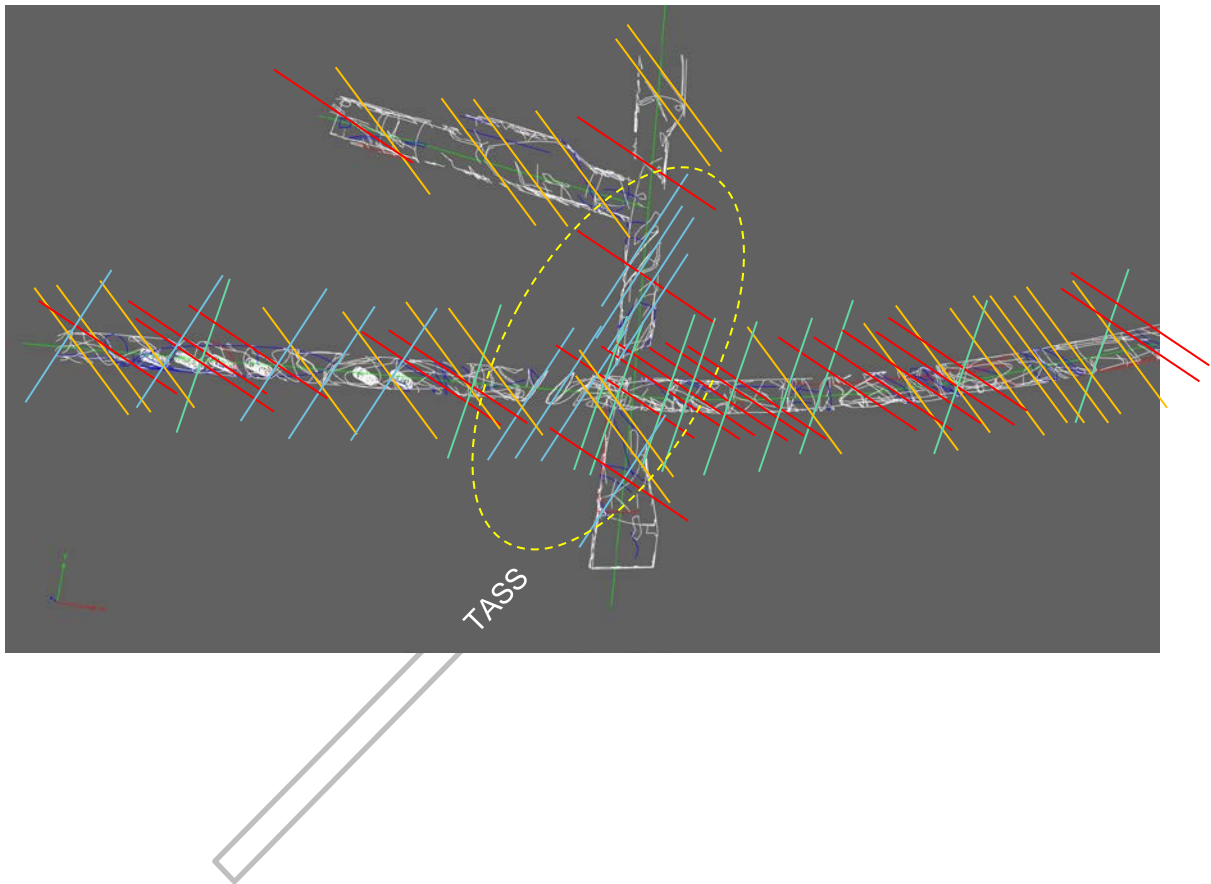


Fig. B.7 Fracture orientations, top view including TASS-tunnel; after /KRI 10/

B.6 Assumed hydraulic features for the model

Similar to Task 8 c&d for the BRIE-site, vertical fractures and fracture zones were defined for the model connecting the PR with the model boundaries. These features are depicted in Fig. B.8 and were justified as follows:

- There is a lack of significant water-bearing fracture traces in section 3593 m to 3600 m while outflow into the tunnel is comparatively high. A zone of increased permeability with a width of 4 m and a trend according to the orange lines in Fig. B.7 is thus positioned in such a way that the central plane crosses the tunnel axis at 3596 m (fracture zone I).
- The dashed light blue trace lines in Fig. B.4 are very suggestively indicating a single fracture with a plunge of about 60° that crosses the tunnel axis at 3590 m as well as deposition hole DA3587G01 (fracture A). While it would account for the comparatively high outflow rate in the deposition hole it would also contribute significantly to out-

flow into the tunnel between 3587 m and 3593 m. Since one hydraulic feature thus controls two outflow rates this fracture A might be difficult to calibrate.

- While outflow rates between holes DA3587G01 and DA3575G01 are quite high the related fracture trace lines are inconclusive. Therefore a vertical zone of increased permeability with a thickness of 2 metres orientated in the direction of the red lines is assumed (fracture zone II). There is no way, though, to avoid an increased outflow into one or more boreholes. Fracture zone II is thus positioned in such a way that it crosses the axis of hole DA3581G01 with its central plane. Difficulties with the calibration of the flow model are in this case more or less restricted to just one borehole.
- One vertical large-scale fracture is assumed to cross the axis of hole DA3545G01 in the direction of the orange lines (fracture B) to reflect the somewhat increased inflow into the tunnel section between 3539 m and 3545 m. Also the higher outflow rate in hole DA3545G01 in comparison to hole DA3551G01 was to be accounted for.
- Two more vertical large-scale fractures (fractures C and D) appear to be consistent with the suggestive fracture trace lines at 3539 m and 3531 m as well as with the rather high outflow rates in the tunnel in the sections between 3527 m, 3531 m, and 3539 m.

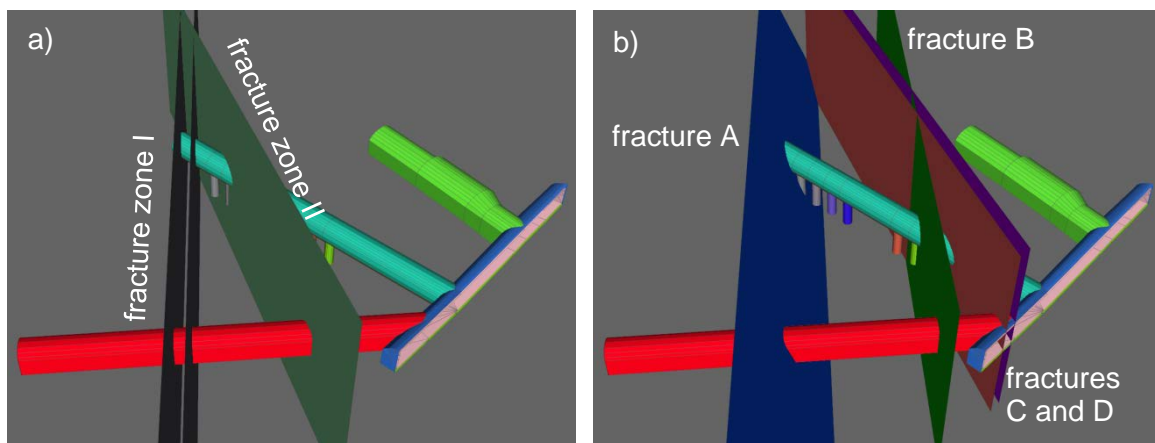


Fig. B.8 Assumed hydraulic features for the model: a) fracture zones and b) fractures

In all cases hydraulic interaction of fractures and fracture zones with the TASS-tunnel or the TASI-tunnel is possible but not considered to be relevant because of the direct connection with the boundary.

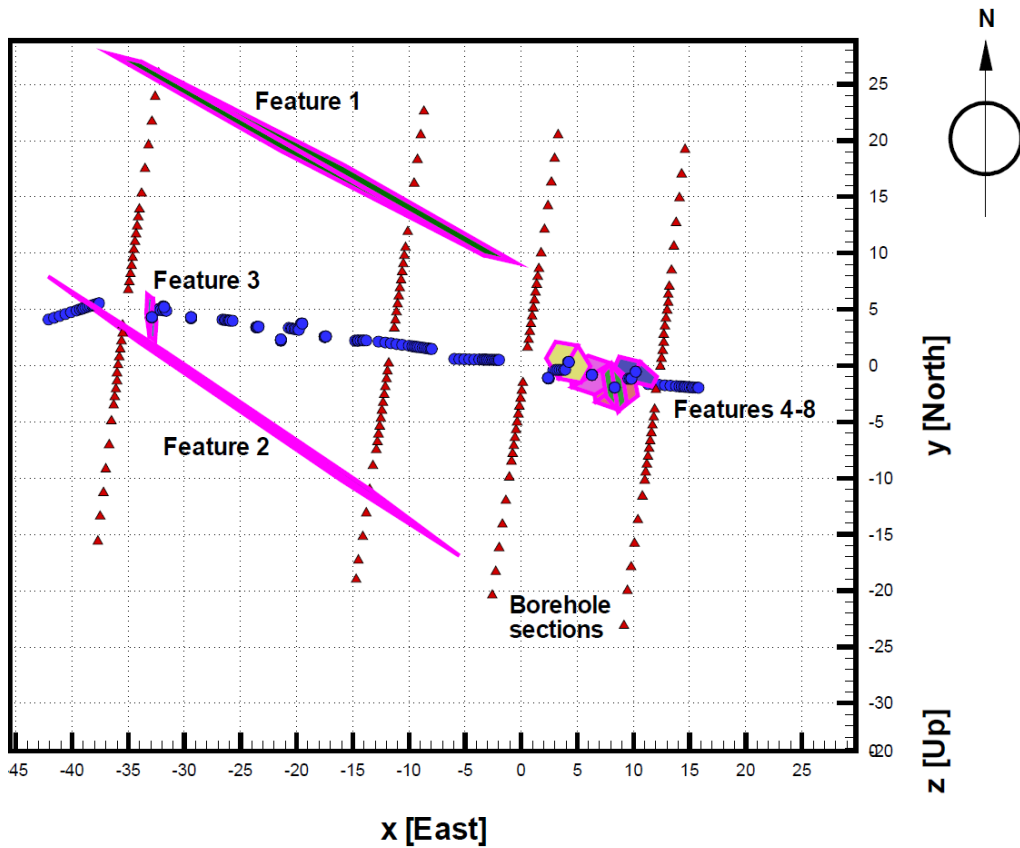


Fig. B.10 Borehole sections and deterministic fractures; from /STI 01/

The northern major fracture (feature 1 in Fig. B.10) and the assumed fractures C and D depicted in Fig. B.11 cross the PR-tunnel more or less at the same location if the former is prolonged as suggested in Fig. B.9. Also the fracture orientations are very similar. The northern major fracture can thus apparently replace the assumed fractures C and D.

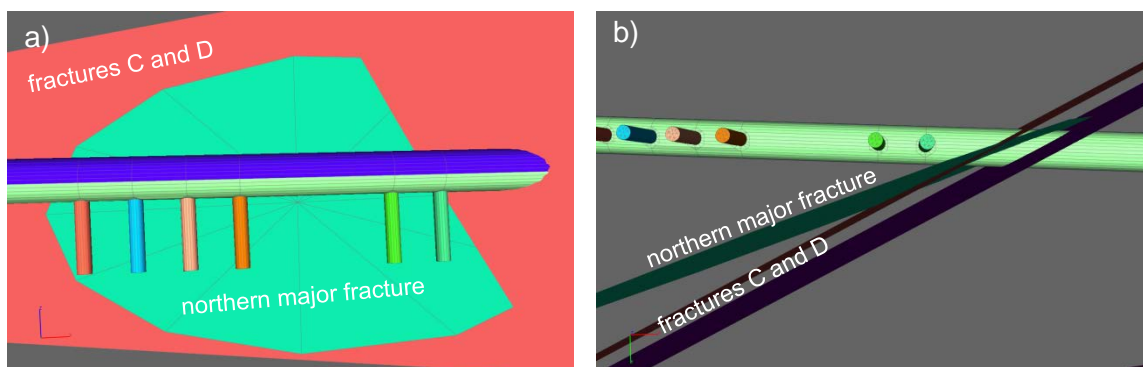


Fig. B.11 Relation of fractures C and D and the northern major fracture; views a) from the side and b) from the bottom

The southern major fracture (feature 2 in Fig. B.10) corresponds to the assumed fracture zone I as shown in Fig. B.12. Both cut also through the end of the PR-tunnel and both can be considered to be highly water producing. This would explain the high outflow rates at the end of the tunnel although the reason for the significantly reduced rate in the section between 3587 m and 3593 m becomes unclear.

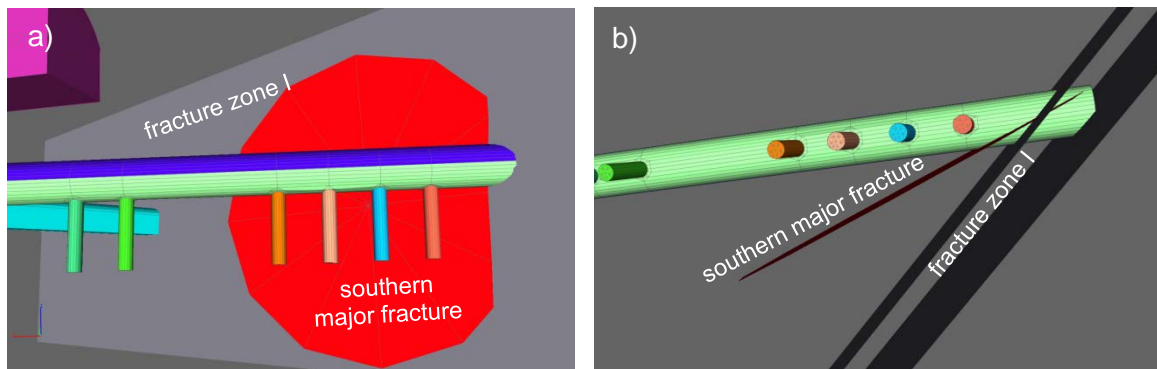


Fig. B.12 Relation of fracture zone I and the southern major fracture; views a) from the side and b) from the bottom

Minor fracture 1 (feature 3 in Fig. B.10) is rather small in comparison to the assumed fracture A but both cross deposition hole DA3587G01 more or less at the same location as shown in Fig. B.13 a). The measured rather high outflow at this deposition borehole is ensured in case of fracture A by the direct contact with the boundary and in case of minor fracture 1 through the connection with the southern major fracture (see Fig. B.13 b)).

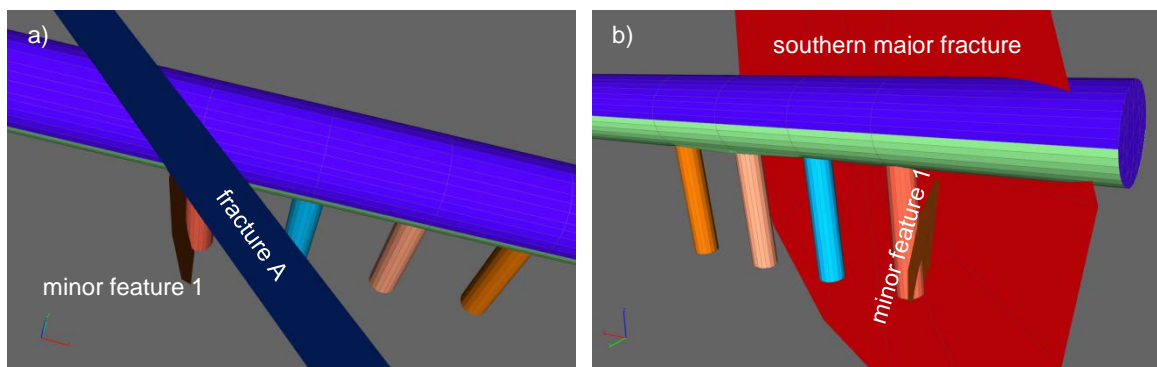


Fig. B.13 Relation of minor fracture 1 a) to fracture B and b) to southern major fracture

There is also a certain if not fully satisfying relation between the cluster of minor fractures 2 to 6 (features 4 to 8 in Fig. B.10) and the assumed fracture B. The cluster can

perfectly well explain an increased inflow into the deposition boreholes DA3545G01 as well as DA3551G01 and also the difference among these two boreholes. But it can of course not account for the slightly increased outflow into the tunnel in the section between 3545 m and 3551 m. However, this appears to be negligible as the outflow rate is actually rather low here anyway.

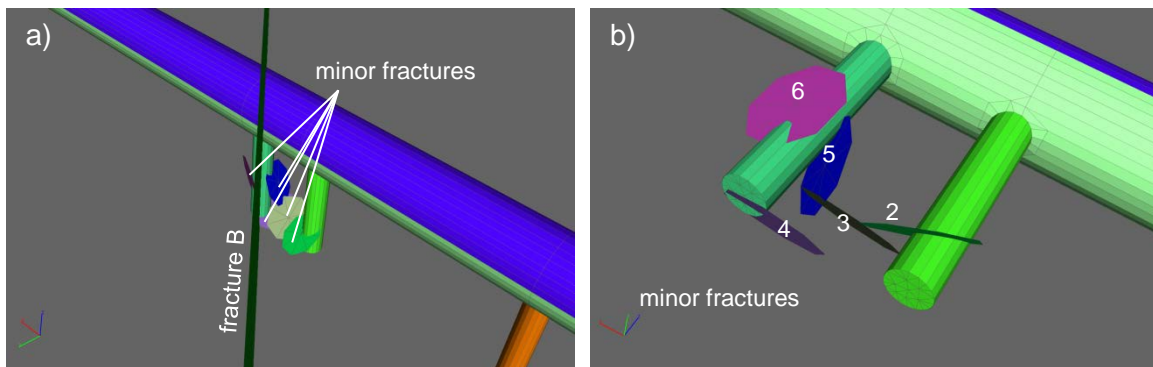


Fig. B.14 Relation of minor fractures 2 to 6 to fracture B

A certain problem poses fracture zone II accounting for the expected rather distributed but high outflow in the section between 3575 m and 3587 m. No fractures have been detected to account for this outflow. Considering also the fact that there is a dense field of test boreholes around the PR-tunnel there is only little room for a large fracture that could have gone unnoticed.

However, close inspection of location and size of the test boreholes depicted in Fig. 3.6 reveals a possible solution. A fracture connecting only to the end of the tunnel and extending beyond the end of the tunnel would be consistent with the results of the hydraulic test program. Such a hypothetical fracture is shown in Fig. B.15 a). It is chosen to fit in with the northern and southern major fractures in size and orientation (see Fig. B.15 b)) which leads to the same orientation as that of fracture zone II as depicted in Fig. B.15 c). The newly assumed fracture crosses the PR-tunnel in a similar way like the previously assumed fracture zone II. It avoids deposition hole DA3581G01, though, which is probably more in line with the outflow measurements from the deposition holes than the previously assumed fracture zone II.

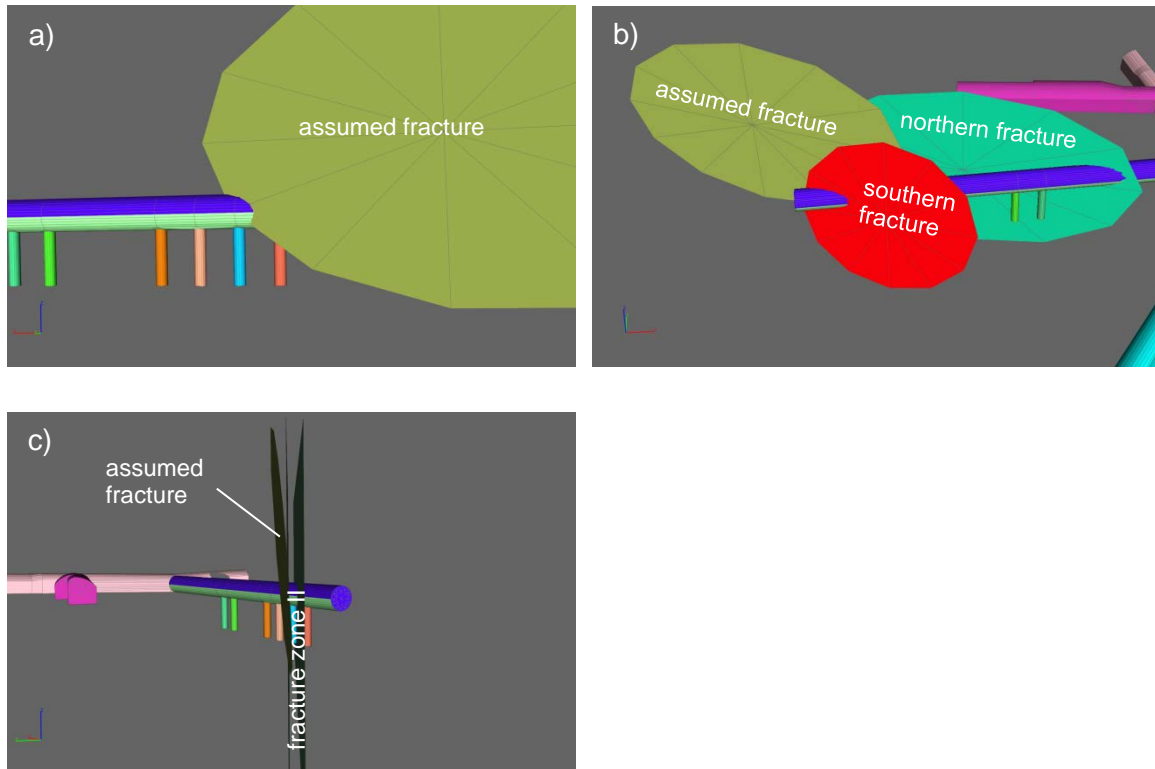


Fig. B.15 Assumed fracture replacing fracture zone II;
 a) location of the assumed fracture, b) relation to northern and southern major fracture, c) relation to fracture zone II

Appendix C Comparison of flow rates

As discussed extensively in /KRÖ 17b/ the relation of outflow rate from the rock and water uptake rate of the bentonite buffer defines the flow conditions at the buffer-rock interface. Exactly compared are the flow density of water leaving the rock (in mass or volume per square metre and second) that would be observed if water could freely exit the pore space of the rock and the flow density of water taken up by the buffer that would be observed if the bentonite had unlimited access to water (UA-conditions).

The surface area of one of the deposition holes amounts to 46.39 m² and the outflow rate for each borehole in kilogram per second is given in Tab. 7.3. These data are used to calculate the outflow density under isothermal conditions as compiled in Tab. C.1. The maximum flow density for air-dry bentonite compacted to a dry density of 1500 kg/m³ is estimated to amount to 1.02 l/(m² h) /KRÖ 18/ which is equivalent to 2.83·10⁻⁴ kg/(m² s).

Tab. C.1 Outflow density for the deposition holes in [kg/(m² s)]

dep.h 1	dep.h 2	dep.h 3	dep.h 4	dep.h 5	dep.h 6
2.52·10 ⁻⁶	2.57·10 ⁻⁶	2.35·10 ⁻⁶	2.22·10 ⁻⁶	1.61·10 ⁻⁶	1.37·10 ⁻⁶

A comparison shows clearly that the theoretical maximum uptake rate of the bentonite exceeds the calculated outflow from the rock. Initially, water coming from the rock is therefore immediately taken up by the bentonite. However, with the increasing water content at the buffer-rock interface, the uptake rate of the bentonite decreases until it falls below the outflow rate from the rock. During this period of time, the rock boundary for flow is quite well represented by free outflow conditions confirming the model assumptions at least for this period of time.

Further modelling of water uptake by the bentonite buffer would be necessary to calculate the time during which the assumption of free outflow can be considered valid. A lower boundary to that effect can be derived, though, by determining the period of time that passes until the uptake rate under UA-conditions has dropped to about 0.9 % of the initial value. Based on data from /KRÖ 04/ it can be estimated that free outflow conditions should prevail for considerably more than 135 days. After that time, a prescribed outflow rate according to the water uptake rate of the bentonite would have been appropriate. This would have led to a decreasing flow velocity in the rock, converging towards zero. At some point, convection cells due to density effects from heating might develop.

But they should not exert any influence on the wetting of the buffer because they would evolve despite outflow from the rock. Sufficient outflow for wetting the buffer and the onset of convection cells would thus coexist.

**Gesellschaft für Anlagen-
und Reaktorsicherheit
(GRS) gGmbH**

Schwertnergasse 1
50667 Köln

Telefon +49 221 2068-0

Telefax +49 221 2068-888

Boltzmannstraße 14

85748 Garching b. München

Telefon +49 89 32004-0

Telefax +49 89 32004-300

Kurfürstendamm 200

10719 Berlin

Telefon +49 30 88589-0

Telefax +49 30 88589-111

Theodor-Heuss-Straße 4

38122 Braunschweig

Telefon +49 531 8012-0

Telefax +49 531 8012-200

www.grs.de